

Cancer Detection and Imaging based on Innovative THz Techniques and Sensors

LIU, Kai

A Thesis Submitted in Partial Fulfilment

of the Requirements for the Degree of

Doctor of Philosophy

in

Electronic Engineering

The Chinese University of Hong Kong

January 2021

Declaration

I hereby declare this thesis is my original work and contains nothing which is the result of work done in collaboration with others, except as specified in the text and Acknowledgement. This work has not been submitted to this or any other university for the award of any degree.

The materials of some chapters have been published in the following journal and conference papers:

- Chapter 1

Q. Sun, Y. He, **K. Liu**, S. Fan, E. P.J. Parrott and E. Pickwell-MacPherson, “Recent advances in terahertz technology for biomedical applications”. Quantitative imaging in medicine and surgery, 7(3), 345 (2017)

- Chapter 4

K. Liu, R. Zhang, X. Chen and E. Pickwell-MacPherson, “Gold nanoparticle enhanced EGFR sensing based on Terahertz metamaterial biosensor”, *in submission to Biomedical Optics Express*.

K. Liu, R. Zhang, X. Chen and E. Pickwell-MacPherson, “Detection of EGFR Protein Using Terahertz Metamaterial Biosensor”. IRMMW-THz, Sept 2018.

- Chapter 5

R. Zhang, Q. Chen, **K. Liu**, Z. Chen, K. Li, X. Zhang and E. Pickwell-MacPherson, “Terahertz microfluidic metamaterial biosensor for sensitive detection of small-


volume liquid samples". IEEE Transactions on Terahertz Science and Technology, 9(2), 209-214 (2019)

- Chapter 6


Q. Sun, **K. Liu**, X. Chen, X. Liu, A. I. Hernandez-Serrano and E. Pickwell-MacPherson, "Utilizing multilayer structures to enhance terahertz characterization of thin films ranging from aqueous solutions to histology slides". Optics Letters, 44, 2149-2152 (2019)

K. Liu, Q. Sun, X. Chen, A. I. Hernandez-Serrano and E. Pickwell-MacPherson, "Highly Sensitive Terahertz Imaging Method For Paraffin Embedded Cancer Samples". 2019 44th International Conference on Infrared, Millimeter, and Terahertz Waves (IRMMW-THz), Sept 2019.

This thesis does not exceed 50,000 words.

Liu Kai  30th Dec 2020

Student Name Signature Date

Prof Emma MacPherson  30th Dec 2020

Supervisor Signature Date

Abstract

Terahertz (THz) techniques are being widely investigated in biomedical research and have shown great potential to improve clinical diagnosis of cancer. Although traditional cancer detection methods have achieved remarkable developments there are still challenges and limitations and the detection sensitivity of cancer related biomarkers needs to be further increased. The imaging contrast of cancer tissue is difficult to improve. Highly efficient terahertz biosensor and innovative imaging methods are promising candidates to overcome these difficulties, which then raise up the requirements on advanced terahertz biosensors and imaging strategies that can give better solutions.

Terahertz metamaterial biosensors are very sensitive to detect various biomolecules. We fabricate a bow-tie THz metamaterial biosensor and present the application on detecting EGFR proteins. The results demonstrate that the proposed device offers an efficient protein-probing strategy. Furthermore, we propose to use gold nanoparticles as a sensing enhancer for trace sample detection, and experimentally verify a significant increase in detection sensitivity. In addition, in order to realize liquid sample detection, we fabricated a multi-micro-channel metamaterial biosensor on the base of our previous design and demonstrated its capability for organic solution detection. This innovative sensor has better performance on liquid sensing compared with a single channel sensor, opening up the opportunity for trace cancer biomarker detection.

A key step in transforming terahertz imaging to a practical medical imaging modality lies in understanding the interactions between THz waves and biological tissues. Most of the models in the literature use the permittivity of liquid water to simulate the THz-tissue interactions, but they often neglect contributions from the biological background. Here, we present a method to prepare thin and flat dehydrated samples, which can be easily handled and measured in a transmission setup. Fundamental parameters for modelling THz-tissue interactions are also provided. Paraffin embedded oral cancer tissues are also imaged and characterised. To improve the image contrast, a new cancer tissue detection geometry, based on a water-tissue-quartz sandwich structure, was proposed and designed. THz images of cancer obtained from transmission and reflection systems are analyzed and optical parameters are calculated. The geometry significantly increases imaging contrast compared with traditional imaging methods and provides clear outline of the cancer detected. This work will further push terahertz techniques to clinical application.

摘要

太赫茲技術已廣泛用於生物醫學研究，並在診斷癌症方面具有臨床潛力。傳統的癌症樣本檢測方法雖然取得很多進展，但仍存在諸多挑戰和局限性，如癌症相關生物標記物的檢測靈敏度需要進一步提高，癌組織的成像對比度難以改善。太赫茲生物傳感器可以實現高效腫瘤樣品檢測的和新的太赫茲成像方法也具有提高腫瘤成像對比度的可能。我們將在本研究中提出新型太赫茲生物傳感器和腫瘤成像方法，探索太赫茲在腫瘤診斷中具有的潛在價值。

太赫茲超材料生物傳感器非常靈敏，能夠檢測各種生物分子。我們製造了領結式太赫茲超材料生物傳感器，並檢測到表皮生長因子受體蛋白。結果表明，提出的策略可以實現 EGFR 檢測。並且我們建議使用金納米顆粒作為痕量樣品檢測的傳感增強劑，在提高檢測靈敏度方面具有良好的性能。此外，為了實現液體樣品檢測，我們在先前設計的基礎上製造了一種多微溝道超材料生物傳感器，並將其應用於有機溶液檢測中。與單通道傳感器相比，這種創新的傳感器在液體傳感方面具有更好的性能，並為痕量癌症生物標誌物檢測提供了可能性。

太赫茲成像轉換為實際醫學成像模式的關鍵步驟在於理解太赫茲波與生物組織之間的相互作用。文獻中的大多數模型都使用液態水的介電常數來模擬太赫茲與組織的相互作用，但它們常常忽略了生物組織的貢獻。在這裡，我們提出了一種製備薄而平坦的脫水樣品的方法，該方法可以很容易地在傳動裝置中進行處理和測量，同時提供了用於分析太赫茲與組織相互作用的基本參數，並檢測石蠟包埋的口腔癌組織。我們基於前期口腔腫瘤太赫茲成像研究基礎，提出並設計了一種應用於太赫茲反射系統的新型癌組織檢測結構。我們分析了從透射和反射系統獲得的太赫茲圖像，併計算光學參數，與傳統方法

相比，這種水-組織-石英夾心結構薄層太赫茲成像技術大大提高了成像對比度，提供了清晰的癌症輪廓，這項工作將把太赫茲技術進一步推向臨床。

Acknowledgement

Time flies so fast and it is the time to say goodbye to my dearest friends and colleagues. I have enjoyed my PhD career with great help and support from many people. Now it's the great chance to send my sincere thanks to them.

I would like to deeply thank my supervisor Prof. Emma Pickwell-MacPherson, for trusting and selecting me to be her student and teaching me a lot about research. Even though I was struggling painfully sometime for a PhD degree, I have had a happy research experience in Prof. Emma's group. We worked happy, and we learn a lot from each no matter from life or work.

I would also like to sincerely thank Dr. Edward Parrott, Dr. Rui Zhang, Dr. Xuequan Chen and Dr. Rayko Stantchev. They have taught me a lot and given me many helps for my works. I also have to thank them for care and help during the IRMMW-THz conference aboard and instructions on projects.

Thanks Yuezhi He and Qiushuo Sun for helping me to get familiar with doing research when I first came. Thank Kaidi Li and Jiarui Wang for helping me to go through troubles and giving me so much support and joy in last 3 years. Dr. Hannah, Dr. Chunrui Han and Dr. Xavier, it is so good to have you worked together.

There are some important people who give me support from mainland. Professor Peiheng Wu, Professor Biaobing Jin, Professor, Caihong Zhang, thanks for helping me know what terahertz is and tell me its potential on medical application. Professor Qingang Hu, Professor Yongbin Mou, thanks for giving me endless care

and support on research and life. Thank my dear friends, Ruiqiao Wang, Lin Nan, Shubo Zhang, Hongru Chen, your encourage and company help me so much.

Thanks all my basketball teammates and friends. I spent much time with you and have a happy daily life on the court and off court with all of you. Thanks Qi Wu, Sining Wang, Yanhao Zhao, Zongshan Hu, Chuhui Hu, Zhiming He, Chaoyang Wang, Yuanjian Yang, Rongyu Li, Nan Li...I will remember all of you, you teach me a lot. I will take the courage and be positive to face the challenge in the future.

My last thanks belong to my family. My Sister Mei, Ziyu, thank you so much for caring my life and study. My aunt Tieping and my uncle Baohua, you are also my parents, thanks for raising me up and giving me endless support. I feel very regret that I cannot see you again, dear uncle Baohua, you always live in my heart. My fiancée Wenfei, thank you for always accompanying with me, supporting me, giving me so much care and love. My Mom, your love is soundless but powerful. Thank you for everything you have given to me and I hope I will be your pride and give you a happy life in the future. Thank everyone around me, you warm my heart and give me power to live myself.

Collaborative notes

The majority of this thesis is my own work, including experiment design, simulation and fabrication of the sensors, all the experiment operation and data analysis. However, I would like to acknowledge Dr. Yuezhi He for the dehydrated model design, Dr Yao Liu for provide experiment equipment and materials on

nanoparticle related experiment, Dr Wenfei Liu for the preparation of gold nanoparticles, Dr. Rui Zhang for the teaching and assistance of simulation and fabrication of metamaterial and MMCMM sensors, Dr. Swench Chen for algorithm coding and THz-TDS system maintenance and Dr. Qiushuo Sun for proposing the thin film tissue imaging strategy.

Contents

Declaration.....	i
Abstract.....	iii
摘要	v
Acknowledgement.....	vii
List of Abbreviations.....	1
List of Figures	3
List of Publications.....	9
1. Introduction to THz medical applications.....	12
1.1. Terahertz waves.....	12
1.2. THz applications for cancer detection.....	13
1.2.1. Cancer related molecules and cells.....	13
1.2.2. Cancer tissue	16
1.3. Other cancer detection techniques.....	18
1.3.1. Ultrasound	19
1.3.2. X-ray	21
1.3.3. Computed tomography	23
1.3.4. PET / CT	23
1.3.5. Endoscopy.....	25
1.3.6. Pathology	26

1.4. Thesis Overview	28
2. Terahertz system	30
2.1. THz generation and detection.....	30
2.1.1. THz generation.....	30
2.1.2. THz detection.....	32
2.2. THz time domain spectroscopy (THz-TDS) system.....	34
2.2.1. THz reflection system	35
2.2.2. THz transmission system	38
3. Data processing method.....	42
3.1. Data processing in the transmission system	42
3.2. Data processing in reflection system.....	45
3.2.1. Baseline subtraction	46
3.2.2. Impulse function	47
3.2.3. Calculation of the refractive index and absorption coefficient.....	49
3.3. Summary	51
4. Detection of EGFR with terahertz metamaterial biosensor	52
4.1. Introduction	52
4.2. Methods.....	53
4.2.1. Metamaterial simulation	53
4.2.2. Metamaterial fabrication.....	54

4.2.3. Sensing experiment procedure	57
4.3. Results.....	60
4.3.1. EGFR detection results with Ab functionalized sensor	61
4.3.2. Bare GNPs detection.....	61
4.3.3. Connection of GNP with EGFR antibody.....	62
4.3.4. EGFR detection results with GNP-Ab functionalized sensor	64
4.4. Summary	69
5. Multi-microfluidic-channel metamaterial biosensor	70
5.1. Introduction	70
5.2. Simulation.....	71
5.3. Results.....	75
5.4. Summary	83
6. Oral cancer characterization and imaging.....	84
6.1 Tissue preparation techniques and THz measurements	84
6.2 Improved sample preparation techniques.....	85
6.3 THz Measurements of Dehydrated Porcine samples.....	89
6.4 Ex vivo THz Detection of Oral Cancer Tissues	91
6.4.1. Thin film oral cancer imaging with terahertz.....	93
6.4.2. Imaging and spectroscopy of thick oral cancer samples	94
6.4.3. THz parameters of thick oral cancer tissues	96

6.4.4. Sandwich structure reflection geometry	96
6.5 Summary	100
7. Conclusions and key findings.....	101
Bibliography.....	104

List of Abbreviations

Ab	Antibody
AER-α	anti-estrogen receptor alpha
ATR	Attenuated Total Reflection
BCC	Basal cell carcinoma
BSA	Bovine serum albumin
CCD	Charge-coupled device
CT	Computerized tomography
DHPLC	Denaturing high-performance liquid chromatography
DLS	Dynamic light scattering
EGFR	Epidermal growth factor receptor
ELISA	Enzyme-linked immunosorbent assay
ERP-α	estrogen receptor peptide alpha
FD	Frequency-Domain
FFPE	Formalin-fixed, paraffin-embedded
FOM	Figure of merit
FWHM	Full width at half maximum
GNP	Gold nanoparticle
IDC	Infiltrating ductal carcinoma
IHC	Immunohistochemistry
IPA	isopropanol
MM	Metamaterial
MMCMCB	Multi-microfluidic-channel metamaterial biosensor
ODU	Optical Delay-Line Unit
PBS	Phosphate-buffered saline
PCA	Photoconductive Antenna
PCR	Polymerase chain rection

PDMS	Polydimethylsiloxane
PET	Positron emission tomography
PFA	Paraformaldehyde
QCL	Quantum Cascade Laser
X-ray	X-radiation
SNR	Signal-to-Noise Ratio
TD	Time-Domain
THz	Terahertz
THz-TDS	THz Time-Domain Spectrometer

List of Figures

1.1	The electromagnetic spectrum, the green area shows the terahertz range.	13
1.2	(a) The transmission spectrum of the bare metamaterial; (b) The schematic diagram of THz-TDS measurement of cells using the designed metamaterial biosensor in ref [29].	15
1.3	Ultrasound probe detects the object.	20
1.4	Schematic setup of X-ray.	12
1.5	Paraffin block of oral cancer tissue and hematoxylin-eosin (HE) staining slide.	27
2.1	A schematic of photoconductive switch functioned as a THz mitter.	32
2.2	A schematic of golay cells detector.	34
2.3	A schematic of a fiber-based THz-TDS reflection system that consists of a femtosecond pulsed laser, delay stage, photoconductive emitter and detector, focusing lenses and an imaging window.	36
2.4	Terahertz reflection imaging system.	37
2.5	THz time-domain signal of quartz window. The first pulse is from the bottom of the quartz window and second pulse is from the upper quartz-air interface.	38
2.6	THz frequency-domain signal. The Frequency domain signal is obtained in ambient air, and the pulse reaches the noise floor about 1.7 THz.	39

2.7	A schematic of THz-TDS transmission system. The red arrows show the propagation of the THz beam.	40
2.8	THz time domain signals of dry air (less than 5% relative humidity) and wet air (70% relative humidity).	41
2.9	THz frequency domain signals of dry air (less than 5% relative humidity) and wet air (70% relative humidity).	41
3.1	Schematic of wave propagation in transmission geometry.	44
3.2	Air and baseline measurement with reflection system.	48
3.3	Time domain measurement of air and baseline from reflection system.	48
3.4	(a)Time domain signal and (b)impulse function signal of human skin with THz reflection geometry.	50
4.1	Simulated transmission spectrum of the bare bow-tie array metamaterial.	54
4.2	(a) Structure of the bow-tie array metamaterial. (b) Transmission amplitude spectrum of the fabricated bow-tie array metamaterial.	54
4.3	Photolithography procedures including film deposition, photoresist application, exposure, development, etching and resist removal.	55
4.4	Photograph of fabricated metamaterial biosensor.	56
4.5	Schematic diagram of the metamaterial biosensor for EGFR detection.	57
4.6	(a) DSL results of bare GNPs with different diameters. (b) DSL results of EGFR antibody modified GNPs with different diameters.	59

- 4.7 The transmission amplitude spectra of EGFR detected with Ab functionalized sensor. (b) The resonance frequency shift of EGFR with bare sensor (blue line) and with Ab functionalized sensor (red line). 61
-
- 4.8 The transmission amplitude spectra of GNPs with diameter of 5nm, 15nm and 25nm. 62
-
- 4.9 The transmission amplitude spectra of GNP-Ab with the nanoparticle diameter of 5 nm, 15 nm and 25 nm at concentration of 10 pM.(b) The resonance frequency shift of GNP-Ab with different GNP diameters. 63
-
- 4.10 Schematic diagram of the metamaterial biosensor for EGFR detection with GNP enhancement. 64
-
- 4.11 (a) The transmission amplitude spectra of EGFR detected with 5 nm GNP-Ab functionalized sensor. (b) The transmission amplitude spectra of EGFR detected with 15 nm GNP-Ab functionalized sensor. (c) The transmission amplitude spectra of EGFR detected with 25 nm GNP-Ab functionalized sensor. (d) The resonance frequency shift results for EGFR detection based on the metamaterial functionalized with Ab (orange line), 5nm GNP-Ab (purple line), 15nm GNP-Ab (light blue line), 25nm GNP-Ab (dark blue line), respectively. 66

-
- 5.1 (a) Simulated electric field distribution of the bow-tie array MM at the resonance frequency. (b) Simulated transmission spectrum of the bare bow-tie array MM. 72
-
- 5.2 (a) Schematic diagram of the multi-channel sensor based on a bow-tie array MM. (b) Simulated sensitivity for different channel width based on a bow-tie array MM. 73
-
- 5.3 Fabrication procedures of the proposed device. (a) Bow-tie array MM. (b) Constructed microfluidic multi-channels on the bow-tie array MM. (c) Quartz substrate. (d) 5-um-thick SU-8 photoresist on the quartz plate. (e) Adhesion of the quartz plate with photoresist to the MM with microfluidic multi-channels. (f) Exposure to the ultraviolet light to make a strong seal. (g) Microscopic image of the fabricated device (15-um-width multi-channels in the sensitive area of bow-tie array MM). (h) Schematic diagram of the one big channel design based a bow-tie array MM with the same dimension. 74
-
- 5.4 (a) Transmission spectra of the MMCMMB (MM with multi-channel, black line), and with water injected into the multi-channels (red line). (b) Transmission spectra of bow-tie array MM with only one big channel on top of the whole MM area (MM without multi-channel, blue line), and with water in the channel (magenta line). 76
-
- 5.5 Experimental results for the IPA-water mixtures with different IPA concentrations based on the proposed MMCMMB (MM with multi-channel) and the bow-tie array MM with only one big channel on top of the whole MM area (MM without multi-channel). Transmission 79

spectra for the different IPA-water mixtures based on the MM with multichannel (a) and the MM without multichannel (b). (c) FWHM results of the IPA-water mixtures with different IPA concentrations. (d) Average resonance frequency shift results of the IPA-water mixtures with different IPA concentrations. (e) Average absorption dip amplitude results of the IPA-water mixtures with different IPA concentrations.

5.6	Experimental results for the BSA solutions with different BSA concentrations based on the proposed MMCMMB. (a) Transmission spectra for the different BSA solutions based on the MM with multichannel. (b) Average resonance frequency shift results of the BSA solutions with different BSA concentrations.	81
6.1	Flow chart of dehydration protocol for porcine skin, muscle and fat tissue.	86
6.2	Dehydrated porcine (a) muscle, (b) skin, (c) fat tissues and their THz E _{max} image, where E _{max} is the maximum amplitude of THz time-domain signal.	87
6.3	The average refractive index (a) and absorption coefficient (b) of dehydrated porcine skin.	89
6.4	The average refractive index (a) and absorption coefficient (b) of dehydrated porcine muscle.	90
6.5	The average refractive index (a) and absorption coefficient (b) of dehydrated fat.	91

6.6	Optical image (a) and THz E_{\max} image (b) of normal oral tissue; optical image (c) and THz E_{\max} image (d) of oral cancer tissue.	93
6.7	(a)Optical image, (b)THz E_{\max} image and FD-magnitude image at 1 THz(c), 1.5 THz(d) of 30 μm oral cancer samples.	94
6.8	The average refractive index and absorption coefficient of 600 μm oral cancer tissue.	96
6.9	Percentage change of the amplitude of M by the cancer tissue compared to the normal tissue, assuming sample thickness $d_{\text{sam}}=30\mu\text{m}$, $\theta_{\text{air}}=30^\circ$, both the window and the prism are made of quartz.	97
6.10	Photographs of the paraffin-embedded oral cancer tissue (a) during the THz measurement, and (b) after drying, (c) histology image, the cancer area is marked with black dashed curve and the normal areas are marked with green dashed curves. (d-e) THz transmission spectroscopy images at 0.5 THz and 1 THz. (f-g) THz sandwich reflection spectroscopy images at 0.5 THz and 1 THz. The upper limit of the colormap scales of the THz images were all normalized to 1.	99

List of Publications

Peer-Review Journals:

1. **K. Liu**, R. Zhang, X. Chen and E. Pickwell-MacPherson, “Gold nanoparticle enhanced EGFR sensing based on Terahertz metamaterial biosensor”, *in submission*
2. J. Wang, A. I. Hernandez-Serrano, **K. Liu** and E. Pickwell-MacPherson, “Evaluation of transdermal drug delivery using terahertz pulsed imaging”. *Biomedical Optics Express*, 11(8), 4484-4490 (2020)
3. Q. Sun, **K. Liu**, X. Chen, X. Liu, A. I. Hernandez-Serrano and E. Pickwell-MacPherson, “Utilizing multilayer structures to enhance terahertz characterization of thin films ranging from aqueous solutions to histology slides”. *Optics Letters*, 44, 2149-2152 (2019)
4. R. Zhang, Q. Chen, **K. Liu**, Z. Chen, K. Li, X. Zhang and E. Pickwell-MacPherson, “Terahertz microfluidic metamaterial biosensor for sensitive detection of small-volume liquid samples”. *IEEE Transactions on Terahertz Science and Technology*, 9(2), 209-214 (2019)
5. Y. He[†], **K. Liu[†]**, C. Au, Q. Sun, E. P.J. Parrott and E. Pickwell-MacPherson, “Determination of terahertz permittivity of dehydrated biological samples”. *Physics in Medicine & Biology*, 62(23), 8882 (2017)

6. R. Zhang, Y. He, **K. Liu**, L. Zhang, S. Zhang, E. Pickwell-MacPherson and C. Zhang, Composite multiscale entropy analysis of reflective terahertz signals for biological tissues. *Optics Express*, 25(20), 23669-23676 (2017)
7. Q. Sun, Y. He, **K. Liu**, S. Fan, E. P.J. Parrott and E. Pickwell-MacPherson, “Recent advances in terahertz technology for biomedical applications”. *Quantitative imaging in medicine and surgery*, 7(3), 345 (2017)

Conference Presentations and Proceedings:

1. **K. Liu**, Q. Sun, X. Chen, A. I. Hernandez-Serrano and E. Pickwell-MacPherson, “Highly Sensitive Terahertz Imaging Method For Paraffin Embedded Cancer Samples”. 2019 44th International Conference on Infrared, Millimeter, and Terahertz Waves (IRMMW-THz), Sept 2019.
2. Q. Sun, X. Chen, **K. Liu**, X. Liu, A. I. Hernandez-Serrano and E. Pickwell-MacPherson, “Characterization of Thin Film Liquids By Multilayer Structure In THz Time Domain Reflection Spectroscopy”. IRMMW-THz, Sept 2019.
3. X. Chen, Q. Sun, J. Wang, A. I. Hernandez-Serrano, **K. Liu**, K. Li and E. Pickwell-MacPherson, “THz Instrumentation and Analysis Techniques for Biomedical Research”. IRMMW-THz , Sept 2019.
4. **K. Liu**, R. Zhang, X. Chen and E. Pickwell-MacPherson, “Detection of EGFR Protein Using Terahertz Metamaterial Biosensor”. IRMMW-THz, Sept 2018.

5. R. Zhang, Q. Chen, **K. Liu**, Z. Chen, K. Li, X. Zhang and E. Pickwell-MacPherson,
“Terahertz microfluidic metamaterial biosensor for tiny volume liquid samples”.
IRMMW-THz, Sept 2018.

†: Equal contributions

1. Introduction to THz medical applications

1.1. Terahertz waves

Terahertz (THz) radiation is in the frequency range between microwave and infrared waves, as shown in Fig. 1.1. Research into THz radiation has been pursued in a wide range of fields including chemistry, biology, materials science and medicine[1]–[4]. Potential applications are found in broad areas, such as detecting explosive materials [5], [6], high speed wireless communication[7], THz spectroscopy and tissue/skin imaging[8]–[11]. THz radiation has many special features which make it suitable for medical applications. Firstly, it has a very low photon energy, therefore there are no harmful ionizing effects on biomolecules during the measurement[12]. Secondly, THz radiation is sensitive to water content, showing great potential for accurate imaging of tissues with a good contrast, which could be beneficial if applied to cancer diagnosis. Moreover, the energy of rotational and vibrational transitions of molecules lies in the THz region[13]. This characteristic makes it a promising tool for the exploration of molecular interactions. This thesis will mainly focus on cancer sample sensing, cancer tissue imaging and characterization. Some relevant techniques will also be introduced and compared.

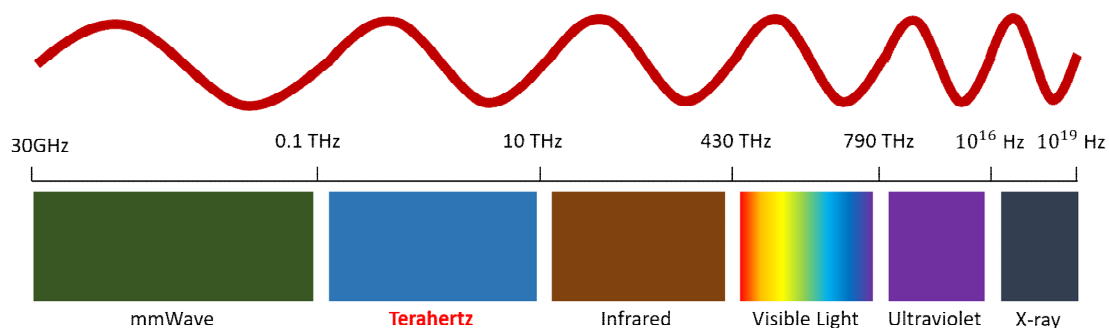


Fig. 1.1 The electromagnetic spectrum. The blue region shows the terahertz range.

1.2. THz applications for cancer detection

1.2.1. Cancer related molecules and cells

The term tumor associated molecule refers to antigen molecules that exist on tumor cells or normal cells, including embryonic protein, glycoprotein antigen and squamous cell antigen, which are commonly used in clinical tumor diagnosis[14], [15]. THz research on biomolecules and cancer related molecules dates back to the 1990s. At that time, researchers found that the vibrational modes of the conformational states of these biomolecules lie in the THz range. The use of THz radiation in cancer cell research has developed during the 21st century, using the high sensitivity of THz radiation to water to differentiate between normal and cancer cells using their different water contents[16].

THz techniques which are capable of detecting cancer related molecules and cells include label-free sensing, agent assisted sensing and sensor-based sensing. Label-free sensing is the most common method to detect biomolecules and cells. In 2000, Prof Markelz's group first used THz light to achieve the detection of the vibrational modes of biomolecules[16]. Following from that, a lot of research on biomolecules and cancer cells has since been reported[17]–[20]. Li et al. reported terahertz

detection results of anti-estrogen receptor alpha (AER- α) and AER- α and estrogen receptor peptide alpha (ERP- α) binding in aqueous solutions with a label-free sensing method[21]. It was found that as the concentration of AER- α increases, the absorption coefficient of AER- α also increases. Compared with classical methods like enzyme-linked immunosorbent assay (ELISA) and immunohistochemistry (IHC), their work proves that THz measurements can quickly and successfully obtain results, and can also yield a better reflection of the true physiological state of the antibody and antigen binding. Furthermore, THz measurements can avoid some of the disadvantages of these other techniques such as the influence of a fluorescent agent in the antibody and antigen reactions.

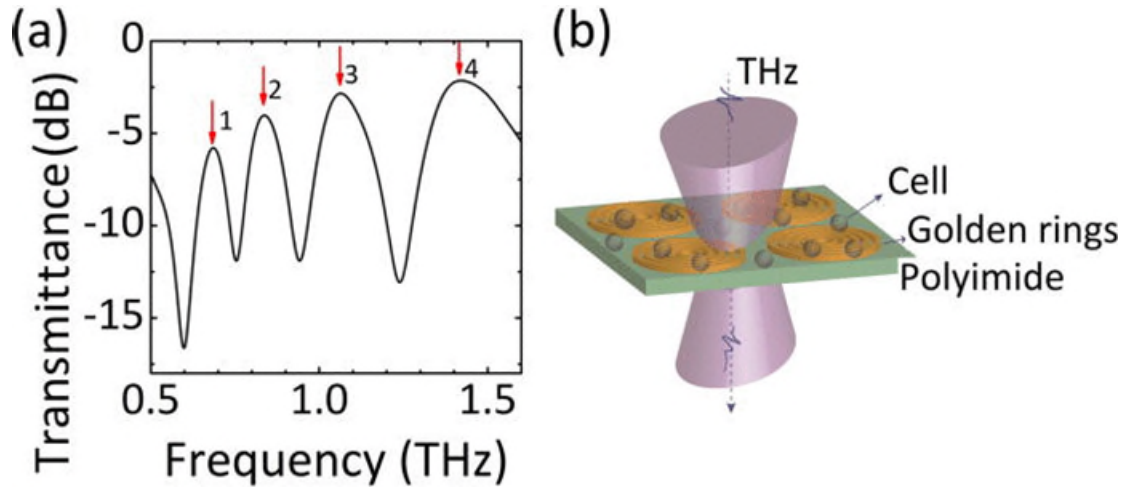
Metamaterials are a type of man-made periodic structure with special properties, such as negative refractive index and breakthrough imaging resolution beyond the diffraction limit[22], [23]. Electromagnetic waves can be manipulated using metamaterials in a way that cannot be achieved with traditional materials. Their peculiar properties are derived from their precise and unique geometry and size[22]. The microstructure is smaller than the wavelength of the light irradiating it. Metamaterials have many advantages as biosensors, for example they can detect trace volumes of samples with a high sensitivity, achieve label-free detection, yield fast response times, probe cancer cells and differentiate different types of cells[24]–[26].

In some cases, to detect low concentrations of cancer related proteins, an enhancing agent is introduced in the experiment, such as metal nanoparticles[27]. These nanoparticles connect to the biomolecules or DNAs, and the samples are detected with metamaterial biosensors. Arash et al. connected gold nanoparticles to

virus-envelope proteins and detected the composite sample[28]. This detection result showed that the gold nanoparticles increase the sensitivity of the metamaterial biosensor by introducing a large resonance shift.

Zhang et al. designed a metamaterial, which consists of a planar array of five concentric subwavelength gold ring resonators to examine the apoptosis of oral cancer cells (see Fig. 1.2)[29]. They found that relative change in the resonant frequency of the metamaterial can show the apoptosis level of oral cancer cells. The result measured using THz time-domain spectroscopy (TDS) has a linear relationship with the apoptosis result measured using Flow Cytometry. Zhang et al. reported a super-surface biosensor based on a non-mirror symmetrical design[30]. They designed a structure with a hexagonal radar chart and a two-dimensional time-frequency extinction card. This sensor can achieve label-free identification and sensing of the lung cancer cell A549 and the liver cancer cell HepG2 without immunological methods.

Fig. 1.2 (a) The transmission spectrum of the bare metamaterial; (b) The schematic diagram of



THz-TDS measurement of cells using the designed metamaterial biosensor in ref [29].

1.2.2. Cancer tissue

1.2.2.1. Skin cancer

THz imaging has great potential in skin cancer diagnosis. The first *ex vivo* THz measurements demonstrating the possible diagnostic ability were the measurements of basal cell carcinoma (BCC), which is the most common kind of skin cancer[31]. If treated too late this cancer can cause severe outcomes for human beings, therefore early detection is vital. THz imaging of BCC has been identified both *ex vivo* and *in vivo*[32]–[34]. Results have shown that a higher THz absorption coefficient can be measured in BCC tissue compared to healthy tissue, even when this difference cannot be seen by the naked eye or in histological images. This shows that THz imaging has the potential to offer better sensitivity than histological examination in BCC detection.

1.2.2.2. Breast cancer

The detection of the margins of tumors during surgery with THz imaging is a promising application. Early *ex vivo* research reported by Fitzgerald et al. has shown that THz radiation can distinguish breast cancer from the surrounding healthy tissue[35]. They found that the differences between cancerous and healthy regions arise from the different water contents and cell densities. Bowman et al. reported a series of work on the contrast between tissues by imaging breast cancer samples[36]–[39]. They prepared formalin fixed, histological samples of paraffin embedded infiltrating ductal carcinoma (IDC) and imaged them with a reflection geometry? THz system. They found that IDCs have a greater reflectivity compared to healthy soft tissues nearby. IDC regions normally have larger cell densities, this may be the reason for the high reflections in that region of the THz image. They also reconstructed 3D THz images and measured the thickness of breast cancer tissues, demonstrating the potential of THz imaging for breast cancer diagnosis and identifying tumor margins.

1.2.2.3. Colon cancer

Wahaia et al. performed THz measurements of colon cancer samples using transmission and reflection systems[40]. 2-mm-thick paraffin embedded colon carcinoma samples were studied. The mean absorption of the colon tumors was found to be 23% greater than the control but this is not enough to be statistically significant. Due to the large thickness of the non-homogenous sample, the precise calculation of THz parameters cannot be performed.

1.2.2.4. Oral cancer

Oral cancer is easily missed by both doctors and patients because of its typical ulcerous appearance, which causes many patients to miss their optimal treatment window. Clinically, the most common approach to diagnosis is histopathological examination, but this is a time-consuming process with dimensional limitations and needs to be observed from the perpendicular plane without the horizontal biological information. Thus, a better method which can obtain more diagnostic information should be developed for oral cancer detection, especially for those in the early stage. In recent years, the use of THz spectroscopy and imaging in the diagnosis of oral cancers was reported, with some developments having been achieved. In 2013 Sim et al. imaged seven fresh excised oral cancer tissues and an oral malignant melanoma tissue with THz radiation at 20 °C and -20 °C[41], [42]. THz imaging of both types of frozen tissue exhibited an increased contrast between the cancerous and healthy areas identified in the histological image, compared to the measurements taken at 20 °C. Additionally, a larger difference in the refractive index and absorption coefficient was found between oral cancer and normal mucosa at -20 °C than at 20 °C. A study of THz time domain waveforms and B-scan images was also performed, to demonstrated the detection of nodules below the tissue's surface, 2 such nodules were found, one in a squamous cell carcinoma tissue at frozen temperatures and another in the melanoma sample at both temperatures. The advantage of frozen samples was attributed to the removal of the effects of liquid water in the blood, but a dehydrated control is needed to confirm this hypothesis.

1.3. Other cancer detection techniques

Clinical cancer diagnostic techniques include medical imaging methods, such as ultrasound, X-ray computerized tomography (CT), experimental examination and histological examination. Each of these techniques has its own characteristics and limitations. CT provides morphological information of tissues, but with relatively low resolution and specificity[13]. Histological examination is the gold standard for cancer diagnosis, which can provide accurate information about cancer tissues but requires invasive and time-consuming procedures to prepare the tissue slices. For different people and diseases, different detection techniques are applied to help patients obtain an accurate diagnosis.

1.3.1. Ultrasound

Ultrasound is a sound wave with a frequency above 20,000 Hertz (Hz) and exceeds the human hearing range, and its propagation speed in human soft tissues and liquids is about 1500 m/s[43]. The following properties of ultrasound make it useful for tumor or cancer diagnosis[44]. Using ultrasound to diagnose cancer involves using the good orientation of the ultrasound beam during the propagation, projecting it towards the tumor or the suspicious part of the cancer and performing continuous scans to find the lesion, as shown in Fig. 1.3. When the ultrasonic beam is projected vertically onto the interface of two different tissues during the process of passing through the human body, part of the ultrasonic energy is reflected back, and the rest of the energy passes through the interface into the next tissue. According to this reflection feature, a lot of cancer data, such as the front and back diameters, internal interface and distribution regularity of tumors, can be measured[45]. In a homogeneous tissue with a consistent acoustic resistance, the ultrasound beam does not produce reflections. In an uneven tissue, when the

acoustic resistance of the tissues on both sides of the interface is different, reflection occurs. The greater the difference in acoustic resistance between the two sides, the stronger the reflection. Different tissues or tumors have different reflection patterns and intensities, which is helpful for both diagnosis and differential diagnosis. Depending on the difference in acoustic resistance between the two tissues, it is also possible that some of the beam can be refracted. Refraction and the reflection caused by an interface that is not perpendicular to the ultrasound beam may produce artifacts and cause misdiagnosis. When the ultrasonic beam passes through the tissue, its energy is absorbed by the tissue and the beam is gradually attenuated. Scattering and refraction are also causes of attenuation. In the same tissue, higher frequencies and shorter wavelengths lead to larger attenuation[44]. Under the same conditions, normal tissues have the least attenuation, general lesions have larger attenuation and cancerous tissues display the most attenuation. Therefore, the use of ultrasound can identify certain pathological properties of the sample.

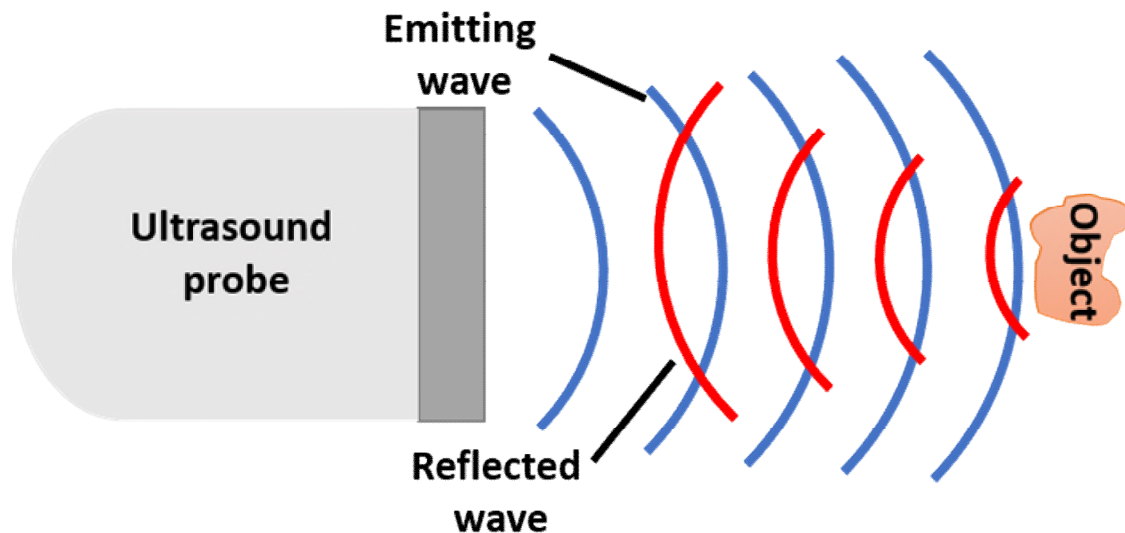


Fig.1.3 Ultrasound probe detects the object.

1.3.2. X-ray

X-radiation (X-ray) is an electromagnetic wave with extremely short wavelength and high energy. The wavelength of X-ray is shorter than that of visible light, and its photon energy is tens of thousands to hundreds of thousands of times greater than that of visible light[46]. X-rays are widely used in medical diagnosis[47]–[49], mainly based on X-ray penetration, differential absorption and sensitization. X-ray imaging systems consist of an X-ray tube, fluorescent screen and charge-coupled device CCD (Fig. 1.4). When X-rays pass through the human body, they are absorbed to different degrees and attenuate[50], [51]. For instance, the amount of X-rays absorbed by bones is more than that absorbed by muscles, therefore the amount of X-rays received by the detector is different after the radiation has passed through these different sample types, causing there to be a big difference in the intensity of the fluorescent effect or the photosensitive effect on the fluorescent screen or the photographic film. Therefore, shadows of different densities will be displayed on the fluorescent screen or the photographic film after development and fixing. According to the contrast of shadows, combined with clinical manifestations, laboratory results and pathological diagnosis, one can determine whether a certain part of the human body is healthy. As a result, X-ray diagnostic technology became the first non-traumatic visceral inspection technology in the world.

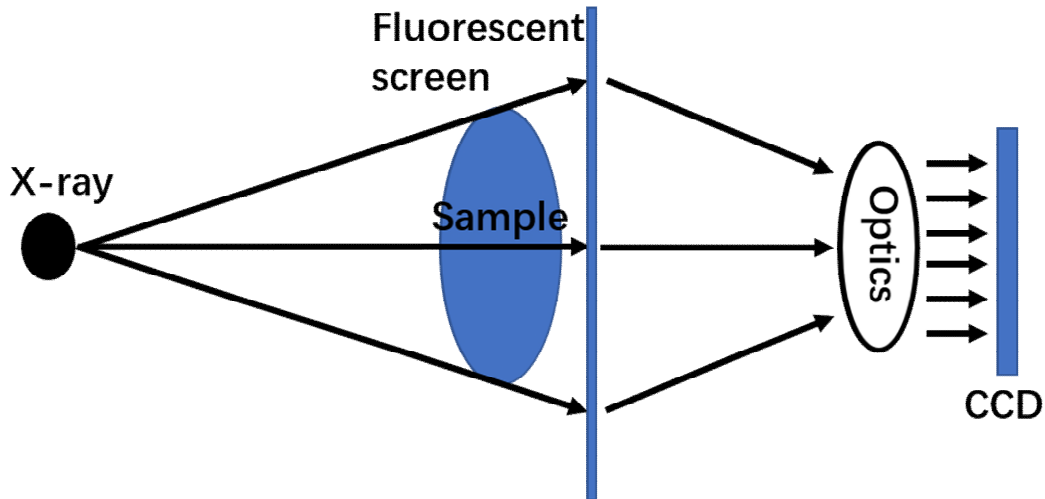


Fig. 1.4 Schematic setup of X-ray imaging.

One of the primary applications of X-ray imaging is in breast tumor detection[52]. For many patients, X-rays can detect the presence or absence of most breast lesions and determine the size. It can also identify some tiny tumors that are not easy to be found by clinical examination. However, in breast tissue with less fat, the breast tissue is generally more dense such that some tumor nodules are often concealed. X-ray examination is also very important for the diagnosis of bone tumors. The examination method is to take regular and lateral radiographs, if necessary, tomography, magnification photography or angiography. X-ray results will show the following features if the diagnosis is bone cancer. The bone at the lesion is damaged and the boundary with the normal bone tissue is blurred and the edge is irregular. However, in certain parts of the human body, especially the abdomen, because the density of several internal organs and the similarity of tissues, it is necessary to introduce harmless contrast agents. For the elements such as barium and iodine, the atomic coefficient is large, causing the photoelectric effect to occur with X-rays,

radiating characteristic X-rays that can pass through the human tissue to the film to form a gray mist, and artificially improve the display contrast to achieve the ideal inspection effect[53].

1.3.3. Computed tomography

Computed tomography (CT) produces a three-dimensional radiographic medical image reconstructed using digital geometric processing. It is a popular clinical examination technique, which is usually used for identifying cancer or some other hard tissue diseases. The working process of CT is to take a series of radiographic images of the body from different angles. Due to the different absorption capacity or reflectivity of X-rays in different tissues, the tomographic image can be reconstructed with computerized three-dimensional technology. In addition, three-dimensional images can be formed by stacking layers of tomographic images[54].

CT is very valuable for the diagnosis of head and neck diseases, such as maxillary cysts, bone tumors and oral cancer [55]. With the application of high-resolution CT, CT examination has increasingly shown its superiority in the diagnosis of chest diseases. Contrast-enhanced scanning is usually applied to determine whether the mediastinum is enlarged or obstruction diseases of lung, and is of great help in the diagnosis of primary and metastatic mediastinal tumors, lymph node tuberculosis, central lung cancer[56]. CT is more advantageous for the parts of the body that are more difficult to observe with plain film examination, such as the appearance of concentric and large vessel overlapping lesions.

1.3.4. PET / CT

PET is the abbreviation of Positron emission tomography. PET / CT is the fusion of PET and CT. While CT is able to provide high resolution imaging, PET is better able to provide information about the functionality, thus combining them gives a more complete picture.. PET uses radionuclides to mark the different abilities of tumor-related diseased tissues to uptake drugs to enable diagnosis. Because the radionuclides reach the intracellular maxtrix of the affected tissues to enable the image formation, PET is classified as biological imaging as well. At present, the conventionally used radionuclide is positron 18F-labeled deoxyglucose[57]. 18F-labeled deoxyglucose will be taken up by brain, kidney and cancer cells and cannot be metabolized within the cells. As a result, the distribution of 18F-labeled deoxyglucose will well reflect the distribution of glucose uptake and phosphorylation by cells in the body. In general, the higher the degree of tumor activity, the more radionuclide molecules are taken in by the tumor.

PET / CT is a safe and efficient tool that has many merits for cancer diagnosis compared to other radiology methods. PET / CT can diagnose cancer and other diseases early. Due to the active metabolism of tumor cells, the ability to take up radionuclides is around 10 times than that of normal cells, which will form an obvious bright dot on the cancer image[58]. Therefore, some hidden microscopic lesions can be found early. Most of the nuclides used in the examination are the basic elements that constitute human life and the half-life is short. The dose received by the human body is slightly higher than

the dose of a chest CT scan[57]. The inspection result is more accurate. Through qualitative and quantitative analysis, it can provide valuable functional and metabolic information. In addition, it can provide accurate anatomical information, which helps determine and find the precise location of the lesion, and the examination results of combined PET/CT have higher accuracy than PET or CT alone. Examinations can be performed quickly. Other imaging techniques scan only selected parts of the body, while a PET-CT full-body scan takes only 20 minutes, and can obtain results of PET, CT, and fusion of them[58]. Through the cross-sectional, sagittal and coronal images of the whole body it is possible to intuitively see the diseased parts and conditions of the whole body.

1.3.5. Endoscopy

An endoscope is an optical instrument that is sent into human body through the natural orifice to check for disease[59]. It can directly observe the lesions of the internal cavity of organs, determine their location and scope, and take pictures or biopsies. This technique greatly improves the accuracy of cancer diagnosis and can be used for certain treatments. Endoscopy is widely used in examination of internal organ cancers, such as gastroscopy for gastric cancer, bronchoscopy for lung cancer and cystoscopy for bladder cancer[59]–[61]. The bronchoscope and digestive endoscope are the two main clinical endoscope instruments for cancer diagnosis. The development of various bronchoscopes means that it plays an increasingly

important role in the early diagnosis of lung cancer. Compared with conventional white-light bronchoscopy, autofluorescence bronchoscopy can not only improve the positive detection rate of early cancer, but also display the tumor contour more clearly[61]. Tumors of the digestive tract have a high incidence. Siegel et al report that around 147,950 individuals will be diagnosed with colorectal cancer and 53,200 will die from the disease in 2020[62]. Digestive endoscopy is the most effective diagnostic method for early tumors of the digestive tract. Therefore, it is of great significance to apply digestive endoscopy in the high incidence area of digestive system tumors. It will help improve the diagnosis rate of early gastrointestinal tumors, benefit patients and improve the 5-year survival rate. The application of new technologies such as narrow band imaging, can assist endoscopists in discovering tiny lesions. Narrow band imaging is currently an extensively used diagnostic technique. Narrow band imaging can clearly show the morphology of mucosal capillaries and glandular duct openings on the mucosal surface[63]. If it is used in conjunction with magnifying endoscopy, the morphology of the mucosal surface can be displayed more clearly[64].

1.3.6. Pathology

Cancer pathological examination is one of the most important diagnosis methods, which is regarded as the “gold standard” of cancer diagnosis. Pathological examination can determine the diagnosis, tissue source, nature and scope of the tumor and provide an important basis for clinical treatment. For the examination method of pathological morphology, the first step is to observe of the pathological changes of the gross specimen, then lesion tissue is paraffin embedded, sliced and

made into histology slides for examination of the lesion with a microscope. Figure 1.5. shows the prepared paraffin embedded cancer tissue block and its histological image. Biopsy and immunohistochemistry are common pathology techniques.

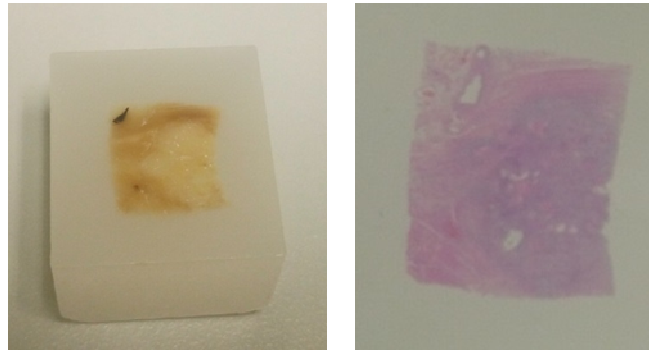


Fig. 1.5 Paraffin block of oral cancer tissue and hematoxylin-eosin (HE) staining slide.

Biopsy is a method in which a small piece of tissue is removed from the diseased part of the patient body or the specimen is surgically excised to make a pathological section and the changes in the morphological structure of the cells and tissues are observed to make it possible to determine the locations of the lesions. This is a common and accurate method for diagnosing tumors. In recent years, due to the improvement of various endoscopes and imaging diagnostic technologies, new techniques can not only directly observe the appearance of certain internal tumors, but also accurately excise samples, which further improves the development of biopsy techniques[64].

Immunohistochemistry is an important part of pathological examination that has developed rapidly in the past decades. It has been widely used in tumor research and diagnosis[65], [66]. Its principle is to use the specific binding reaction of antigens and antibodies to detect unknown antigens or antibodies in tissues, mainly

tumor related antigens, such as tumor differentiation antigens and tumor embryo antigens, to determine the origin and degree of differentiation to assist pathological diagnosis and differential diagnosis of tumors[53]. It has been possible to identify tumors whose origin is difficult to judge by many conventional methods with this technique.

1.4. Thesis Overview

This chapter has covered a brief introduction to the basic knowledge of the medical applications of THz techniques, especially in cancer detection and imaging related applications. There has also been an introduction to the general approaches to cancer diagnosis and imaging instruments.

Chapter 2 introduces THz generation and detection techniques. Information on THz-TDS systems is presented. Finally, a THz reflection system from Menlo and a homemade transmission system are introduced.

Chapter 3 mainly focuses on the data processing methods. Extraction of the refractive index and absorption coefficient for the transmission and reflection system will be presented in this chapter. Details on calibrating the baseline and the extraction of impulse function are presented as well.

Chapter 4 introduces the sensing of the cancer related antigen-epidermal growth factor receptor (EGFR), with a metamaterial biosensor. A bow-tie array structure metamaterial biosensor was designed and fabricated, which has the ability on EGFR detection. Gold nanoparticles are introduced to this measurement system to further increase the sensitivity.

Chapter 5 presents a multi-microfluidic-channel metamaterial biosensor for liquid sample sensing. This multi-microfluidic-channel structure can further improve the sensitivity and decrease the volume of the investigated sample required compared to the one-channel structure.

Chapter 6 is about THz cancer imaging. We propose a dehydrated biological tissue preparation method and apply this method to make dehydrated porcine samples and paraffin embedded oral cancer samples. THz images of oral cancer samples obtained with a THz-TDS transmission system are presented. A strategy to improve the image contrast for THz cancer imaging using a water-tissue-quartz sandwich structure geometry is proposed and introduced in this chapter.

Chapter 7 summarizes and concludes the key findings presented in this thesis.

2. Terahertz system

Our THz lab equipped with THz time-domain spectroscopy (THz-TDS) systems is the main platform for my research. The core components in a THz-TDS system include two photoconductive antennas functioning as the emitter and detector respectively, a femtosecond laser and a delay stage. Transmission and reflection geometries are both used to adapt to the different measurement demands. Details about the system will be introduced in this chapter.

2.1. THz generation and detection

2.1.1. THz generation

THz emitters can be divided into narrowband and broadband frequency emitters, according to the bandwidth of the generated THz signal. Typical narrow band THz sources include photomixing techniques[53], optical paramagnetic oscillation(OPO) systems[53], free-electron lasers(FELs)[67], backward wave oscillators(BWOs)[68], frequency multipliers and quantum cascade lasers(QCLs)[69]. The principles of QCLs and a technological analysis of them will be presented later. For a broadband THz emitter, one technique is to use optical rectification[70], whilst a more convenient generation method involves implementing a photoconductive antenna(PCA)[71], this will be introduced in the following part in detail.

PCAs are widely used as emitters in THz-TDS systems to generate broadband THz signals. The structure of this kind of antenna is illustrated in Fig. 2.1. This antenna consists of two metal electrodes, which are attached to the substrate. LT-GaAs and InGaAs, which have ultrashort carrier lifetimes and high mobilities, are commonly selected as the substrate. The two metallic electrodes are parallel to each other,

and a bias voltage is applied across them. The working principle is: a fs-laser beam is focused on the gap between the two electrodes on the substrate, exciting the electrons in the substrate to transfer them from the valence band to the conduction band. Next, these excited electrons in the substrate are accelerated by the bias voltage applied to the electrodes. A photocurrent will then be generated by the movement of the electrons, at the same time, some of the energy of the electrons will radiate as an electromagnetic wave which lies in the THz band. The intensity of the THz beam is proportional to the electric field in the gap and the fs-laser intensity. The bandwidth of the emitted THz beam is mainly restricted by the life time of the electrons and the duration of the fs-laser pulse.

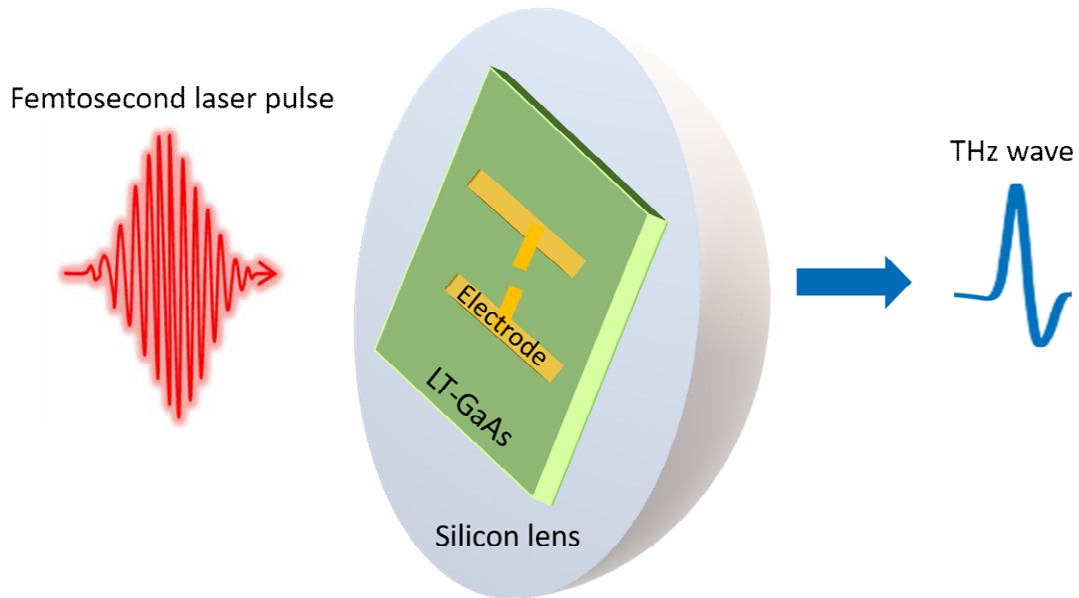


Fig. 2.1 A schematic of photoconductive switch functioned as a THz emitter.

In recent few years, the use of quantum cascade lasers (QCL) to generate THz signals has gained more and more attention[69]. The working principle of this technique is based on the intersubband transitions of the electrons in the periodic

quantum well structure in the semiconductor. The coherent single frequency radiation is generated by the transition of electrons from one quantum state to the next, which is at the same energy level. QCLs have attractive features including the wide tunability and overall high performances. However, for a long time QCLs have been limited for THz generation by the low operation temperature. In 2015, the Belkin group exhibited QCLs operated at room temperature in the THz spectral range, with a nearly 2mW output power and a significant tunability[72]. This is a big breakthrough for the development of THz QCL sources.

2.1.2. THz detection

THz detection techniques can be divided into two categories: incoherent detectors and coherent detectors. Coherent detectors can acquire the amplitude and phase information simultaneously, while incoherent detectors can only record the intensity. In a coherent system, the emitter and detector use the same fs-laser to provide a constant relationship between the pump and probe beam, such as electro-optic sampling [72], and PCA detectors[73], which will be introduced further. For incoherent detectors, Golay cells[74] and bolometers[75] are widely applied. The detection principle is based on thermal measurements. Continuous THz radiation causes temperature changes in these two devices which are then transformed into other measurable variations.

PCAs can also be implemented for measuring the broadband THz signal. The structure is similar to the emitter which has been described in Section 2.1.1. The difference is that no bias voltage is applied across the electrodes for the PCA detector. The detection process is that the fs-laser beam is pumped onto the gap between the antenna to transfer the electrons from valence band to conductive band.

The incoming coherent THz signal pushes the electrons to move between the antennas, thus a measurable photocurrent is generated. This photocurrent is proportional to the amplitude of the THz pulse. The electrons in the semiconductor have a short enough life-time to resolve the THz beam in the time domain. By adjusting the relative time delay between the THz pulse and fs-laser pulse using a delay stage, the whole waveform can be recorded[73].

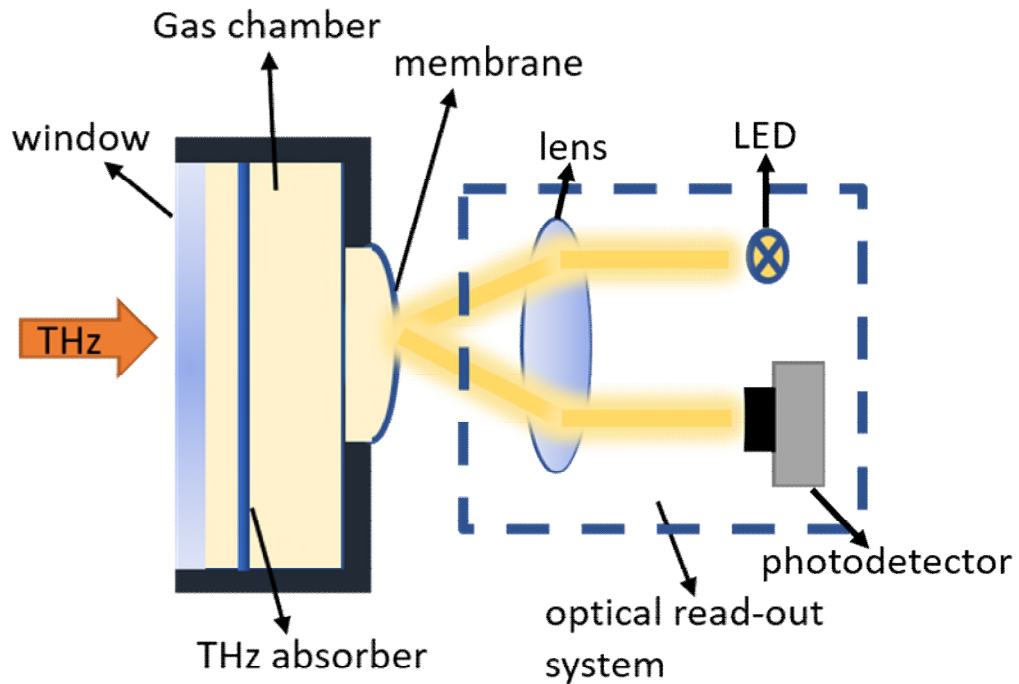


Fig. 2.2 A schematic of golay cells detector.

Golay cells contain a chamber filled with gas, an absorber and light reflection membrane (see Fig. 2.2). The absorber can absorb the energy of the incident THz radiation, this energy is then transformed into heat to induce the expansion of the gas changing the shape of the membrane. This shape change can be transferred into intensity via an optical read-out system. The advantage of the Golay cell is the high sensitivity and the broad bandwidth. However, the response is relatively slow

because of the transfer of energy into heat. The typical integration time is around 25ms[74].

2.2. THz time domain spectroscopy (THz-TDS) system

THz-TDS is the most commonly used technique for sample characterization. By Fourier transforming the acquired time-domain signal, the frequency-domain information can be obtained and consequently the spectrum can be analyzed. Figure 2.3 shows a schematic of a typical THz-TDS reflection system that consists of femtosecond pulsed laser, a delay stage, a photoconductive emitter and detector, optical lenses and an imaging window. Normally, the femtosecond pulses are generated by a Ti:sapphire or fiber laser: the wavelength of the laser light needs to be short enough to be able to excite the electrons in the semiconductor from the valence band to the conductive band. The emitted THz beam is focused by a silicon lens and then propagates through free space. In our reflection geometry, the THz beam is directed onto the quartz window with 30° incident angle. The window serves as the platform to support the sample. The detector receives the THz signal reflected by sample. With the movement of the delay stage, the whole time-domain waveform can be well recorded. The transmission geometry has a similar configuration to that of reflection, with the detector receiving the THz signal transmitted through the sample.

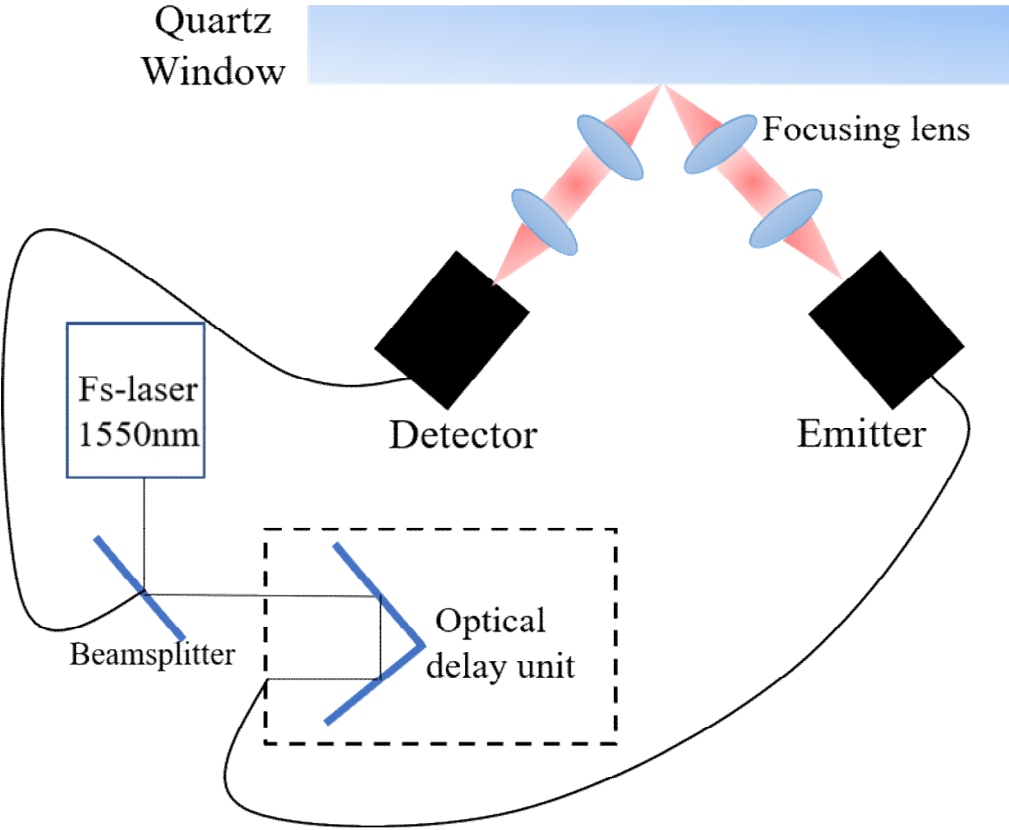


Fig. 2.3 A schematic of a fiber-based THz-TDS reflection system that consists of a femtosecond pulsed laser, delay stage, photoconductive emitter and detector, focusing lenses and an imaging window.

For this research, a commercial terahertz reflection imaging system and a homemade transmission THz system are used.

2.2.1. THz reflection system

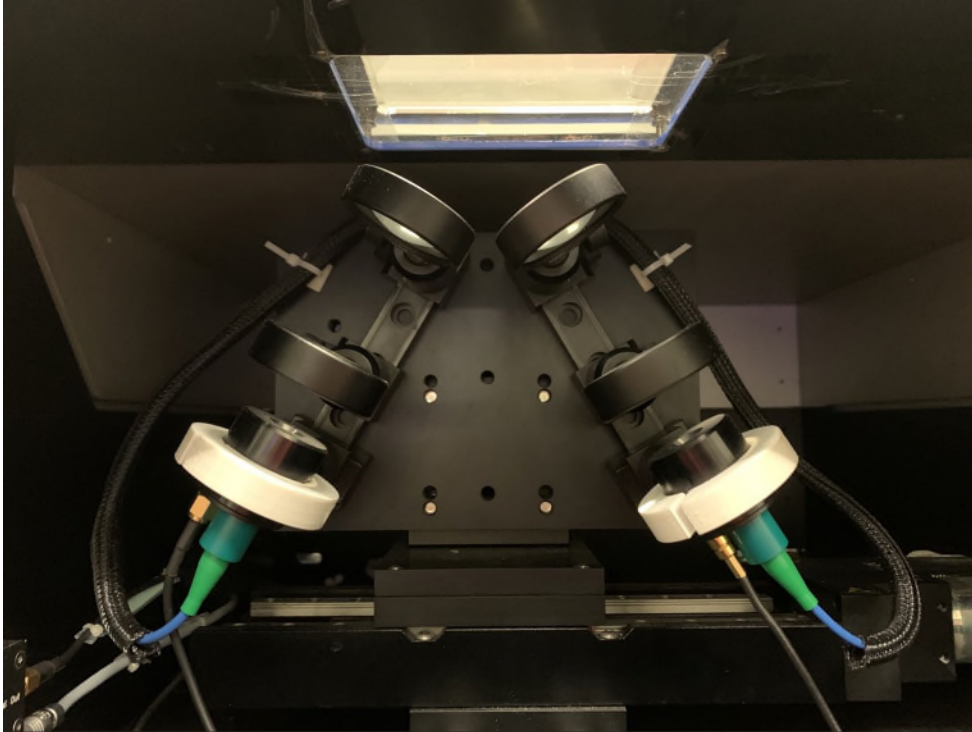


Fig. 2.4 Terahertz reflection imaging system.

Figure 2.4 shows the THz-TDS reflection system in our lab, which was purchased from Menlo Systems, Inc. It is fiber-based and pumped by a 1550nm laser. The semiconductor used in the PCAs to emit and detect the signals is InGaAs. The polarization state of the THz pulse can be switched between s- and p-polarizations. The imaging window can be replaced by prisms to adapt with the experimental demands. The detector and emitter are assembled on an X-Y moving stage. Imaging can be achieved by scanning in the x-y plane. **The diameter of the focal spot of the broadband THz beam onto the quartz imaging window is around 3 mm.**

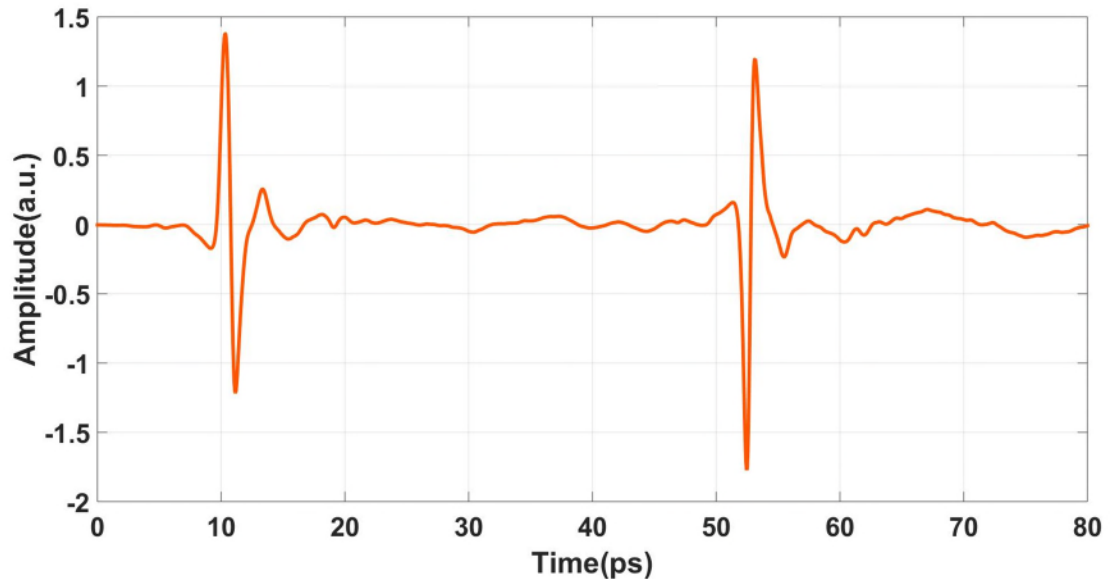


Fig. 2.5 THz time-domain signal of quartz window. The first pulse is from the bottom of the quartz window and second pulse is from the upper quartz-air interface.

This system offers a point-scan mode and an imaging mode. In the point-scan mode, the THz beam is fixed on a specific position of the sample. The measured length of the time-domain waveform is typically 80 ps, taking around 0.25s to acquire. In the imaging mode, the imaging speed is determined by the imaging resolution, in general, imaging a 10 mm*5 mm area takes about 35s to acquire, taking 1 mm steps in both X and Y directions.

Figure 2.5 shows the raw time-domain data measured from the quartz window alone, because only the second pulse contains object information, the first reflection pulse should be calibrated with the method introduced in Section 2.2 in the sample characterization stage.

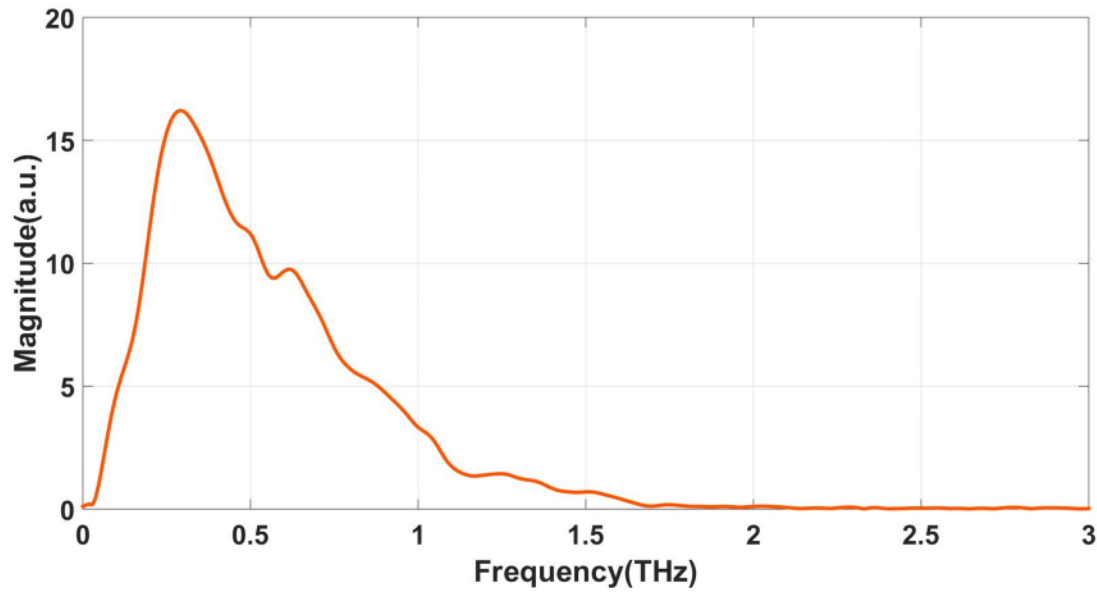


Fig. 2.6 THz frequency-domain signal. The Frequency domain signal is obtained in ambient air, and the pulse reaches the noise floor about 1.7 THz.

Figure 2.6 shows an example of the frequency-domain spectrum of the air-reflection after subtracting the lower air-quartz reflection.

2.2.2. THz transmission system

Figure 2.7 illustrates the free-space THz-TDS transmission system used in this work. The center wavelength of the laser is 800 nm and the pulse width is 100 fs. Apart from the laser, this system consists of a rapid scan delay (ScanDelay 50, APE Berlin, Germany), a long scan delay (Physik Instrument GmbH & Co.KG), and a pair of LT-grown GaAs photoconductive antennas (Menlo Systems TERA8-1, Martinsried, Germany). When it is in operation, the laser is incident onto the center of the H shape antennas, THz light is emitted and received. The sample is placed at the focal point and normal to the THz beam. There are four parabolic mirrors to collimate the the THz beam. The focal spot size of the THz light depends on the

frequency and is around 1 mm at 1 THz. The operational bandwidth of the setup is up to 3.5 THz.

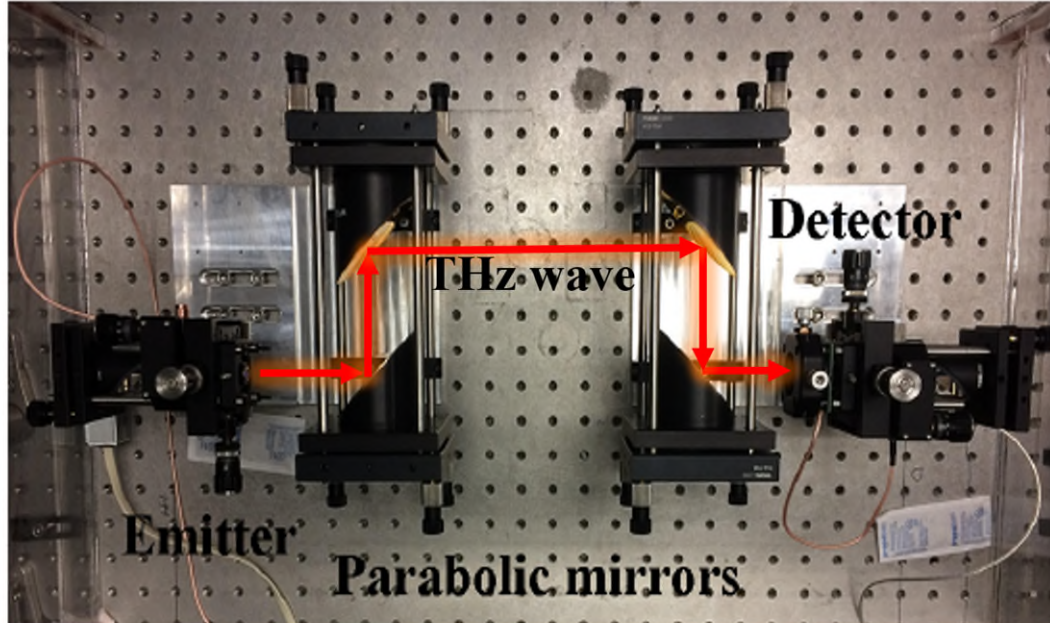


Fig. 2.7 A schematic of THz-TDS transmission system. The red arrows show the propagation of the THz beam.

The transmission system setup is covered with a sealed box to enable dry air purging. Usually, the system is purged with dry air and the relative humidity can be decreased to less than 5% in the chamber. Fig.2.7 shows the signal obtained at different relative humidities. The red signal for dry air has a greater amplitude and the oscillation following the main pulse is reduced at a lower humidity.

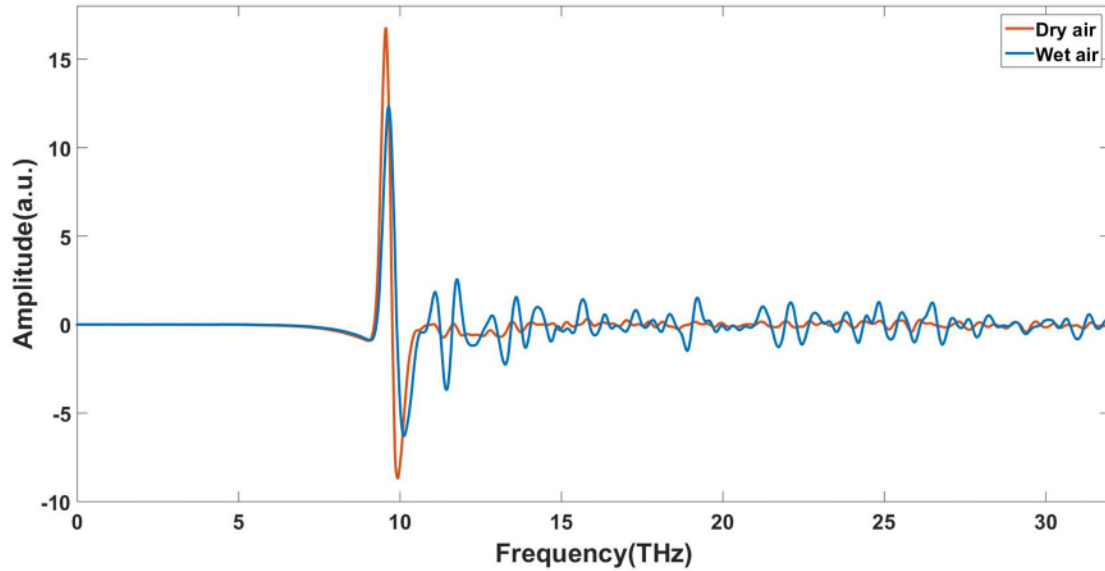


Fig. 2.8 THz time domain signals of dry air (less than 5% relative humidity) and wet air (70% relative humidity).

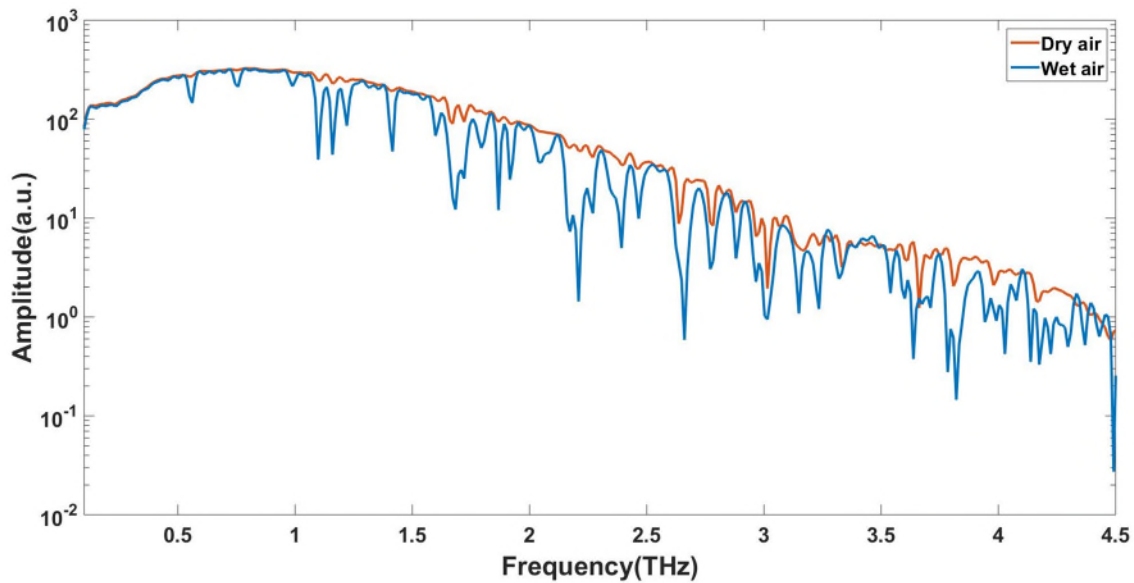


Fig. 2.9 THz frequency domain signals of dry air (less than 5% relative humidity) and wet air (70% relative humidity).

In figure 2.9, the frequency domain magnitudes of the air signals in the wet and dry air environments are shown. Because of the presence of water vapor, absorption

peaks can be observed at around 0.55THz, 0.75THz, 0.9THz and 1.1THz for the blue curve, which will affect the accuracy and sensitivity of the measurement. Therefore, keeping the relative humidity low during measurements is usually required to achieve a good accuracy and a high SNR.

3. Data processing method

3.1. Data processing in the transmission system

When an electromagnetic wave travels in a medium, the electromagnetic function is:

$$E(x, t) = E_0 \exp[i(\omega t - kx)] \quad (3.1)$$

in this function, E_0 is the initial electric field amplitude, ω is the angular frequency, t is time, x is the distance along the propagating direction and k represents wave vector. When the electromagnetic wave passes through a sample or medium, absorption occurs. This process can be written with the complex refractive index, \tilde{n} . It is related to the wave vector by the following equation:

$$\tilde{n} = n - i\kappa = \frac{kc}{\omega} \quad (3.2)$$

In the above function, n is the refractive index, c is the speed of light in a vacuum and κ is called the extinction coefficient. The real part of \tilde{n} describes the propagation phase change, while the imaginary part reflects the absorption during the propagation.

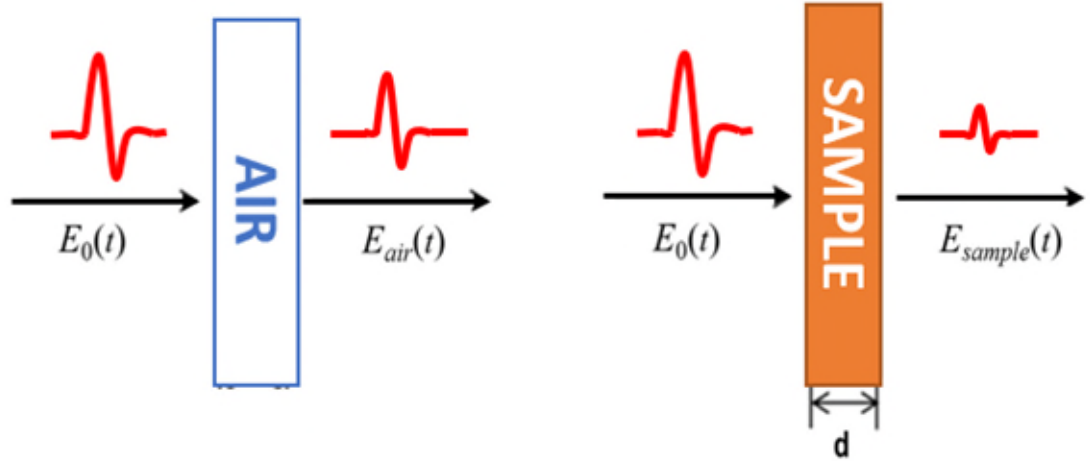


Fig. 3.1 Schematic of wave propagation in transmission geometry.

The measurement of samples in a transmission system is depicted in Fig. 3.1. Generally, the air signal (i.e. the transmission in the absence of the sample) is used as the reference. The air reference signal can be expressed by the following formula:

$$E_{air}(\omega) = E_0(\omega) \cdot \exp\left\{-i * d * \frac{\tilde{n}_{air}\omega}{c}\right\} \quad (3.3)$$

where $E_0(\omega)$ is the Fourier Transform of the incident terahertz wave $E_0(t)$. \tilde{n}_{air} is the complex refractive index of air, d is the thickness of the sample.

The THz signal transmitted through the sample is expressed by:

$$E_{sam}(\omega) = E_0(\omega) \cdot t_{as} \cdot t_{sa} \cdot \exp\left\{-i * d * \frac{\tilde{n}_{sam}(\omega)}{c}\right\} \quad (3.4)$$

in which \tilde{n}_{sam} is the complex refractive index of the sample material, t_{as} and t_{sa} are the transmission coefficients at the air/sample and sample/air interface, respectively.

The ratio between the electric fields after transmitted through the sample and air can be written as:

$$\frac{E_{sam}(\omega)}{E_{air}(\omega)} = t_{as} \cdot t_{sa} \cdot \exp\left\{-id \frac{(\tilde{n}_{sam} - \tilde{n}_{air})\omega}{c}\right\} \quad (3.5)$$

For normal incidence:

$$\tilde{n} = n - ik \quad (3.6)$$

$$t_{as} = \frac{2\tilde{n}_{air}}{\tilde{n}_{air} + \tilde{n}_{sam}} \quad (3.7)$$

$$t_{sa} = \frac{2\tilde{n}_{sam}}{\tilde{n}_{air} + \tilde{n}_{sam}} \quad (3.8)$$

Therefore,

$$\frac{E_{sam}(\omega)}{E_{air}(\omega)} = \frac{4\tilde{n}_{air}\tilde{n}_{sam}}{(\tilde{n}_{air} + \tilde{n}_{sam})^2} \cdot \exp\left\{-d \frac{\omega\kappa_{sam}}{c}\right\} \exp\left\{-id \frac{(n_{sam} - n_{air})\omega}{c}\right\} \quad (3.9)$$

The ratio between the electric fields can be represented by an amplitude term and a phase term as shown in Equation (3.10). A and ϕ can be acquired by comparing the measured sample and reference signals. The refractive index and the absorption coefficient can then be calculated using Equation (3.11) and (3.12).

$$\left\{ \begin{array}{l} \frac{E_{sam}(\omega)}{E_{air}(\omega)} = t_{as} \cdot t_{sa} \cdot \exp\left\{-id \frac{(\tilde{n}_{sam} - \tilde{n}_{air})\omega}{c}\right\} \\ \frac{E_{sam}(\omega)}{E_{air}(\omega)} = A \cdot \exp(-i\phi) \end{array} \right. \quad (3.10)$$

$$n_{sam} = 1 + \frac{c\phi}{d\omega} \quad (3.11)$$

$$\alpha_{sam} = \frac{2\omega}{c} \kappa_{sam} = -\frac{2}{d} \ln \left[\frac{(n_{sam} + 1)^2}{4n_{sam}} \cdot A \right] \quad (3.12)$$

3.2. Data processing in reflection system

The tissue imaging part of this work is mainly done with the reflection system. The data processing involves baseline calibration, deconvolution and the calculation of optical parameters. Details will be presented in the following section.

3.2.1. Baseline subtraction

As shown in Figure 3.2a, the detector receives two THz reflections from the quartz window. One comes from the lower surface of the quartz and the other comes from the upper surface of the quartz. The lower reflection, named the baseline in our studies, contains fluctuations due to the systematic artifacts and the water vapors, which interfere with the upper reflection in the time-domain. Therefore, it is necessary to subtract the baseline from the detected signal to extract the pure upper reflection. The baseline can be measured by placing a piece of thick quartz on top of the imaging window. The second reflection can then be eliminated due to the index matching. Figure 3.3 shows the measured time-domain signals with and without the additional quartz on top of the window. The measured baseline only contains the lower air-quartz reflection, which is identical to the first pulse of the measured air signal (without subtracting the baseline). The tiny reflection at the second pulse position in the baseline signal comes from the imperfect contact between the quartz window and the top quartz plate. For imaging applications, the unevenness of the quartz window may introduce phase shifts and amplitude modifications for signals obtained at different spatial positions. The detailed calibration of these systematic errors can be found in the work by Chen et al[76].

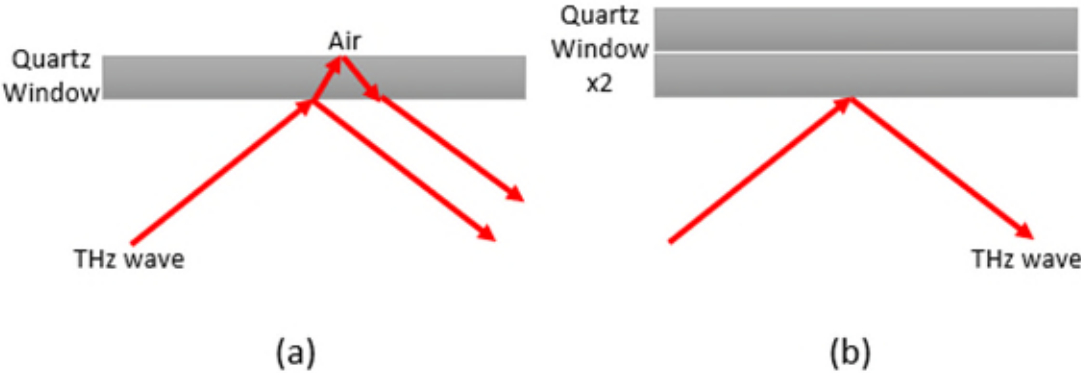


Fig. 3.2 Air and baseline measurement with reflection system.

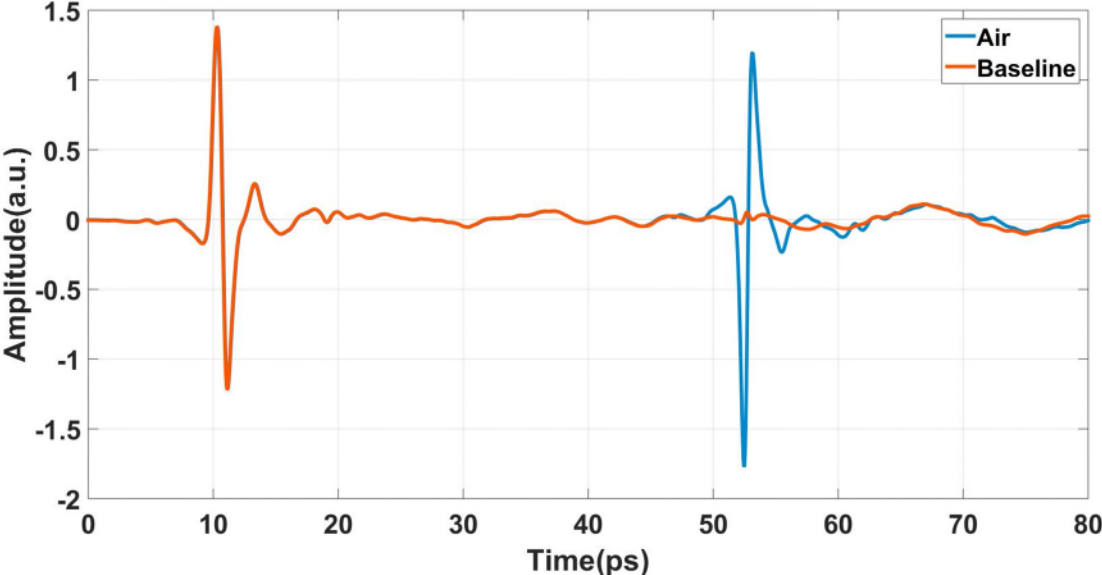


Fig. 3.3 Time-domain measurement of air and baseline from reflection system.

3.2.2. Impulse function

In thin-film analysis or in vivo skin studies, one usually performs a deconvolution of the signal and calculates the impulse function to better investigate the layered structure. The impulse function is a well-known approach to removing system

defects and extracting the sample features. The function can be calculated using equation 3.14, which is the inverse Fourier transform of the transfer function shaping with a double Gaussian filter (DGF)

$$\text{Impulse function} = \text{IFFT} \left[\text{DGF}(\omega) \times \frac{\text{FFT}(E_{sam}(t))}{\text{FFT}(E_{ref}(t))} \right] \quad (3.13)$$

where

$$\text{DGF}(\omega) = \left(e^{-\frac{H^2\omega^2}{4}} - e^{-\frac{L^2\omega^2}{4}} \right) e^{i\frac{T\omega}{2}} \quad (3.14)$$

where H and L define the high- and low-cut off frequencies of the filter. T is the length of the measured time-domain signals. The filter applies to the ratio between sample and reference removes the shape dependence of the THz pulse. The double Gaussian filter is selected to remove both high and low frequency noise. In this way, the impulse function only contains the high SNR region of the spectrum and eliminates the influence of the system and environment. Some small features in the impulse function can be seen more clearly than that in the raw signals, such as the multiple thin film reflections.

Figure 3.4 (b) shows the impulse function of an air reflection. We can see that the two-layer structure is much clearer in the impulse function than in the raw signal, making it possible to perform a more accurate calculation of the thickness of each layer.

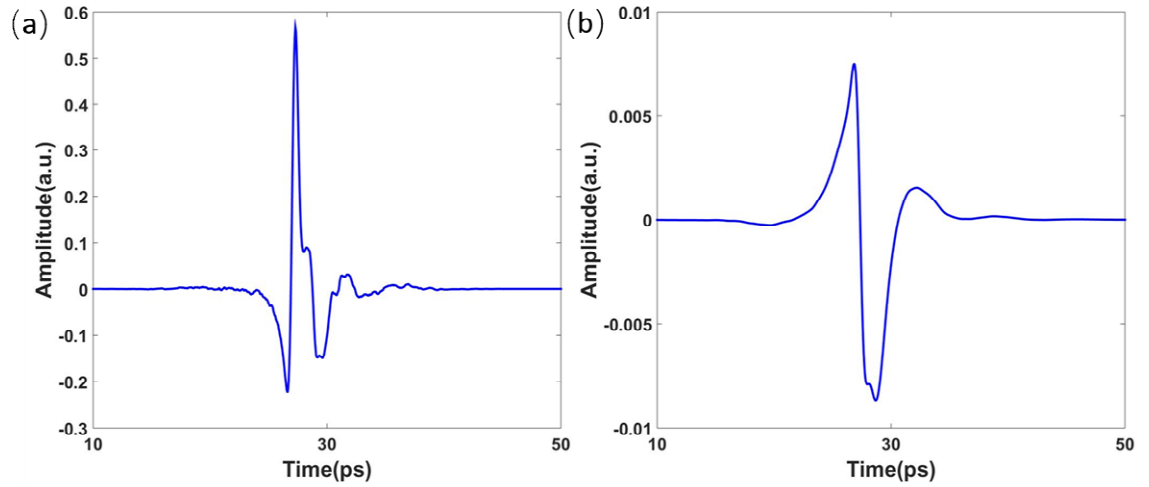


Fig. 3.4. (a)Time domain signal and (b)impulse function of human skin with THz reflection geometry.

3.2.3. Calculation of the refractive index and absorption coefficient

Terahertz reflection geometry can be used to measure highly absorptive samples, which are challenging to measure in transmission geometry. For the reflection geometry, the refractive index and absorption coefficient can be determined from the reflection ratio R , represented in Equation 3.15:

$$\begin{aligned}
 R(\omega) &= \frac{E_{sam}(\omega)}{E_{air}(\omega)} = \frac{r_{qs}}{r_{qa}} \\
 &= \frac{\tilde{n}_{qua} \cos\theta_{qua} - \tilde{n}_{sam} \cos\theta_{sam}}{\tilde{n}_{qua} \cos\theta_{qua} + \tilde{n}_{sam} \cos\theta_{sam}} \cdot \frac{\tilde{n}_{qua} \cos\theta_{qua} + \tilde{n}_{air} \cos\theta_{air}}{\tilde{n}_{qua} \cos\theta_{qua} - \tilde{n}_{air} \cos\theta_{air}}
 \end{aligned} \quad (3.15)$$

Rearranging Equation 3.15 we can express $\tilde{n}_{sam} \cos \theta_{sam}$ as:

$$\begin{aligned} \tilde{n}_{sam} \cos \theta_{sam} &= \tilde{n}_{qua} \cos \theta_{qua} \left(\frac{\tilde{n}_{qua} \cos \theta_{qua} (1 - R) + \tilde{n}_{air} \cos \theta_{air} (1 + R)}{\tilde{n}_{air} \cos \theta_{air} (1 + R) + \tilde{n}_{qua} \cos \theta_{qua} (1 - R)} \right) \\ &= \tilde{X} \end{aligned} \quad (3.16)$$

Utilizing Snell's Law,

$$\tilde{n}_{air} \sin \theta_{air} = \tilde{n}_{qua} \sin \theta_{qua} = \tilde{n}_{sam} \sin \theta_{sam} \quad (3.17)$$

Equation 3.17 can be expressed as:

$$\tilde{n}_{sam}^2 (1 - \sin^2 \theta_{sam}) = \tilde{n}_{sam}^2 - \tilde{n}_{air}^2 \sin^2 \theta_{air} = \tilde{X}^2 \quad (3.18)$$

The sample complex refractive index can be expressed as:

$$\tilde{n}_{sam} = \sqrt{\tilde{X}^2 + n_{air}^2 \sin^2 \theta_{air}} \quad (3.19)$$

The refractive index and extinction coefficient can be calculated as the real and imaginary parts of \tilde{n}_{sam} , respectively

3.3. Summary

In this chapter, we explained how the THz time-domain and frequency-domain raw signals obtained from transmission and reflection measurements are analyzed. The procedures for data and sample characterization were also introduced.

4. Detection of EGFR with terahertz metamaterial biosensor

4.1. Introduction

The epidermal growth factor receptor (EGFR) is a transmembrane protein which plays an important role in the occurrence and development of many kinds of cancers, such as gastrointestinal cancer, lung cancer and head and neck epithelial cancer[77]–[79]. Traditional EGFR detection methods mainly include direct sequencing of polymerase chain reaction (PCR), denaturing high performance liquid chromatography (DHPLC), and immunohistochemistry [80], [81]. Quick and sensitive detection of EGFR is important for the diagnosis and prognosis of EGFR related diseases. However, most of these traditional methods cannot realize high detection speed and sensitivity at the same time.

Terahertz (THz) techniques have been recently used in rapid and label-free identification of biomolecules and proteins. In particular, metamaterial biosensors were commonly used in the detection of biomolecules and cancer related antigens[28]. Compared with traditional detection methods, terahertz metamaterial biosensors are a promising technique for time-saving, low-cost, highly sensitive and non-destructive detection of trace amount biological samples.

Metal nanoparticles have excellent physical and chemical properties and biocompatibility, which have been widely used in molecular imaging, targeted drug development, imaging agent and photothermal therapy[82]–[84]. Nanoparticles with different shapes and sizes can also be developed according to different application purposes. In recent studies, researchers used gold nanoparticle to

combine with specific antibody or ligand to detect target biomolecules based on THz metamaterial[27],[28], which can further increase the sensitivity and decrease the dosage of target biomolecules. Nonetheless, the effect of the size of GNPs on the sensitivity enhancement has not hitherto been revealed.

In this chapter, we show the THz experiment of EGFR protein based on a bow-tie array metamaterial biosensor. First, we simulated and fabricated a bow-tie metamaterial biosensor. Then the EGFR antibodies were combined with gold nanoparticles with different sizes to react with EGFR proteins on the metamaterial biosensor. The metamaterial resonance frequencies for EGFR detection based on antibodies with and without gold nanoparticles (GNPs) were calculated to verify the enhanced sensitivity and sensing specificity. The nanoparticle size effect on the sensing sensitivity was also analyzed.

4.2. **Methods**

4.2.1. Metamaterial simulation

The bow-tie array metamaterial can achieve stronger electric field enhancement and localization compared to the square or rectangular structure, which is suitable for sensing application. The bow-tie array metamaterial design is adopted in this study, with the unit cell shown in the inset of Fig. 4.1. The 50- μm -side /10- μm -gap bow-tie array metamaterial (equilateral triangles, 100-nm-thick Au, fabricated on a 2-mm-thick quartz substrate) was simulated by the frequency domain solver in the CST Microwave Studio. In the simulation, the quartz substrate was modeled as a lossless dielectric with dielectric permittivity $\epsilon = 4.41$, and the Au conductivity was set as 4.56×10^7 S/m. The amplitude transmission $t(\omega)$ was obtained by the

following equation: $t(\omega) = |\tilde{E}_s(\omega) / \tilde{E}_r(\omega)|$, where $\tilde{E}_s(\omega)$ and $\tilde{E}_r(\omega)$ are the fast Fourier transformed sample and reference THz signals, respectively, ω is the angular frequency. An identical quartz substrate without the metamaterial was adopted as the reference.

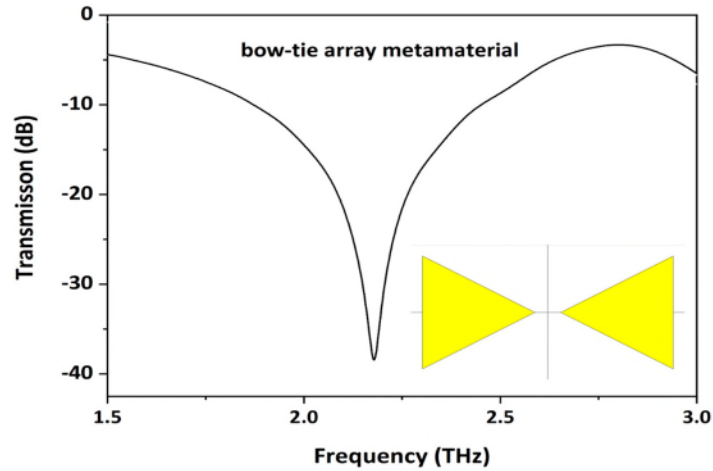


Fig.4.1. Simulated transmission spectrum of the bare bow-tie array metamaterial.

The simulation results are shown in Fig. 4.1. The 50- μm -side /10- μm -gap bow-tie array metamaterial shows a resonance peak at 2.15 THz.

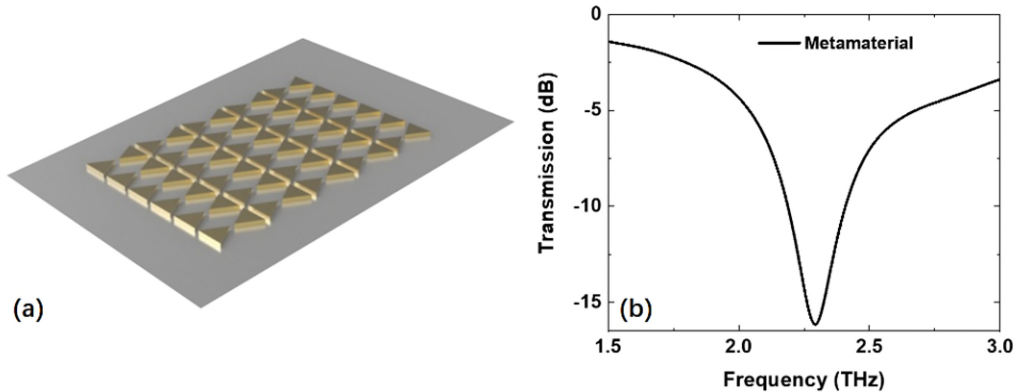


Fig.4.2. (a) Structure of the bow-tie array metamaterial. (b) Transmission amplitude spectrum of the fabricated bow-tie array metamaterial.

4.2.2. Metamaterial fabrication

The bow-tie arrays were fabricated on the 2-mm-thick z-cut quartz substrate by standard photolithography and metal thermal evaporation process. A 2 mm high transparent crystal quartz substrate was First, the quartz substrate was cleaned under the ultrasonic treatment with acetone and isopropyl alcohol (IPA) for 10 min, then washed with double distilled water, and dried by nitrogen. Then, positive photoresists were deposited onto the quartz and patterned the designed bow-tie array structure, details of the photolithography show in Fig. 4.3. 20 nm of chromium and 100 nm of gold (Au) layers were deposited separately with the rate of 1 Å/s by metal thermal evaporation process. We used a chromium sublayer to increase the adherence of the gold layer to the surface of quartz substrate. For the lift-off process, the fabricated device was immersed with acetone under ultrasonic treatment first and washed with double distilled water to finish.

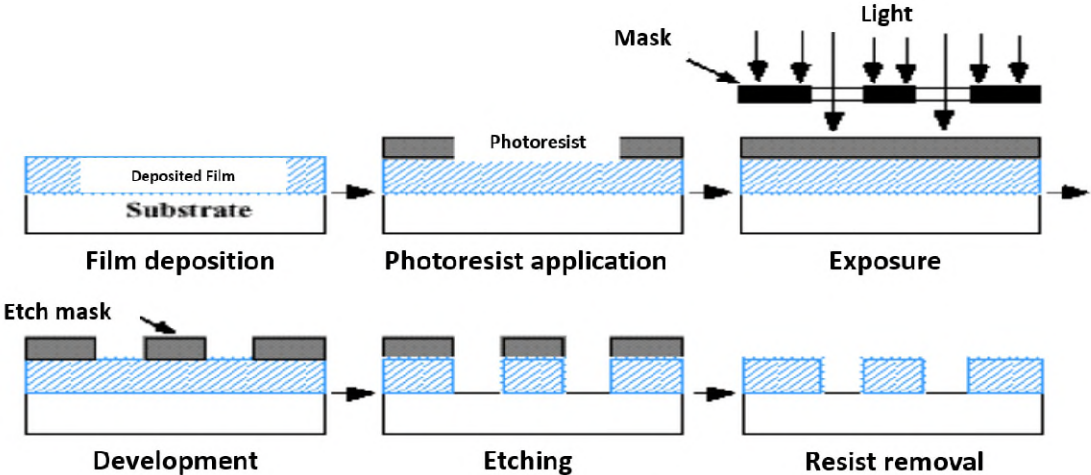


Fig.4.3. Photolithography procedures including film deposition, photoresist application, exposure, development, etching and resist removal.

The bow-tie array structure used for the base of our sensor is illustrated in Fig. 4.3. Each bow-tie consists of two identical equilateral triangles of side 50µm and there is a 10 µm gap at the center of each unit. 2-mm-thick quartz was adopted as

the substrate. The size of the sensor was about 8 mm by 8 mm. The total number of bow ties is 75×133 . The unit size is $106.6 \mu\text{m} \times 60 \mu\text{m}$. The single bow-tie structure is the unit of the array for the designed metamaterial. There is no resonance in a single unit structure. Metamaterials are electromagnetic materials with periodic arrangements of sub-wavelength structures, which exhibit the localized electromagnetic field enhancement at a specific resonance frequency and are particularly sensitive to changes in the dielectric properties of the surrounding environment. The THz beam size from our system is around 4-5 mm. The size of the metamaterial sensing area large enough for the THz beam to be completely incident on the sensor. The experimental spectrum of the fabricated metamaterial is shown in Fig. 4.4, with the resonance frequency at 2.292 THz and transmission dip amplitude of 16.15 dB. (see Fig. 4.2) The full width at half maximum (FWHM) is 0.117 THz. The dynamic range of the signal transmitted through a 2mm thick quartz wafer, which was used as our reference, is 30 dB at 2.3 THz, sufficient to resolve the attenuation of 16.15 dB at the resonant dip. The minor distinctions between the simulated and experimental data are mainly due to errors in fabricating the metamaterials.

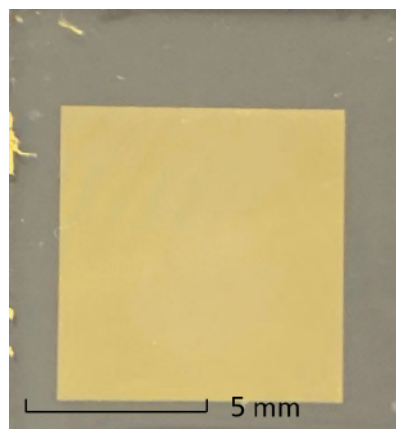


Fig.4.4. Photograph of fabricated metamaterial biosensor.

The polarization of the incident THz field was vertical to the long axis of the unit. When biosensing was performed, we used a holder to fix the sensor in order to keep the same position every test. Thus, polarization will be the same every test, it will not cause the accuracy of the test.

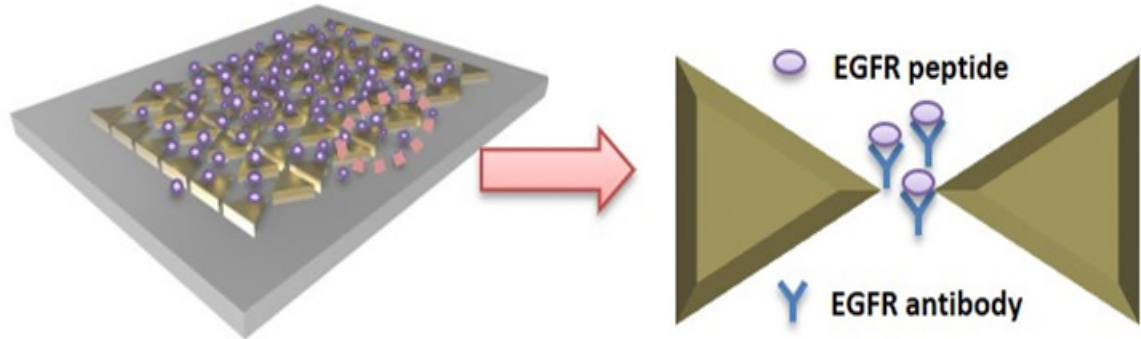


Fig. 4.5. Schematic diagram of the metamaterial biosensor for EGFR detection.

4.2.3. Sensing experiment procedure

The sensing experiments based on the fabricated sensor were conducted in a THz time-domain transmission system. More details of the system are given in a previous publication from our group [28]. The sensor was placed in the focal point of THz beam. The transmission amplitude spectra were measured. Before the Fourier transform, a 40 ps window is applied to the time-domain waveform to select the first transmitted main pulse and zero padding is applied to extend the signal length to 10 ns, providing a frequency resolution of 0.1 GHz.

For EGFR detection, the metamaterial was functionalized with EGFR antibodies and GNPs to improve the sensitivity. First of all, we implemented the EGFR sensing experiment with only EGFR antibody (Ab) functionalized metamaterial. The procedures were as follows. Firstly, 10 ul EGFR solution was added onto the bare

metamaterial sensor (without Ab functionalization), air dried and measured as the control. The concentration of EGFR solution ranged from 10 fM to 10 pM. In order to detect the binding state of EGFR and Ab, we added 10 μ l Ab solutions (10 pM) onto the sensing area of the sensor and incubated for 30 min. Then, 10 μ l EGFR of different concentrations were mixed with the Ab on the sensor and stored at 4 °C to bind with Ab, air dried and measured by the THz time-domain transmission system. The mean value of three repeated measurements for each concentration was adopted for further analysis.

Moreover, the GNPs were further introduced to improve the sensitivity. The schematic diagram for EGFR detection based on bow-tie metamaterial sensor with the addition of GNPs and antibodies is shown in Fig. 4.5. The experimental procedures are as follows. Firstly, the GNPs were functionalized with polyethylene glycol (PEG) (Laysan Bio Inc) via the thiol group. EGFR antibodies were linked to the GNPs with the PEG linker molecule, whose N-Hydroxysuccinimide (NHS) ester group can form covalent bonds with EGFR antibody. 10 nM GNP-PEG were mixed with 100 nM EGFR antibody solution. The mixture was incubated at room temperature for 120 min to form the nanoparticle-antibody complexes. Unreacted EGFR antibody was removed by centrifugation at 15000 rpm for 30 min. After removal of the supernatant, purified EGFR antibody modified GNPs (GNP-Ab) were acquired.

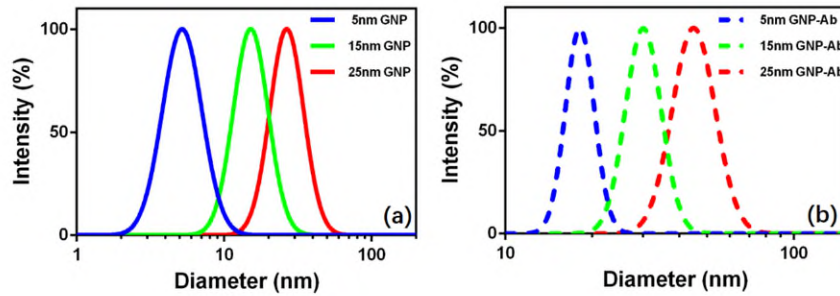


Fig.4.6. (a) DLS results of bare GNPs with different diameters. (b) DLS results of EGFR antibody modified GNPs with different diameters.

Dynamic light scattering (DLS) measurements were carried out to characterize the GNP modification results by EGFR antibodies. The Gaussian fitting results of the diameter measurement data are shown in Fig. 4.6. The intensity is normalized to 100%. The GNPs with mean diameters of 5 nm, 15 nm and 25 nm were adopted and compared in this study (Fig. 4.6a). After EGFR antibody modification, the prepared GNP-Ab increases in size compared to the bare GNP. The DLS results of EGFR antibody modified GNPs with different diameters are shown in Fig. 4.6b. An increase in diameter of nearly 10-15 nm is seen compared to the bare GNPs for different nanoparticle sizes, which demonstrates the successful modification of GNPs by the EGFR antibodies.

The GNP concentration was determined by the molarity of Au used for preparation and verified by the inductively coupled plasma mass spectrometry. For the GNP-Ab solution, the GNPs with bigger diameter may contain more antibodies due to the larger surface area for antibody modification, but it is difficult to measure the exact antibody molar numbers on the GNPs. Here the molarity of GNP was adopted to represent the GNP-Ab concentration. To compare the resonant frequency shifts of GNP and GNP-Ab with different diameters, we prepared GNP or GNP-Ab solutions and diluted them to the concentration of 10 pM. 10 μ L GNP or GNP-Ab solution (10 pM) with different GNP diameters was dropped on the sensor

center and air dried for detection. For EGFR detection, we dissolved EGFR antibody modified GNPs with PBS and diluted to 10 pM. The GNP-Ab modification procedures are nearly the same as EGFR detection with only antibody functionalization (without GNP). Firstly, 10 μ l GNP-Ab solution (10 pM) was dropped on the sensing area of metamaterial and incubated for 30 min. After incubation, we deposited 10 μ L EGFR solutions of four different concentrations on the sensor and stored at 4 $^{\circ}$ C. The THz transmission responses were measured when the reaction was completely finished. For comparison, the THz transmission measurements of bare GNP or GNP-Ab with different diameters (10 μ L solution (10 pM) dropped on the metamaterial without EGFR addition) were also implemented. The average result of three repeated responses for each measurement was used and new sample was added for each repeated experiment.

4.3. Results

4.3.1. EGFR detection results with Ab functionalized sensor

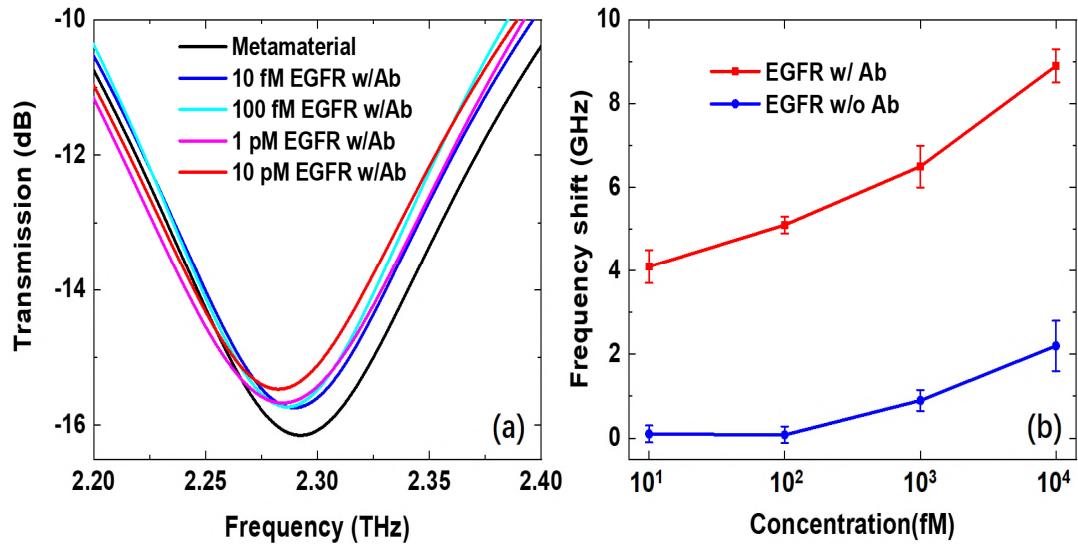


Fig. 4.7. (a) The transmission amplitude spectra of EGFR detected with Ab functionalized sensor. (b) The resonance frequency shift of EGFR with bare sensor (blue line) and with Ab functionalized sensor (red line).

The transmission amplitude spectra of the EGFR detected metamaterial biosensor is shown in Fig. 4.7a. The resonance frequency of the EGFR antibody is 2.292 THz, when the concentration is increased from 10 fM to 10 pM (by tenfold scaling), the resonance frequency red-shifts as illustrated in Fig. 4.7a. Figure 4.7b compares the resonance frequency shift based on the sensor w/o and w/ EGFR antibody. The sensor w/ Ab demonstrated larger detection sensitivity, and nearly a 10 GHz resonance frequency shift for 10 pM EGFR can be obtained, while only 2 GHz shift of the same amount can be obtained without Ab functionalization. The detection limit of Ab functionalized sensor is around 10 fM, but the bare sensor is larger than 100 fM.

4.3.2. Bare GNPs detection

GNPs have much higher refractive index compared with biomolecules, which could provide a larger frequency shift range based on THz metamaterial when biological samples are combined with GNPs. To further investigate the sensitivity enhancement effect of the GNPs, we compared the GNP solutions at concentration of 10 pM with mean diameter of 5 nm, 15 nm and 25 nm, respectively.

GNP solution were diluted to 10 pM. Then, 10 μ l diluted GNP solutions with diameter of 5nm, 15nm and 25nm were evenly injected at the center of the metamaterial biosensor and air dried, respectively. The transmission results are shown in Fig. 4.8. Compared to the metamaterial sensor, the resonance frequency with GNPs has a red-shift tendency. The 25-nm-diameter GNPs cause the largest resonance frequency shift: a red-shift of \sim 12.5 GHz was observed. While the 5-nm-diameter and 15-nm-diameter GNPs only have around 2.2 GHz and 6.7 GHz frequency shift, respectively.

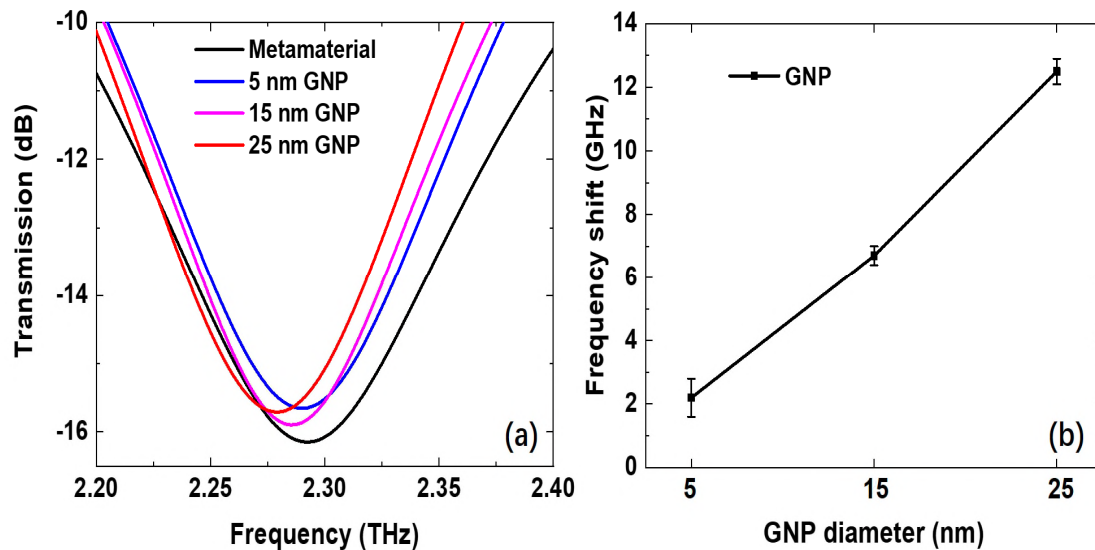


Fig. 4.8. The transmission amplitude spectra of GNPs with diameter of 5nm, 15nm and 25nm.

4.3.3. Connection of GNP with EGFR antibody

After comparing the bare GNPs with different diameters, we connected the GNP with EGFR Ab. The prepared GNP-Ab has a size increase compared with the bare GNP. Nearly 10-15 nm increase of the diameter can be seen with the dynamic light scattering (DLS) characterization, see Fig. 4.3.

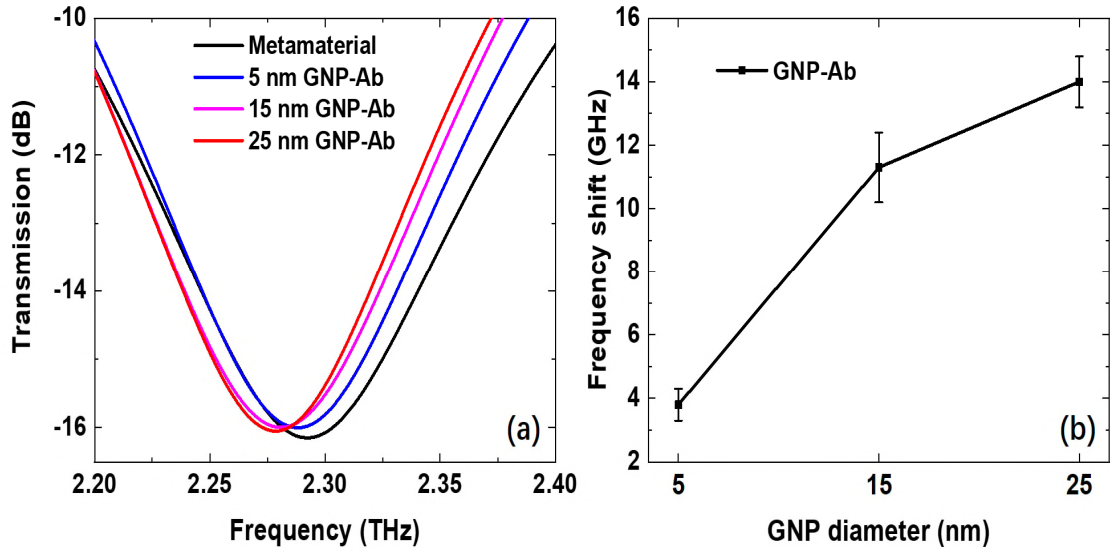


Fig. 4.9. The transmission amplitude spectra of GNP-Ab with the nanoparticle diameter of 5 nm, 15 nm and 25 nm at the concentration of 10 pM .(b) The resonance frequency shift of GNP-Ab with different GNP diameters.

10 μ L GNP-Ab solutions with different GNP diameters at concentration of 10 pM were dropped on the sensing area of metamaterial and then incubated for 30 min. The sensing experimental results are shown in Fig 4.9. The GNP-Ab with bigger GNP diameter causes a larger resonance frequency shift. Compared to the resonance frequency of metamaterial, 5 nm GNP-Ab can cause a frequency shift of around 3.8 GHz, while 15 nm and 25 nm GNPs have frequency shifts of 11.3 GHz and 14 GHz, respectively.

4.3.4. EGFR detection results with GNP-Ab functionalized sensor

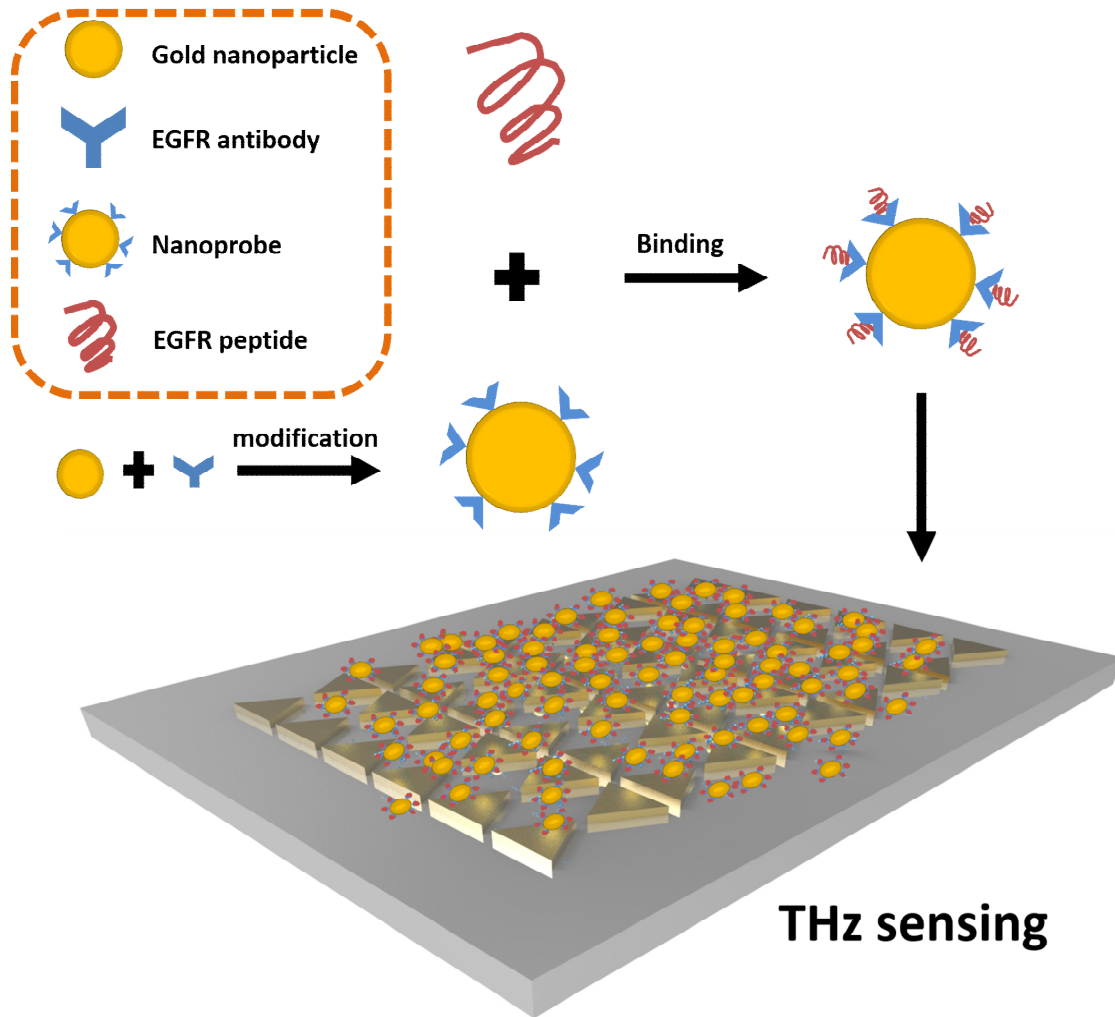


Fig. 4.10. Schematic diagram of the metamaterial biosensor for EGFR detection with GNP enhancement.

To further evaluate the sensitivity enhancement effect of GNP-Ab, we used the same experiment procedures as the EGFR detection with Ab functionalized sensor (see Fig. 4.10). For comparison, the resonance frequency shift results for EGFR detection without GNP (only Ab functionalization) are also listed in Fig. 11d. Compared to the resonance frequency of metamaterial, the sensors functionalized

by GNP-Ab with GNP diameters of 5 nm, 15 nm and 25 nm have resonance frequency shift of 15 GHz, 36.5 GHz and 39 GHz for 10 pM EGFR, respectively. However, only 8.9 GHz shift can be obtained with only Ab functionalization. The GNP-Ab functionalized metamaterial has a larger frequency shift range and a higher detection sensitivity for EGFR detection compared to the only Ab functionalized metamaterial. Furthermore, the metamaterial functionalized with GNP-Ab of bigger GNP diameter achieves a larger resonance frequency shift.

The measurement results show the strong ability for sensitive detection of trace volume EGFR solutions with our designed THz metamaterial biosensor. The proposed strategy with GNP-Ab modification can significantly increase the detection sensitivity.

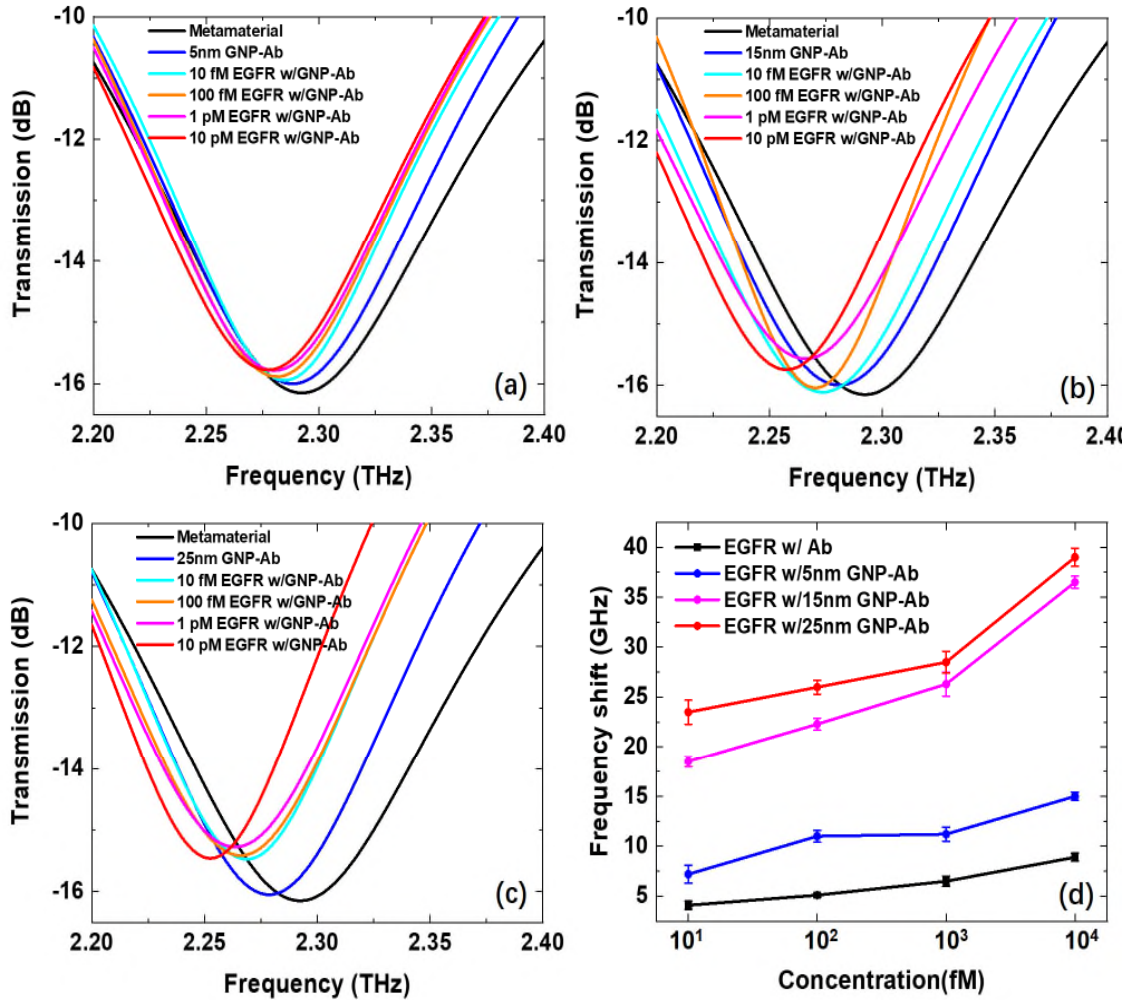


Fig 4.11. (a) The transmission amplitude spectra of EGFR detected with 5 nm GNP-Ab functionalized sensor. (b) The transmission amplitude spectra of EGFR detected with 15 nm GNP-Ab functionalized sensor. (c) The transmission amplitude spectra of EGFR detected with 25 nm GNP-Ab functionalized sensor. (d) The resonance frequency shift results for EGFR detection based on the metamaterial functionalized with Ab (orange line), 5nm GNP-Ab (purple line), 15nm GNP-Ab (light blue line), 25nm GNP-Ab (dark blue line), respectively.

The reasons for the sensitivity enhancement effects of GNP-Abs with different GNP diameters are as follows. The metamaterial has strong electromagnetic field enhancement and localization and is highly sensitive to any fluctuations in

dielectric properties on the surface [77]–[79]. In metamaterial sensing applications, the resonant frequency shift is mainly related to the real part of the complex refractive index of the sample being sensed [85]. Metal nanoparticles usually have high refractive index and can help achieve higher sensing sensitivity when binding to biological samples. The GNP-Ab and EGFR complexes can be regarded as the isotropic medium film based on the effective medium theory [92]. A larger resonance frequency shift would be detected with a thicker sample film on the metamaterial [33]. An increase in GNP diameter could be regarded as a way to achieve a larger average sample thickness, which leads to greater resonance frequency shift. Furthermore, owing to the differences of the surface areas of GNP with different sizes, the antibodies on GNPs with different diameters are different. The GNPs with bigger diameter may contain more antibodies on their surface. This is also a secondary factor for the larger enhancement effect with bigger GNPs. It is not beneficial for the GNP size to become too big (usually < 50 nm) due to the aggregation effect, because aggregations of GNP are generally too large to disperse at the strong field areas on the metamaterial [92].

In previous studies, the sample is usually measured with the metamaterial sensor only and the sensitivity of the sample is not enough for clinical use [28]. Our proposed GNP assisted metamaterial biosensor requires less sample volume to realize high sensitive sensing, which is highly desirable for the very costly and precious samples. This detection strategy can be applied to different metamaterial designs and other frequency bands. The sensing ability can be further improved by optimization of the MM structure. Moreover, the microfluidic channels can be introduced to further improve the sensitivity. As for the applications of this

metamaterial biosensor, the sensitivity and specificity of the biosensor can be further improved by optimizing the structure parameters to match the specific resonant frequencies of the biomolecules. Apart from the biological applications on protein solutions, the designed metamaterial sensor can be applied in a wide range of areas, such as dried bacteria sensing, cancer cells sensing and even non-biological organic matters sensing. In the future we hope to be able to do a comparison with clinical data-this would require extracting certain cancer biomarkers from serum or other clinical samples.

4.4. Summary

In this chapter, we designed and fabricated a bow-tie array terahertz metamaterial biosensor and functionalize the sensor with EGFR specific antibody and GNP of different diameters. We detected the EGFR protein of different concentrations and their binding state with specific Ab with the metamaterial sensor. The resonance frequency shift increases with increasing EGFR concentration. The GNP-Ab functionalized sensor with larger GNP diameter shows a better sensing sensitivity. GNP aided metamaterial biosensor has the ability to perform quantitative EGFR measurements sensitively. The proposed strategy has great potential for clinical use in EGFR detection.

5. Multi-microfluidic-channel metamaterial biosensor

5.1. Introduction

Metamaterial (MM) sensors are widely applied for detection of biological samples. They can react sensitively to the tiny variations of the dielectric properties on the top surface. The electrical field at some special area will strongly enhance as well[85]. This kind of feature can realize label-free detection of a small amounts of bio-samples. The vibrational and rotational energy bands of many biomolecules are located in the terahertz frequency range[86], [87]. Terahertz metamaterial biosensors have merits among these two aspects, which has been investigated a lot in the recent years[88]–[97]. Many kinds of structures has been designed and applied to many types of bio-samples, such as proteins, genes and bacteria [96], [97]. However, the high absorption of water will decrease the sensitivity of metamaterial. A majority former research focused on solid samples being dehydrated or with a low hydration level[89]–[96].

Water is the most important ingredient for human beings and essential for biochemical reactions, so to design a device which can detect liquid bio-samples is necessary. Microfluidic devices can realize tiny liquid sample detection and avoid the influence of the strong absorption of liquid samples. Furthermore, microfluidic devices are low cost. Recently, microfluidic chips have been widely combined with metamaterial in many terahertz biological research. However, most such sensors only have one channel at the surface of the metamaterial[98]–[105]. The sensitivity can be further improved by concentrating the liquid only in the field-enhancing

regions For example, the near-field microfluidic MM chips (employing the near-field coupling between the metal-atoms and the local THz emission) were proposed to achieve small volume liquid sample detection[106], [107]. However, for this approach, an additional THz pulse detection module are needed. Furthermore, the signal to noise ratio (SNR) achieved is not very high.

In this chapter, we design a multi-microfluidic-channel metamaterial biosensor (MMCMMB) and apply it for tiny liquid sample detection with THz TDS systems. The device is shown to have a high sensitivity on tiny liquid sample. A better sensing performance can be achieved with the multi-channels concentrating the liquid sample into the field-enhanced areas. We applied the metamaterial introduced in the Chapter 4 with multi-channels for several types of liquid samples. The detections of isopropyl alcohol (IPA) -water mixtures and bovine serum albumin (BSA) solutions based on the proposed MMCMMB are presented.

5.2. Simulation and fabrication

A bow-tie structure unit of MM is shown in Fig. 5.1. The side of bow-tie array MM is 50 μm with a 10- μm -gap between the equilateral triangles pair. The bow-tie structure consists of 100-nm-thick Au on 500- μm -thick quartz substrate. Simulation was performed with the frequency domain solver in the CST Microwave Studio[108]. In the simulation, the quartz substrate was modeled as a lossless dielectric with dielectric permittivity $\epsilon= 4.41$ and the Au conductivity was set as 4.56×10^7 S/m[109], [110]. The incident THz polarization was set as the direction of the arrow in Fig.1(a). **The polarization of the incident THz field was vertical to the long axis of the unit. If the polarization direction is rotated 90 degree, there will be no**

resonance peak. The amplitude transmission $t(\omega)$ was obtained by the following equation $t(\omega) = |\tilde{E}_s(\omega) / \tilde{E}_r(\omega)|$, where $\tilde{E}_s(\omega)$ and $\tilde{E}_r(\omega)$ are sample and reference signals, respectively, ω is the angular frequency. An identical quartz substrate was adopted as the reference.

The simulation results are shown in Fig. 5.1. The resonance peak of designed MM is at 2.06 THz. The enhancement region of electric field is mainly at the center of the bow-tie structure, which is the best sensing area for biomedical applications. Thus, we designed the multi-channels in the center of all the bow-tie structures. There is an inlet and an outlet, which connects all the channels. The schematic diagram of the proposed THz MMCMMB based on bow-tie array MM is shown in Fig.5.2(a).

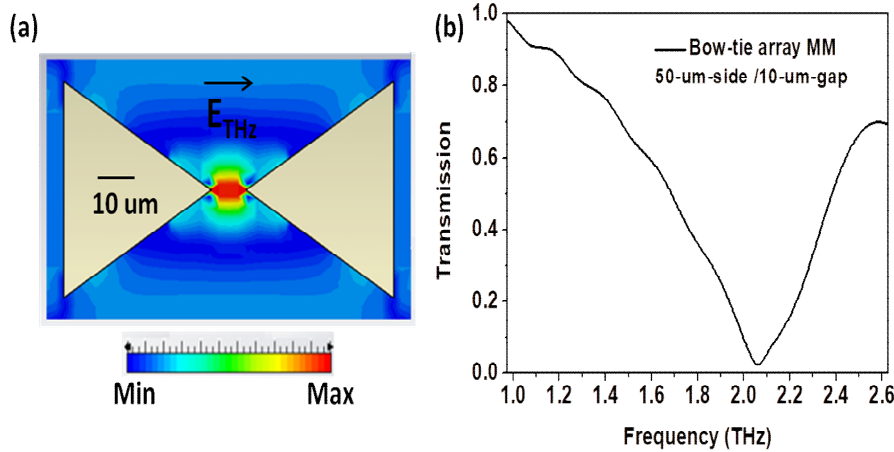


Fig. 5.1 (a) Simulated electric field distribution of the bow-tie array MM at the resonance frequency.
(b) Simulated transmission spectrum of the bare bow-tie array MM.

To test the feasibility of this design, the sensitivity of the multi-channels with different width (15- μm -thickness) was firstly simulated and calculated. The results are shown in Fig. 5.2(b). The channels were set to consist of SU-8 photoresist, which

was set as a lossless dielectric ($\epsilon = 3.24$) in the simulation[103]. The sensitivity is defined as the resonance frequency shift of unit refractive index change for a unit volume sample in the multi-channels[111]. The simulated results show that the larger width of the channel will decrease the sensitivity of designed sensor. The 15- μm -width channels are used in this work by both considering the alignment difficulty during the micro-fabrication and further research on cell detection, which diameter is around 0.2 μm to 10 μm .

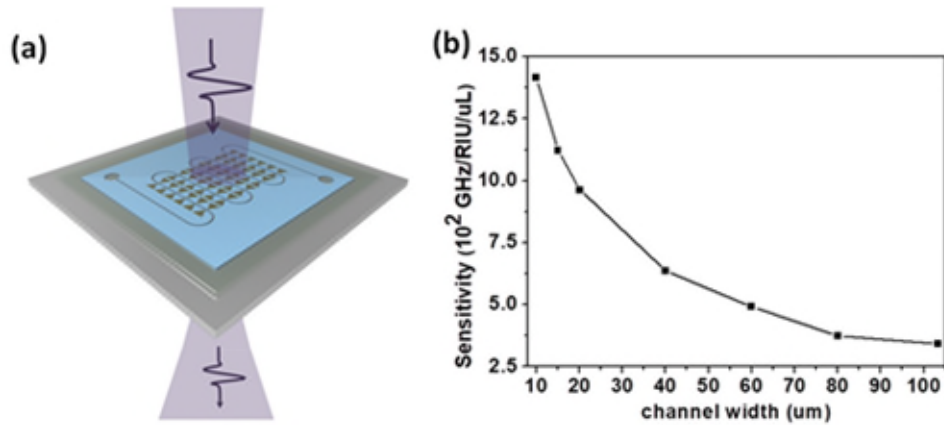


Fig.5.2. (a) Schematic diagram of the multi-channel sensor based on a bow-tie array MM. (b) Simulated sensitivity for different channel width based on a bow-tie array MM.

The fabrication procedures of this proposed device are shown in Fig.5.3. The photolithography process was first applied to build the bow-tie array pattern on the 500- μm -thick z-cut quartz substrate. Later, we performed the lift-off procedure and deposited 20-nm-thick Cr and 100-nm-thick Au with the E-beam evaporation technique to obtain the designed MM device (Fig.5.3(a)). The microfluidic multi-channels with 15/15 μm width/thickness were aligned and patterned on top of each bow-tie gap using SU-8 photoresist (Fig.5.3(b)). The single channel was aligned and

patterned on top of the boundary of the whole bow-tie area using SU-8 photoresist with 15 μm thickness. Another 500- μm -thick quartz was applied to seal the channels thanks to its low absorption in the THz range (Fig.5.3(c)). A 5- μm -thick SU-8 photoresist was spin-coated on the quartz substrate as an adhesion layer (Fig.5.3(d)).

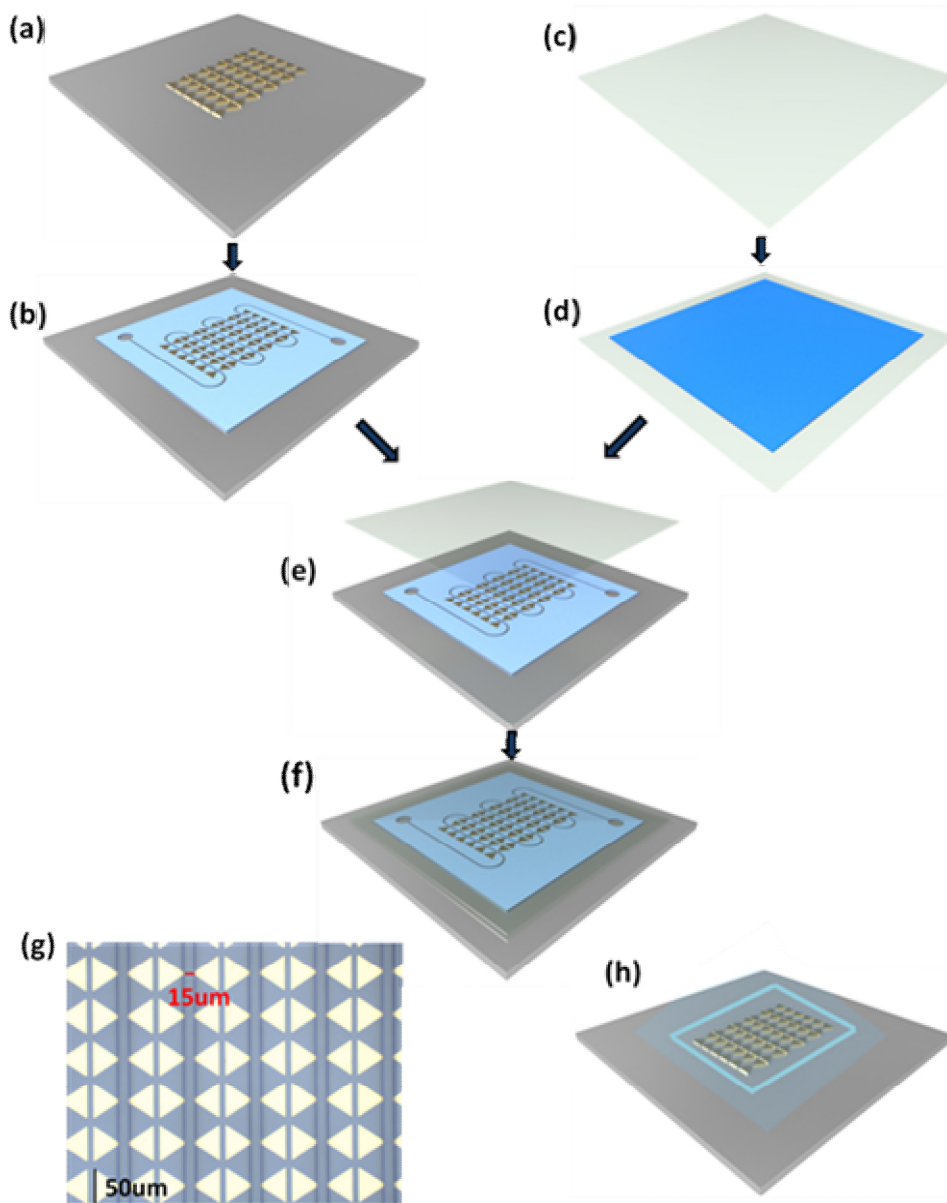


Fig. 5.3. Fabrication procedures of the designed sensor. (a) Bow-tie array MM. (b) Constructed microfluidic multi-channels on the bow-tie array MM. (c) Quartz substrate. (d) 5- μm -thick SU-8

photoresist on the quartz plate. (e) Adhesion of the quartz plate with photoresist to the MM with microfluidic multi-channels. (f) Exposure to the ultraviolet light to make a strong seal. (g) Microscopic image of the fabricated device (15- μm -width multi-channels in the sensitive area of bow-tie array MM). (h) Schematic diagram of the one big channel design based a bow-tie array MM with the same dimension.

Subsequently, the sealing quartz with adhesion layer was mounted on top of one channel and the multi-channels (Fig.5.3(e)). Finally, the fabricated microfluidic MM sensor was exposed to the ultraviolet light to crosslink the adhesive photoresist layer (Fig.5.3(f)), completing the sealing work to avoid liquid leaking during the experiment[103]. The effective region of this device is around 64 mm². The microscopic image of this bio-sensor is shown in Fig.5.3(g), which demonstrate the accurate position of the channels. A bow-tie array MM with one 15- μm -thick channel on top of the whole MM as control. The schematic diagram of the one big channel design is shown in Fig.5.3(h).

5.3. Results

The sensing performances of the designed devices were verified with the transmission THz TDS system. **The sensor was placed in the center of the light path. The polarization of the incident THz field was vertical to the multi-channels. When biosensing was performed, we used a holder to fix the sensor in order to keep the same position every test. Thus, polarization will be the same every test. The amplitude transmission spectra were calculated.** The liquid volume of the sample was recorded. The sensitivity (S) is defined as the resonant frequency shift of unit

refractive index change for unit volume sample[111]. The figure of merit (FOM) is calculated as $FOM=S/FWHM$. FWHM is the full width at half maximum in the amplitude transmission spectra.

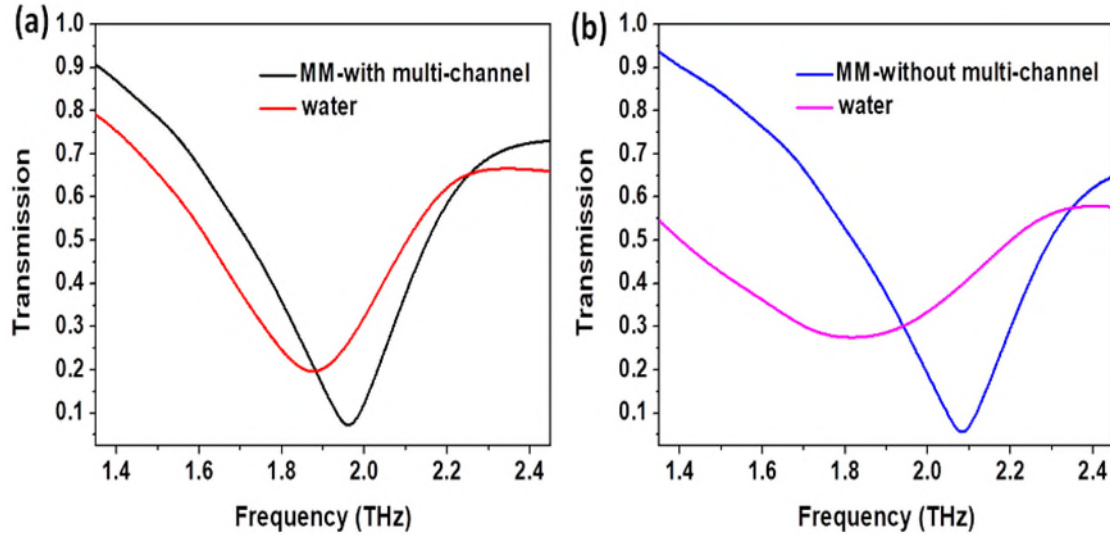


Fig.5.4 (a) Transmission spectra of the MMCMMB (MM with multi-channel, black line), and with water injected into the multi-channels (red line). (b) Transmission spectra of bow-tie array MM with only one big channel on top of the whole MM area (MM without multi-channel, blue line), and with water in the channel (magenta line).

Firstly, water was detected with MMCMMB and the device with one channel to verify the sensing performance of proposed device. The experimental transmission spectra results are shown in Fig. 5.4. The MM with one channel has a resonance frequency at 2.08 THz, while the resonance frequency of the bare MM is 1.96 THz. The transmission spectra after water injection demonstrate that the MMCMMB largely decreases the damping effect to the MM resonance caused by the water absorption [1, 35].

The resonance frequency difference between the two devices is caused by the SU-8 photoresist used to construct the multi-channels. The SU8 photoresist occupies a

part of the surface area of the bow-tie structure, but the constructed microfluidic channel is mainly located in the hotspot area where the metamaterial electric field is enhanced, and the SU8 photoresist is mainly located in the area with slightly enhancement. SU8 photoresist will slightly affect the resonance peak of the metamaterial itself. For example, the resonance peak of the metamaterial without the microfluidic channel is at 2.08 THz, and the resonance peak of the sensor with the microfluidic channel is at 1.96 THz. The red shift of the resonance peak after adding the liquid sample, the sensor containing the microfluidic channel is relatively smaller than the metamaterial without the microfluidic channel. However, it needs to be particularly pointed out that the design containing the microfluidic channel makes the liquid sample mainly located in the hotspot area where the electric field of the metamaterial is enhanced. The sensitivity and quality factor of the sample per unit volume are significantly improved, which greatly reduces the amount of sample, which is expensive and targeted. The biomedical samples are very meaningful

TABLE 5.1

Water sensing comparison results for the bow-tie array MM with and without multi-channel.

	MM WITH MULTI-CHANNEL	MM WITH MULTI-CHANNE
Liquid volume (uL)	0.96	0.13
Frequency shift (GHz)	267	86
Sensitivity (GHz/RIU/uL)	232	552
$S=\Delta f/\Delta n/V$		
FWHM ₁ without water (GHz)	83.7	99.9
FWHM ₂ with water (GHz)	931.8	350.9
Figure of merit (/RIU/uL)	0.25	1.58
$FOM=S/FWHM_2$		

The results of the bow-tie array MM with and without multi-channels are shown in Table 5.1. The MMCMMB only needs a tiny liquid volume and the FWHM after sample loaded is much smaller. Furthermore, the sensitivity per unit volume, especially the figure of merit is much higher for the MMCMMB. The comparison result demonstrates the good sensing performance of the MMCMMB design compared with the device with one big channel.

To further test the effectiveness of the proposed MMCMMB design, the IPA-water solutions were measured. The IPA-water mixtures were tested. We selected the IPA percent of 100%, 75%, 50%, 25% and 0% as samples for this experiment (100%-pure IPA, 0%-pure water). The refractive index and the absorption coefficient of the IPA-water mixture decrease with the increase of the IPA concentration[99], [103]. The IPA-water mixtures were also measured with MM device with one big channel as control. The mean value of three repeated measurements for each concentration was adopted for further analysis.

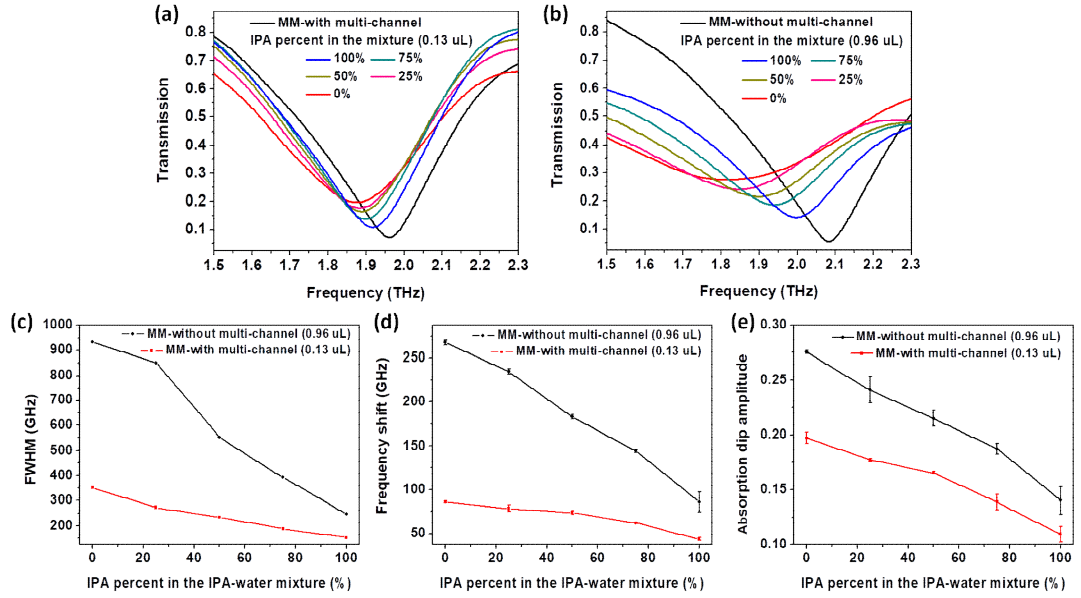


Fig.5.5 Experimental results for the IPA-water mixtures with different IPA concentrations based on the proposed MMCMMB (MM with multi-channel) and the bow-tie array MM with only one big channel on top of the whole MM area (MM without multi-channel). Transmission spectra for the different IPA-water mixtures based on the MM with multichannel (a) and the MM without multichannel (b). (c) FWHM results of the IPA-water mixtures with different IPA concentrations. (d) Average resonance frequency shift results of the IPA-water mixtures with different IPA concentrations. (e) Average absorption dip amplitude results of the IPA-water mixtures with different IPA concentrations.

The measured transmission spectra and the corresponding FWHM, resonance frequency shift and absorption dip amplitude results of the IPA-water mixtures with different IPA percentage are shown in Fig. 5.5. In the two devices, the resonance frequency both blue-shifts with the increase of the IPA percentage in the mixture solutions. The FWHM increases with the decrease of the IPA percentage in the IPA-water mixture and the THz absorption of the mixture increases.

Furthermore, the transmission amplitude at the resonance frequency decreases continuously with the increase of the IPA percent in the IPA-water mixture. Although MMCMMB design has smaller resonance frequency shift, it is significant to highlight that the liquid volume used is much smaller and the sensitivity per unit volume is higher. Moreover, the FWHM of the MMCMMB design after liquid injection is much lower and the corresponding FOM is higher. Thus, high-performance quantitative sensing of water-based solutions can be realized with the MMCMMB assisted THz spectroscopy.

In this experiment, the minimum concentration of the IPA aqueous solution we used is 25%, which can be effectively detected and identified. Regarding the minimum detectable concentration, the frequency shift corresponding to the unit refractive index of the sensor with the multi-channel is 72GHz/RIU, and the frequency shift corresponding to the unit refractive index of the sensor with one channel is 223GHz/RIU, and the smallest detectable IPA concentration depends on the refractive index of the IPA solution and the frequency resolution of the terahertz measurement system, and we will accurately measure it in future studies.

To test the feasibility of the proposed MMCMMB design for biomedical applications, the BSA water solutions were measured. The BSA solutions with the concentration of 0.25, 0.5, 1, 2 mg/mL were measured. Three repeated measurements for each concentration were conducted for further analysis. The measured transmission spectra and the corresponding resonance frequency shift results are shown in Fig. 5.6. The average resonance frequency shift is 98, 101, 110, 118 GHz for 0.25, 0.5, 1, 2 mg/mL BSA solutions. These results fully demonstrate

the feasibility of the proposed MMCMMB design in real liquid-based THz biosensing application.

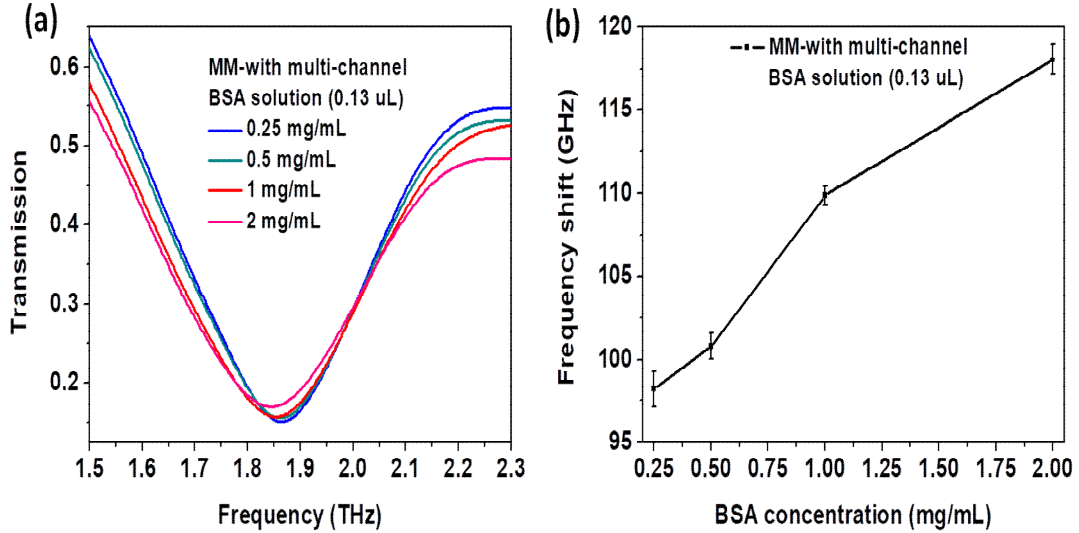


Fig.5.6 Experimental results for the BSA solutions with different BSA concentrations based on the proposed MMCMMB. (a) Transmission spectra for the different BSA solutions based on the MM with multichannel. (b) Average resonance frequency shift results of the BSA solutions with different BSA concentrations.

The experimental results demonstrate the robust feasibility to detect tiny volume liquid samples with high sensitivity with the proposed MMCMMB. Comparing with MM sensor with one microfluidic channel[98]–[105], the proposed MMCMMB can increase the detection sensitivity and need less sample volume. Moreover, the proposed design has a wide scope of applications, as it can be retrospectively adopted in all the standard THz-TDS systems. The sensing procedures are easy. In contrast to the near-field microfluidic MM chips, the detection SNR is large. The MMCMMB can be fabricated on quartz substrates with the standard

microfabrication technique. The cost is also much lower than the near-field microfluidic MM chips which need a high-performance nonlinear optical crystal.

In the previous studies, the sample is normally cover the whole region of the MM and the volume of the sample is large [69]–[71], [78]–[80]. If the required sample volume is not considered, the sensing sensitivity in our study (72 GHz/RIU for the multichannel design, 223 GHz/RIU for the one big channel design) is comparable to previous studies (such as, 40 GHz/RIU, 220 GHz/RIU[105], 305 GHz/RIU[104]). Nevertheless, our fabricated device needs much tiny sample volume, which is highly suitable for the liquid samples that is hard to obtain high volume. The proposed design can be extended to other MM structures and other frequency ranges. The sensitivity and the FOM can be further improved by optimizing the MM structure, such as using a thinner substrate [93], [94] and a resonator with a higher quality factor[92], [111], [115]. Moreover, the overlap of the electromagnetic fields and the sensing analytes can be further improved to achieve higher sensitivity[111]. As for the biosensing applications, the sensitivity and selectivity of the proposed design can be further improved by optimizing the structure parameters to match the resonant frequencies of the detected biological macromolecules and specific reaction between the biological target and binding agent immobilized onto the device[104].

5.4. Summary

In summary, the MMCMMB provides an effective THz-analyte interaction platform for tiny volume liquid sensing, which has the advantages of being highly sensitive, label-free, cost-effective, easy to operate and highly compatible. The proposed design has promising applications in real liquid-based biosensing and could accelerate the development of THz lab-on-chip devices.

6. Oral cancer characterization and imaging

Differentiating cancer tissue from normal tissue with THz light has been investigated for decades[13], [86], especially on breast cancer samples[36]–[39], [116]–[118]. However, few research on the use of THz imaging for oral cancer detection has been reported [41], [42]. In this chapter, we demonstrate how a window-sample-water sandwich structure can significantly enhance the contrast in THz reflection spectroscopy. We image paraffin-embedded oral cancer tissues and show how the proposed method increases the sensitivity of THz measurements for solid low-absorption thin film cancer samples. In addition to this, we also investigate the sample preparation methods for biological tissues, such as porcine skin, muscles and fat, for applications in THz spectroscopy.

6.1 Tissue preparation techniques and THz measurements

The water content in fresh tissue often changes following excision with the potential to be decrease over time. Freeze drying is one of the techniques used to remove water from fresh tissues, but often increases surface roughness and causes the sample to not have an even thickness[116], [119], [120]. This will affect the accuracy of the calculation of the THz parameters. In the work reported by G. Png, only the absorption coefficients of dehydrated samples were presented and the refractive indexes were not given[119]. A recent study by G. G. Hernandez-Cardoso et. al. simulated the THz parameters at of skin at different hydration levels for the application of early screening of diabetic foot syndrome [121]. The dehydrated

sample THz parameters were extracted using histological dehydrated samples from breast biopsy. One of the steps in their processing technique uses ethanol to replace the water from the biopsy sample.

Herein, we propose an improved dehydration protocol based on histological techniques. Our protocol works on various tissue types and the samples prepared are thin, flat slides, which are suitable for THz transmission measurements.

6.2 Improved sample preparation techniques

Figure 6.1 shows the preparation flow chart of our dehydration protocol. Fresh porcine skin, muscle and fat were cut into $1\text{ cm} \times 1.5\text{ cm} \times 4\text{ mm}$ (width \times length \times thickness). First, we need to make sure the sample does not deteriorate over time, so we fixed the sample using 4% para-formaldehyde (PFA) in $4\text{ }^{\circ}\text{C}$ and freeze for 3 days. The para-formaldehyde powder was dissolved in phosphate-buffered saline (PBS) which is considered as isotonic solution for fresh tissue. The fixation lasts for 3 days as the estimated penetration speed of the fixative is approximately 0.5mm per hour.

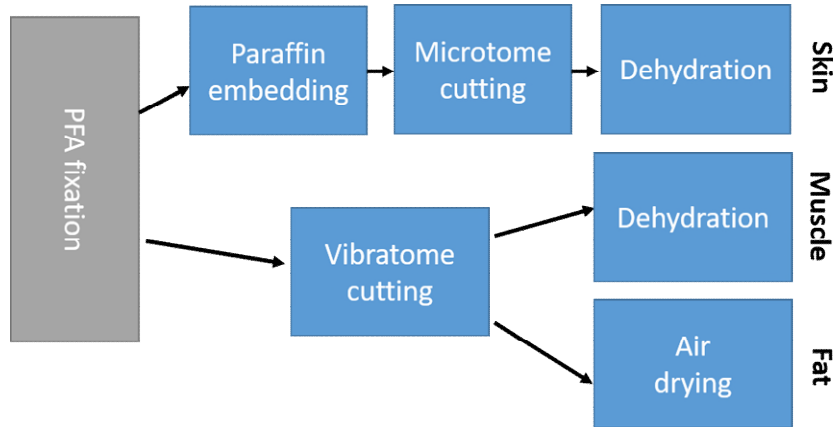


Fig. 6.1. Flow chart of dehydration protocol for porcine skin, muscle and fat tissue.

After PFA fixation, we rinsed the sample with PBS to wash off excessive fixative. Then the sample is ready for sectioning. Tissues with different textures require different sectioning techniques. Muscle and fat tissues are relatively soft and we used a vibratome to slice them. A vibratome works by cutting the sample with a motorized razor blade. The sample is glued to a metal block whose relative position can be adjusted for cutting slices with different thickness. Section thickness may vary between 1 μm to a few hundred micrometers with resolution of 1 μm . The cutting amplitude and speed of the razor blade can also be adjusted. Cold PBS solution was used to soak the sample and improve its rigidity. We also find that well fixed samples are harder in terms of stiffness which facilitates the sectioning. Therefore, fixation is important for the overall preparation technique. Then we can proceed to dehydration. The dehydration process also varies depending on tissue types. For muscles, the majority of tissue mass is water and protein therefore we can replace the water with ethanol. This is done by soaking the muscle sample in a series of ethanol solutions with different concentrations. In our experiment, we used 70%, 85% and 100% with an immersion period of 1 h per concentration. Using a low

to high concentration gradient can protect the sample from distortion caused by water out flux. Then the muscle sample can be dried in ambient air because ethanol is highly volatile. Gentle pressure can be applied to the sample to prevent the sample from curling. At this point the muscle has been dehydrated and it is ready for measurements with the THz system. On the other hand, the major component of fat is lipid and water only plays a minor role in the effective refractive index. In order to accurately measure its THz parameters, it is not suitable to use ethanol to replace the liquid water as the lipid will dissolve in ethanol. The resulting sample would be a hollow cell skeleton without biological content. To dehydrate fat samples, we simply dry them in ambient air for 24 h. Vibratome sectioning and ethanol/air drying dehydration work for muscle/fat tissues.

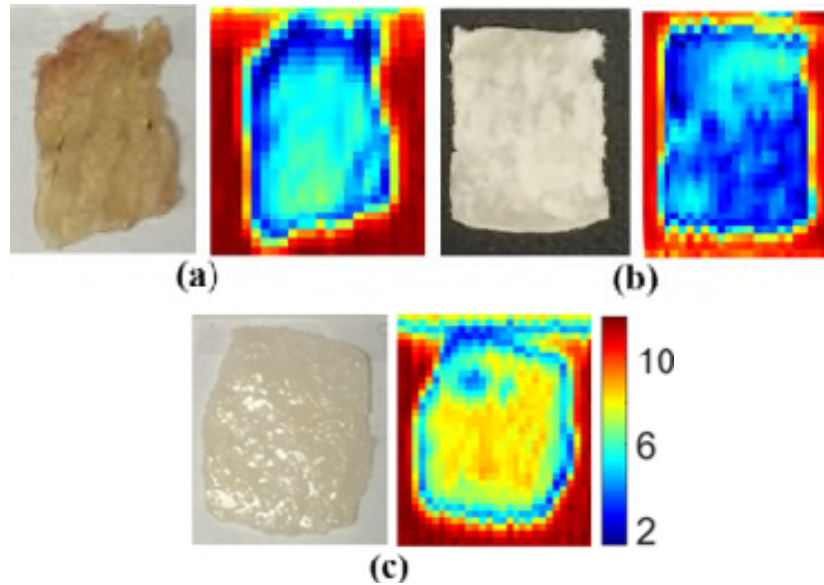


Fig. 6.2. Dehydrated porcine (a) muscle, (b) skin, (c) fat tissues and their corresponding THz Emax images, where Emax is the maximum amplitude of THz time-domain signal.

The resulting sections are shown in Fig.6.2. We can see the sections have an even surface therefore it is ideal for THz transmission measurements. Unfortunately, the

porcine skin samples we used are very tough and the vibratome cannot cut through them. The metal block used to glue the sample tilted over with the skin sample as the razor blade moved forward. Instead of using a vibratome, we use a rotary microtome to section skin tissues. Before sectioning the sample has to be dehydrated and the steps are as previously described. Then the sample was soaked in xylene. The sample has a transparent appearance after this step because paraffin wax is immiscible with water or ethanol, but xylene can dissolve wax. Then we used paraffin wax to infiltrate the sample as it provides physical support for sectioning in the next step. Dehydration, clearing and infiltration was performed using a commercial tissue processor (Thermo Fisher SCIENTIFIC Inc., Excelsior ES). After processing, the paraffin embedded sample was sliced with a microtome. Most of the microtomes can cut samples into sections with thickness from 1 μm to 60 μm , which is suitable for microscope examination. However, the sample is considered a thin film in THz transmission measurements because the multiple reflections from the sample will overlap with one another, resulting an inaccurate parameter extraction if the ordinary calculation technique is used [3]. Generally, samples with $n = 1.5$ will have overlapping reflections if the thickness is under 200 μm . Although one might apply thin film calculations the result is sensitive to a number of factors such as thickness variation and optimization algorithm [4]. In order to obtain a robust result from dehydrated biological sample, we decided to prepare samples thicker than 200 μm . Since most of biological samples have a refractive index greater than 1.5, we will be able to separate multiple reflections from the main pulse easily. Using a simple calculation method based on Beer Lambert's law we can work out the sample THz parameters and the result will be less sensitive to errors in the thickness. To obtain skin slides with a thickness of over 200 μm , we use the rotary

microtome to trim the sample from both sides of the skin. The remaining part of the skin was used for THz measurement. The trimming may require multiple embedding steps to re-orientate the sample, depending to the microtome and tissue cassette used. Now the sample slide is embedded in wax which will also contribute to the effective refractive index if we measure it directly. We need to remove the effect of paraffin, so we dissolve the wax with xylene and rinse the sample by ethanol. If there is any unevenness on the sample surface, we can polish it with a file.

6.3 THz Measurements of Dehydrated Porcine samples

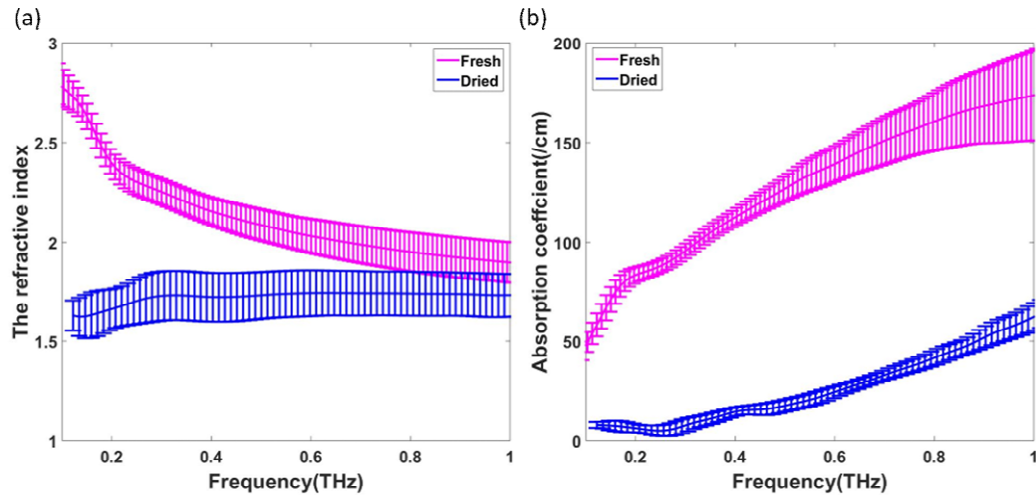


Fig. 6.3. The average refractive index (a) and absorption coefficient (b) of dehydrated porcine skin.

All dehydrated samples were measured with the transmission system. In total, we have 9 samples for each type of tissue. Figure 6.3 and Figure 6.4 show the average refractive index and absorption coefficient of skin and muscle respectively. Blue lines indicate the fresh sample while the red lines represent the dehydrated

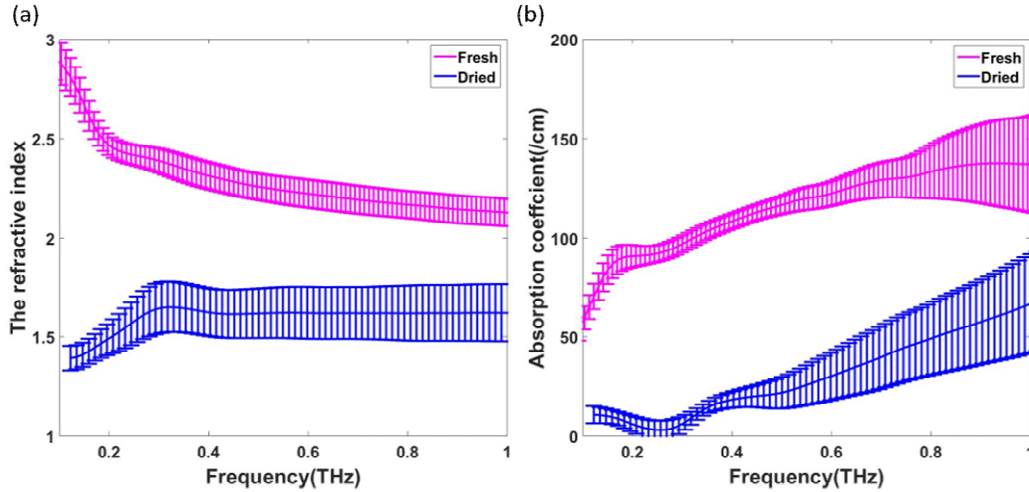


Fig. 6.4. The average refractive index (a) and absorption coefficient (b) of dehydrated porcine muscle.

sample. The error bars represent the standard deviation. First, let's look at the refractive index of the dehydrated samples, the three types of tissues show no significant difference between them after dehydration as the average is in the range of 1.6-1.7. As for the absorption coefficient, muscle and skin samples belong to a group with greater absorption. Whereas fat sample is only 15/cm at the same frequency. Low absorption is a distinct feature of fat sample which differentiates it from the other two samples. Additionally, it is worth noting that muscle samples have the greatest standard deviation which indicates that the sample is highly inhomogeneous. On the other hand, the fat samples are relatively homogeneous therefore have smaller error bars.

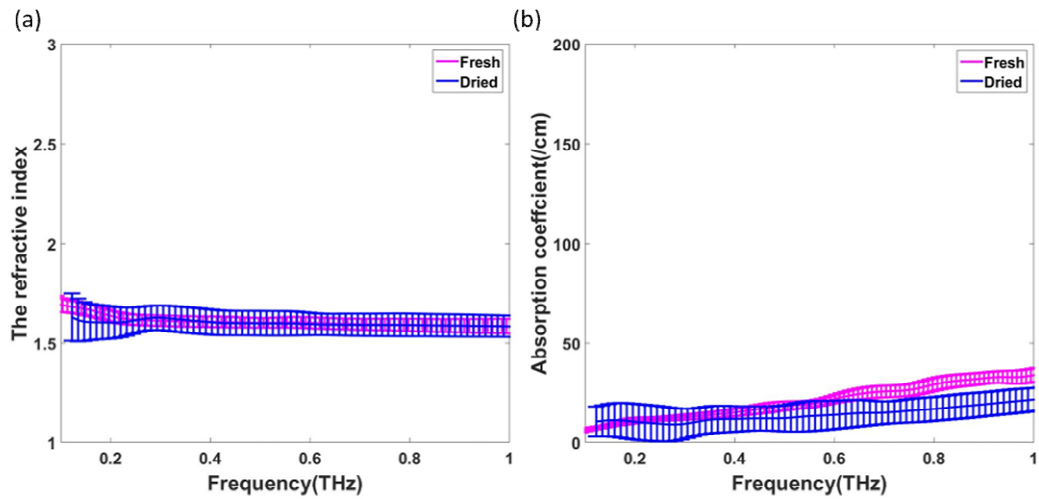


Fig. 6.5. The average refractive index (a) and absorption coefficient (b) of dehydrated porcine fat.

6.4 Ex vivo THz Detection of Oral Cancer Tissues

Oral cancer is one of the most common invasive epithelial malignant tumors of the head and neck. Typically, it occurs in the tongue, cheek, gums, bottom of the mouth and other superficial parts. Although new treatment methods are emerging constantly, its 5-year survival rate has not been significantly improved in recent decades, making it a serious threat to human health. Although oral cancer is located in the superficial region of the oral cavity, nearly half of the cases are diagnosed with regional lymph node metastasis[122], [123]. The main reason leading to this phenomenon is the difficulty to distinguish cancer from benign diseases precisely and conveniently, especially for cancer in the early stages. At present, the clinical diagnosis depends mainly on the clinical experience and CT imaging.

Pathological examination is the gold standard for cancer diagnosis. This technique involves the microscopic examination of cancer tissues excised from the patient by a pathologist. However, this examination relies heavily on biopsy or surgery

excision, which are invasive and painful for patients. Therefore, there is a pressing need to find a more comprehensive diagnosis process than conventional pathological examination and establish a sensitive, fast, convenient and feasible examination method to identify oral cancer.

THz imaging is a promising technique which has attracted interest in the research of cancer diagnosis. Compared with CT, MR and histological examination, THz imaging possesses many unique features which are favorable for cancer diagnosis. It is a high contrast, time-saving and noninvasive technique with non-ionizing radiation. As described in Chapter 1, THz imaging has been utilized to examine fresh excised oral cancer tissue. However, using fresh tissue cannot eliminate the influence of inter individual water content. Among healthy oral tissues, there are a lot of minor glands, such as lip glands, palate glands and bubble glands, which contain continually changing volumes of water. This makes it unreliable for distinguishing oral cancer from the surrounding tissues with THz imaging of fresh excised samples. Thus, measuring the dehydrated paraffin embedded oral cancer is a better way to precisely detect oral cancer.

6.4.1. Thin film oral cancer imaging with terahertz

As tissue sections with thicknesses ranging from 1 μm to 60 μm can be easily obtained using a microtome, we chose 30 μm as an appropriate thickness at the beginning of our research considering the THz resolution range. Two paraffin embedded samples with the thickness of 30 μm were prepared for THz measurements with the help of pathological technicians. The prepared samples are shown in Fig 6. Then we mounted the thin film cancer tissues onto the quartz and normal glass substrate. The mounted thin film cancer tissue slices were measured with the homemade THz TDS transmission system.

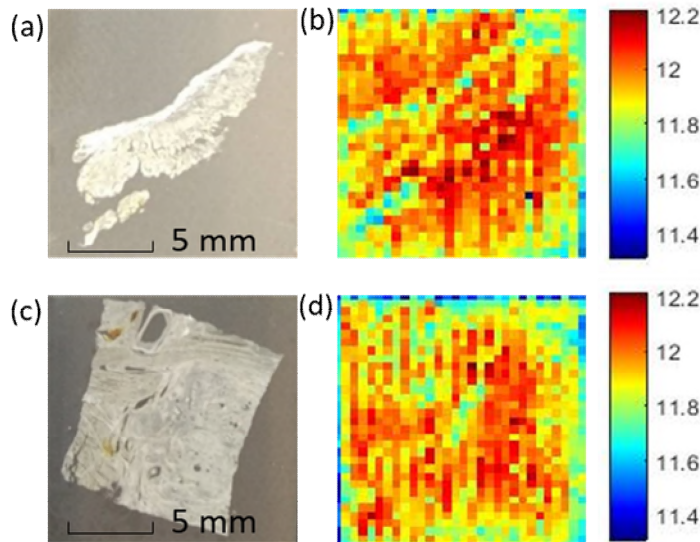


Fig. 6.6. Optical image (a) and THz E_{max} image (b) of normal oral tissue; optical image (c) and THz E_{max} image (d) of oral cancer tissue.

After processing the data, we found that the absorption of the normal glass slide was very high. On the contrary, the absorption of the sample on the quartz substrate is less than 5%. Very little information of the tissues can be obtained from these

samples. From the tissues on the quartz substrate, contrast was observed neither between the normal tissues and the cancer tissues, nor between the tissue slice and the quartz. Optical parameters cannot be calculated accurately due to the low contrast. The refractive index was calculated to be range from 1.2 to 1.3, which is much lower than the dehydrated bio-sample range measured in Chapter 2 and the value in previous reports. Therefore, thicker samples, which may absorb THz radiation more strongly and give improved contrast, were prepared in the following experiment.

6.4.2. Imaging and spectroscopy of thick oral cancer samples

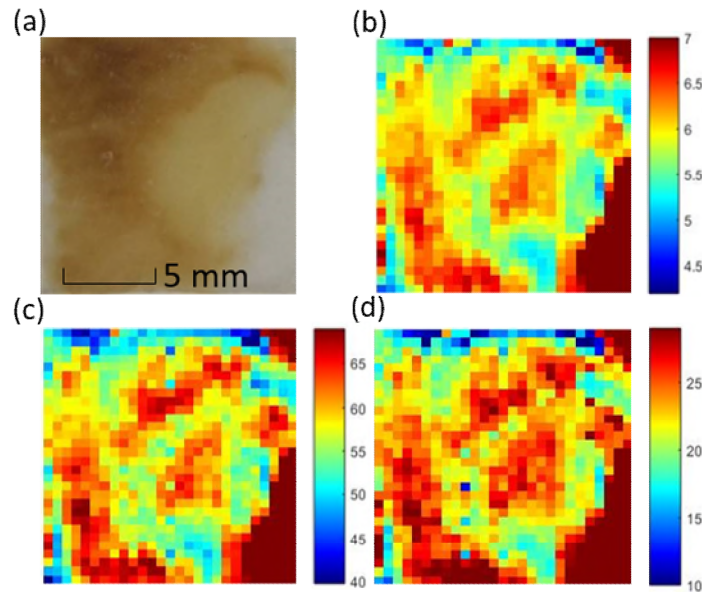


Fig. 6.7. (a)Optical image, (b)THz E_{\max} image and FD-magnitude image at 1 THz(c), 1.5 THz(d) of 30 μm oral cancer samples.

Because of the low absorption of thin films with a thickness on tens of micron-scale provided insufficient contrast between different kinds of tissues, thick samples were prepared to achieve a better contrast. The improved preparation method for

dehydrated skin samples were used in this experiment. First, the paraffin embedded oral cancer tissues was sectioned to obtain a flat surface. Then, the sample was put into paraffin solution at 60 °C. After all the paraffin around the bio-sample had melted, we re-embedded the sample and sectioned it with the paraffin from the other side. At last, the paraffin section was polished to obtain the sample with a target thickness. The sample was detected and imaged with homemade THz transmission system as described in Chapter 2. Figure 6.7 shows the optical image, THz time domain Emax image and THz frequency domain magnitude image at 1 and 1.5 THz of the 600 μm oral cancer tissue. In order to obtain a clearer image, the range of the colour bar was set as the range between the lowest and highest values of the tissue sample. This provides the best contrast to the tissue area. Compared with thin film THz images, images of the thicker samples possess higher contrast between normal tissue and cancer tissue. There is a distinct boundary between the normal tissue and the cancer tissue in both time domain and frequency domain images.

6.4.3. THz parameters of thick oral cancer tissues

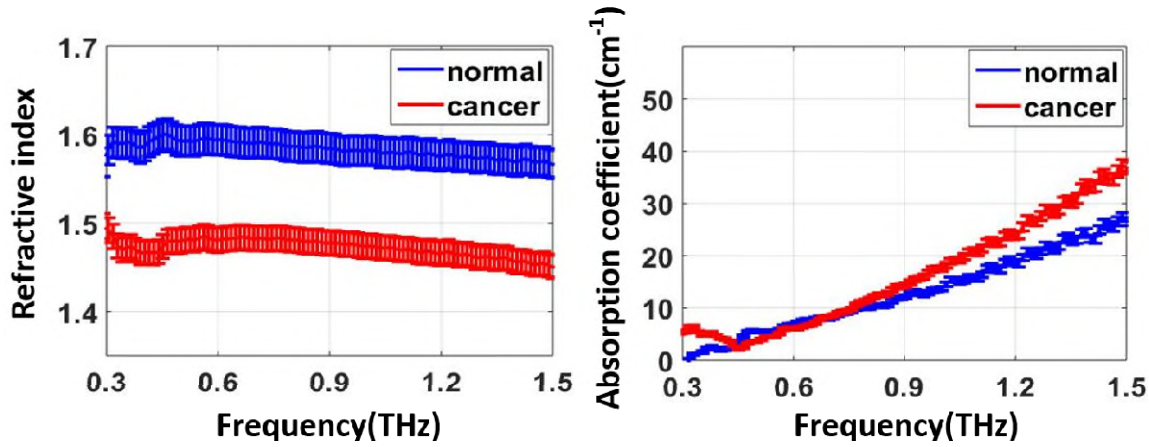


Fig. 6.8. The average refractive index and absorption coefficient of 600 um oral cancer tissue.

The refractive index and absorption coefficient were calculated with the calculation method introduced in Chapter 2. As shown in Figure 6.8, the refractive index of normal tissue is slightly higher than that of the cancer tissue, while the absorption coefficient of the cancer tissue is slightly higher than that of the normal tissue.

6.4.4. Sandwich structure reflection geometry

To evaluate the sensitivity on low-absorptive solid samples, such as paraffin-embedded tissue, we assume the refractive indices of the cancer and normal tissue are $n_c = 1.63 - 0.05i$ and $n_n = 1.56 - 0.03i$. We consider using water as the top medium in the sandwich geometry to give better contact with the tissue. The percentage change of $abs(M)$ by the cancer tissue was compared to that by the normal tissue, calculated by Eqn:

$$RC_{abs(M)} = \frac{abs(M) - abs(M_{V\%=0})}{abs(M_{V\%=0})} \times 100\%$$

Fig. 6.9 shows that the quartz window-sample-water setup can display the highest contrast between the normal and cancer tissue. In contrast, the transmission geometry only has less than 2% difference. Thus, we will show THz imaging results of oral cancer from sandwich reflection spectroscopy based on the window setup.

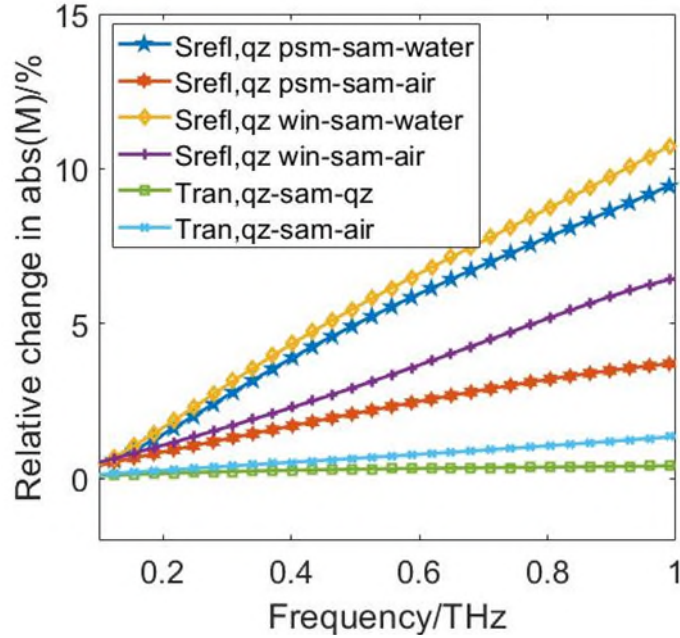


Fig. 6.9 Percentage change of the amplitude of M by the cancer tissue compared to the normal tissue, assuming sample thickness $d_{\text{sam}}=30\mu\text{m}$, $\theta_{\text{air}}=30^\circ$, both the window and the prism are made of quartz.

The THz images of a paraffin-embedded oral cancer sample from transmission and sandwich reflection geometries are given in Fig 6.10, as well as the visual and histology images. The normalized amplitude of M was calculated by Eqn

$$\left\{ \begin{array}{l} M_{\text{mag}} = \left| \frac{\text{FFT}(E_{\text{sample}}(t) \times \text{WinFtn})}{\text{FFT}(E_{\text{ref}}(t) \times \text{WinFtn})} \right| \\ M_{\text{mag_plot}} = \frac{M_{\text{mag}}}{\max(M_{\text{mag}})} \end{array} \right.$$

and plotted in Fig 6.10 (d-g). The transmission images

(Figure 6.10 (d-e)) are slightly blurred because of the low contrast: at 1 THz the

absolute value of M_{mag} of the transmission image before normalization only varies between 0.94 and 1.06, this narrow dynamic range makes it difficult to discriminate between the cancer and normal tissues. However, using our proposed sandwich technique in reflection geometry, the dynamic range is significantly increased and the shape of the tissue in the THz reflection image at 0.5 THz (Fig 6.10 (f)) corresponds well with the dried tissue in Fig 6.10 (b), the black dashed circle area may indicate cancer as it is very distinct from the surrounding areas. To further check this, the histology image is given in Fig 6.10 (c). The cancer area is indicated by the black dashed line and matches very well with the THz image at 1 THz (Fig 6.10 (f)). The color bars in Fig 6.10 (d-g) are the normalized amplitude of the processed waveforms as calculated by Eqn above. From the ranges of the color bars, it is clear that the percentage changes in amplitude for Fig 1f and Fig 1g are much greater than for Fig 6.10 (d) and Fig 6.10 (e). From Eqn

$$RC_{\text{abs}(M)} = \frac{\text{abs}(M) - \text{abs}(M_{V\%=0})}{\text{abs}(M_{V\%=0})} \times 100\%$$

, we calculated that the contrast between the cancer and normal tissues was enhanced by over a factor of 5, by using the proposed multilayer reflection geometry compared to transmission geometry. To check if the high contrast in the reflection images was caused by the different water diffusion speeds going into the normal and cancer tissues, we imaged the tissue in reflection geometry repeatedly for 7 times within 2 hours interaction with water. However, no clear difference was observed.

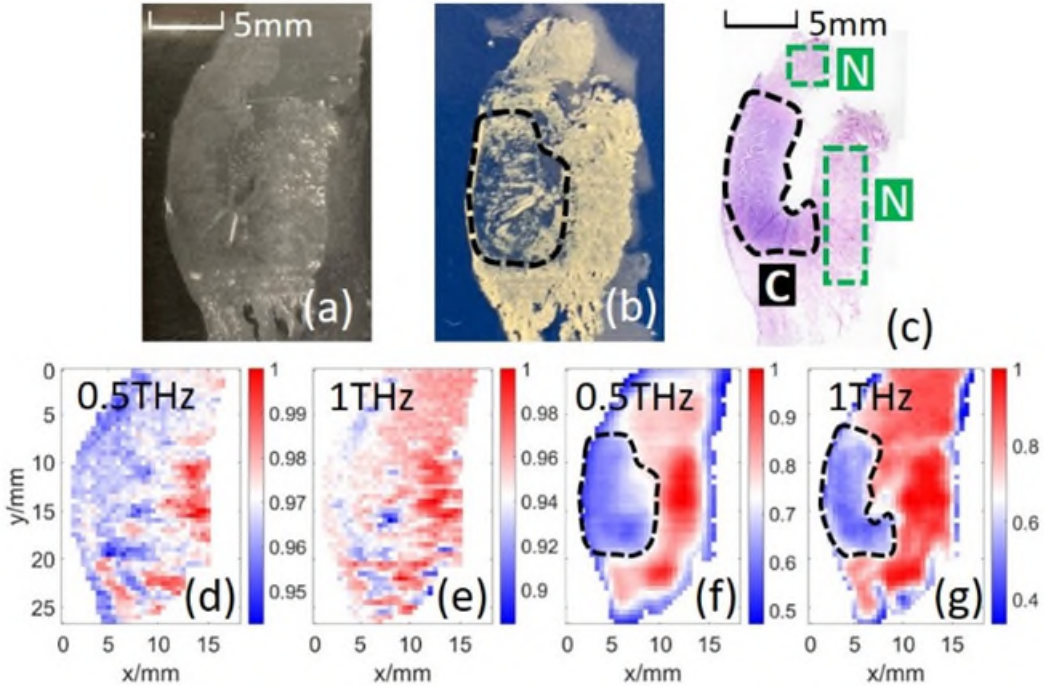


Fig. 6.10. Photographs of the paraffin-embedded oral cancer tissue (a) during the THz measurement, and (b) after drying, (c) histology image, the cancer area is marked with black dashed curve and the normal areas are marked with green dashed curves. (d-e) THz transmission spectroscopy images at 0.5 THz and 1 THz. (f-g) THz sandwich reflection spectroscopy images at 0.5 THz and 1 THz. The upper limit of the colormap scales of the THz images were all normalized to 1.

The photograph, histological image and THz images of a paraffin-embedded oral cancer sample from transmission and sandwich reflection geometries are shown in Fig. 6.9. The normalized data were acquired with Equation (1) and plotted in Fig. 6.9(c-d). At 0.6 THz, the range of unnormalized values of the transmission image only vary between 0.96 and 1.04, which makes it impossible to tell the cancer from normal tissue. With the quartz-window-water sandwich reflection geometry, a 5-fold increase in contrast was obtained compared with the transmission geometry. The THz reflection image of the cancer tissue in Fig. 6.9(d) matched well with the histological image.

6.5 Summary

In this chapter, we first introduced the tissue sample preparation method, especially the vibratome for preparation of 60- μm -thick to 200- μm -thick fat and muscle tissue in terahertz imaging research. In particular, we showed the measurement of porcine skin, muscles and fat tissues to investigate the properties of fresh and dehydrated tissues using THz-TDS. We also image the human paraffin embedded oral cancer tissue from OSCC patients with the THz transmission system. Due to the limited sensitivity and contrast, we further propose a new reflection imaging strategy based on an index matching sandwich structure. The imaging results of paraffin embedded oral cancer tissue show a significantly higher contrast using the proposed sandwich structure compared to that with normal transmission and reflection geometries. This technique offers a highly sensitive approach for THz biomedical research and applications.

7. Conclusions and key findings

In this thesis we present devices and imaging strategies for improving the sensing, characterizing and diagnosing abilities of THz spectroscopy and imaging. Chapters 1-3 introduce the fundamental background of cancer detection techniques, THz equipment and systems, as well as the relevant data processing methods used in the thesis. Chapters 4 to 5 detailed the detection of biomolecules and liquid samples by the proposed metamaterial devices. Chapter 6 presents the tissue preparation methods, tissue characterization and oral cancer sample THz imaging.

In Chapter 4, we designed and fabricated a bow-tie terahertz metamaterial biosensor and enhance the sensing ability of the sensor with GNPs of a diameter of 5nm, 15nm and 25nm respectively. We detected the binding state of EGFR with its specific antibody at different concentrations with the biosensor. The resonance frequency shifts of GNP and GNP-Ab were observed. We showed the enhancement ability of GNPs on the sensing performance of the THz metamaterial biosensor. We found that the frequency shift of EGFR either with or without GNP increases with increasing concentration. A higher sensitivity can be obtained with the assistant of GNPs compared with specific antibody only. The presented results demonstrate that the GNP-assisted metamaterial can be efficiently applied in quantitative EGFR detection with a promising sensitivity. The proposed strategy has great potential for rapid diagnosis of EGFR related diseases.

In Chapter 5, we presented a novel multi-microfluidic-channel metamaterial biosensor (MMCMMB) for highly sensitive THz sensing of small-volume liquid samples. The MMCMMB provides an efficient THz-analyte interaction platform for

small volume liquid sensing, which has the advantages of being highly sensitive, label-free, cost-effective, easy to operate and highly compatible. The proposed design has promising applications in practical liquid-based biosensing, and it could accelerate the development of THz lab-on-chip devices.

In Chapter 6, we presented a method to prepare thin and flat dehydrated samples, which can be easily handled and measured in a transmission setup. Fundamental parameters for modelling THz-tissue interactions are provided as well. Paraffin embedded oral cancer tissues are imaged and characterized. A thin film sandwich structure was used in the terahertz reflection system to improve the sensitivity and imaging contrast. THz images of oral cancer tissues obtained from transmission and the proposed sandwich reflection geometries were conducted and compared: a significantly higher imaging contrast was achieved using the proposed geometry, providing a significantly clearer outline of cancer areas. This work paves the way for terahertz spectroscopy and imaging to practical clinical application.

Key results:

1. Design and fabrication of a THz biosensor for protein measurement using a bow-tie structure metamaterial (Chapter 4). EGFR, a common cancer biomarker of head and neck tumor, was measured to demonstrate the high sensitivity of the biosensor.
2. Development of a novel multi-microfluidic-channel metamaterial biosensor for highly sensitive THz sensing of small-volume liquid samples (Chapter 5). In the future, this biosensor has the potential for sensing single living cells and multiple types of cancer related antigens.

3. Development of a robust dehydrated tissue preparation method for THz measurement (Chapter 6). Different types of tissues were treated so as to have a proper dehydrated state and good shape for THz detection.

4. Development of a novel multi-layer geometry imaging strategy (Chapter 6) which, when applied to THz cancer imaging, increased the imaging contrast five-fold compared with ordinary thin film tissue THz imaging.

Bibliography

- [1] X. Han, S. Yan, Z. Zang, D. Wei, H.-L. Cui, and C. Du, “Label-free protein detection using terahertz time-domain spectroscopy,” *Biomed. Opt. Express*, vol. 9, no. 3, pp. 994–1005, 2018.
- [2] M. O. AlNabooda, R. M. Shubair, N. R. Rishani, and G. Aldabbagh, “Terahertz spectroscopy and imaging for the detection and identification of illicit drugs,” in *2017 Sensors networks smart and emerging technologies (SENSET)*, 2017, pp. 1–4.
- [3] M. S. Islam, J. Sultana, A. Dinovitser, K. Ahmed, B. W.-H. Ng, and D. Abbott, “Sensing of toxic chemicals using polarized photonic crystal fiber in the terahertz regime,” *Opt. Commun.*, vol. 426, pp. 341–347, 2018.
- [4] G. G. Hernandez-Cardoso *et al.*, “Terahertz imaging for early screening of diabetic foot syndrome: A proof of concept,” *Sci. Rep.*, vol. 7, pp. 1–9, 2017, doi: 10.1038/srep42124.
- [5] V. P. Sirkeli, O. Yilmazoglu, S. Preu, F. Küppers, and H. L. Hartnagel, “Proposal for a Monolithic Broadband Terahertz Quantum Cascade Laser Array Tailored to Detection of Explosive Materials,” *Sens. Lett.*, vol. 16, no. 1, pp. 1–7, 2018.
- [6] N. Palka, M. Szala, and E. Czerwinska, “Characterization of prospective explosive materials using terahertz time-domain spectroscopy,” *Appl. Opt.*, vol. 55, no. 17, pp. 4575–4583, 2016.

- [7] H. Vettikalladi, W. T. Sethi, A. F. Bin Abas, W. Ko, M. A. Alkanhal, and M. Himdi, "Sub-THz antenna for high-speed wireless communication systems," *Int. J. Antennas Propag.*, vol. 2019, 2019.
- [8] Q. Sun *et al.*, "In vivo estimation of water diffusivity in occluded human skin using terahertz reflection spectroscopy," *J. Biophotonics*, vol. 12, no. 2, p. e201800145, 2019.
- [9] J. Wang, Q. Sun, R. I. Stantchev, T.-W. Chiu, A. T. Ahuja, and E. Pickwell-MacPherson, "In vivo terahertz imaging to evaluate scar treatment strategies: silicone gel sheeting," *Biomed. Opt. Express*, vol. 10, no. 7, pp. 3584–3590, 2019.
- [10] N. S. Balbekin *et al.*, "Terahertz pulse time-domain holography method for phase imaging of breast tissue," in *Quantitative Phase Imaging V*, 2019, vol. 10887, p. 108870G.
- [11] R. Grigorev *et al.*, "Investigation of fresh gastric normal and cancer tissues using terahertz time-domain spectroscopy," *Materials (Basel)*, vol. 13, no. 1, p. 85, 2020.
- [12] S. S. Dhillon *et al.*, "The 2017 terahertz science and technology roadmap," *J. Phys. D. Appl. Phys.*, vol. 50, no. 4, 2017, doi: 10.1088/1361-6463/50/4/043001.
- [13] C. Yu, S. Fan, Y. Sun, and E. Pickwell-Macpherson, "The potential of terahertz imaging for cancer diagnosis: A review of investigations to date.," *Quant. Imaging Med. Surg.*, vol. 2, no. 1, pp. 33–45, 2012, doi: 10.3978/j.issn.2223-4292.2012.01.04.

-
- [14] Y. Komohara, Y. Fujiwara, K. Ohnishi, and M. Takeya, "Tumor-associated macrophages: Potential therapeutic targets for anti-cancer therapy," *Adv. Drug Deliv. Rev.*, vol. 99, pp. 180–185, 2016.
- [15] P. Pathria, T. L. Louis, and J. A. Varner, "Targeting tumor-associated macrophages in cancer," *Trends Immunol.*, vol. 40, no. 4, pp. 310–327, 2019.
- [16] T. Globus, D. Theodorescu, H. Frierson, T. Khromova, and D. Woolard, "Terahertz spectroscopic characterization of cancer cells," in *Advanced Biomedical and Clinical Diagnostic Systems III*, 2005, vol. 5692, pp. 233–240.
- [17] M. Danciu *et al.*, "Terahertz spectroscopy and imaging: a cutting-edge method for diagnosing digestive cancers," *Materials (Basel)*, vol. 12, no. 9, p. 1519, 2019.
- [18] D. K. George and A. G. Markelz, "Terahertz spectroscopy of liquids and biomolecules," in *Terahertz spectroscopy and imaging*, Springer, 2012, pp. 229–250.
- [19] D. F. Plusquellic, K. Siegrist, E. J. Heilweil, and O. Esenturk, "Applications of terahertz spectroscopy in biosystems," *ChemPhysChem*, vol. 8, no. 17, pp. 2412–2431, 2007.
- [20] A. G. Markelz, A. Roitberg, and E. J. Heilweil, "Pulsed terahertz spectroscopy of DNA, bovine serum albumin and collagen between 0.1 and 2.0 THz," *Chem. Phys. Lett.*, vol. 320, no. 1–2, pp. 42–48, 2000.

- [21] M. Li *et al.*, “Label-free detection of anti-estrogen receptor alpha and its binding with estrogen receptor peptide alpha by terahertz spectroscopy,” *Rsc Adv.*, vol. 7, no. 39, pp. 24338–24344, 2017.
- [22] C. L. Holloway, E. F. Kuester, J. A. Gordon, J. O’Hara, J. Booth, and D. R. Smith, “An overview of the theory and applications of metasurfaces: The two-dimensional equivalents of metamaterials,” *IEEE Antennas Propag. Mag.*, vol. 54, no. 2, pp. 10–35, 2012.
- [23] S. J. Park *et al.*, “Detection of microorganisms using terahertz metamaterials,” *Sci. Rep.*, vol. 4, p. 4988, 2014.
- [24] A. Keshavarz and Z. Vafapour, “Water-based terahertz metamaterial for skin cancer detection application,” *IEEE Sens. J.*, vol. 19, no. 4, pp. 1519–1524, 2018.
- [25] D. Cheng *et al.*, “Terahertz biosensing metamaterial absorber for virus detection based on spoof surface plasmon polaritons,” *Int. J. RF Microw. Comput. Eng.*, vol. 28, no. 7, p. e21448, 2018.
- [26] D.-K. Lee *et al.*, “Nano metamaterials for ultrasensitive Terahertz biosensing,” *Sci. Rep.*, vol. 7, no. 1, pp. 1–6, 2017.
- [27] W. Xu *et al.*, “Gold nanoparticle-based terahertz metamaterial sensors: mechanisms and applications,” *Acs Photonics*, vol. 3, no. 12, pp. 2308–2314, 2016.

-
- [28] A. Ahmadvand *et al.*, “Extreme sensitive metasensor for targeted biomarkers identification using colloidal nanoparticles-integrated plasmonic unit cells,” *Biomed. Opt. Express*, vol. 9, no. 2, pp. 373–386, 2018.
- [29] C. Zhang *et al.*, “Label-free measurements on cell apoptosis using a terahertz metamaterial-based biosensor,” *Appl. Phys. Lett.*, vol. 108, no. 24, p. 241105, 2016.
- [30] M. Yang *et al.*, “Electromagnetically induced transparency-like metamaterials for detection of lung cancer cells,” *Opt. Express*, vol. 27, no. 14, pp. 19520–19529, 2019.
- [31] R. M. Woodward *et al.*, “Terahertz pulse imaging of ex vivo basal cell carcinoma,” *J. Invest. Dermatol.*, vol. 120, no. 1, pp. 72–78, 2003.
- [32] V. P. Wallace *et al.*, “Terahertz pulsed imaging of basal cell carcinoma ex vivo and in vivo,” *Br. J. Dermatol.*, vol. 151, no. 2, pp. 424–432, 2004.
- [33] E. Pickwell *et al.*, “Simulating the response of terahertz radiation to basal cell carcinoma using ex vivo spectroscopy measurements,” *J. Biomed. Opt.*, vol. 10, no. 6, p. 64021, 2005.
- [34] V. P. Wallace *et al.*, “Terahertz pulsed spectroscopy of human basal cell carcinoma,” *Appl. Spectrosc.*, vol. 60, no. 10, pp. 1127–1133, 2006.
- [35] A. J. Fitzgerald *et al.*, “Terahertz pulsed imaging of human breast tumors,” *Radiology*, vol. 239, no. 2, pp. 533–540, 2006.
- [36] T. Bowman, M. El-Shenawee, and L. Campbell, “Time of flight estimation for breast cancer margin thickness using embedded tumors,” *Opt. Interact.*

- with Tissue Cells XXVII*, vol. 9706, p. 97061V, 2016, doi: 10.1117/12.2211167.
- [37] T. Bowman, Y. Wu, J. Gauch, L. K. Campbell, and M. El-Shenawee, “Terahertz Imaging of Three-Dimensional Dehydrated Breast Cancer Tumors,” *J. Infrared, Millimeter, Terahertz Waves*, vol. 38, no. 6, pp. 766–786, 2017, doi: 10.1007/s10762-017-0377-y.
- [38] T. Bowman, M. El-Shenawee, and L. K. Campbell, “Terahertz transmission vs reflection imaging and model-based characterization for excised breast carcinomas,” *Biomed. Opt. Express*, vol. 7, no. 9, p. 3756, 2016, doi: 10.1364/boe.7.003756.
- [39] T. C. Bowman, M. El-Shenawee, and L. K. Campbell, “Terahertz Imaging of Excised Breast Tumor Tissue on Paraffin Sections,” *IEEE Trans. Antennas Propag.*, vol. 63, no. 5, pp. 2088–2097, 2015, doi: 10.1109/TAP.2015.2406893.
- [40] F. Wahaia *et al.*, “Terahertz absorption and reflection imaging of carcinoma-affected colon tissues embedded in paraffin,” *J. Mol. Struct.*, vol. 1107, pp. 214–219, 2016, doi: 10.1016/j.molstruc.2015.11.048.
- [41] Y. C. Sim, J. Y. Park, K.-M. Ahn, C. Park, and J.-H. Son, “Terahertz imaging of excised oral cancer at frozen temperature,” *Biomed. Opt. Express*, vol. 4, no. 8, p. 1413, 2013, doi: 10.1364/boe.4.001413.
- [42] Y. C. Sim, K. M. Ahn, J. Y. Park, C. S. Park, and J. H. Son, “Temperature-dependent terahertz imaging of excised oral malignant melanoma,” *IEEE Trans. Terahertz Sci. Technol.*, vol. 3, no. 4, pp. 368–373, 2013, doi: 10.1109/TTHZ.2013.2267415.

-
- [43] B. D. Sites *et al.*, “Artifacts and pitfall errors associated with ultrasound-guided regional anesthesia: Part I: Understanding the basic principles of ultrasound physics and machine operations,” *Reg. Anesth. Pain Med.*, vol. 32, no. 5, pp. 412–418, 2007.
- [44] R. Guo, G. Lu, B. Qin, and B. Fei, “Ultrasound imaging technologies for breast cancer detection and management: a review,” *Ultrasound Med. Biol.*, vol. 44, no. 1, pp. 37–70, 2018.
- [45] Y.-H. Hsiao, S.-J. Kuo, H.-D. Tsai, M.-C. Chou, and G.-P. Yeh, “Clinical application of high-intensity focused ultrasound in cancer therapy,” *J. cancer*, vol. 7, no. 3, p. 225, 2016.
- [46] A. Momose, T. Takeda, Y. Itai, and K. Hirano, “Phase-contrast X-ray computed tomography for observing biological soft tissues,” *Nat. Med.*, vol. 2, no. 4, pp. 473–475, 1996.
- [47] W. Otieno, H. Nyawanda, and Z. Akanga, “Comparative radio-opacity of bones of commonly consumed fish species in western Kenya region on digitalised lateral neck X-ray films,” *East Afr. Med. J.*, vol. 93, no. 7, pp. 281–286, 2016.
- [48] P. M. Tovar and M. M. R. Rodríguez, “Acquired heart disease in adults: what can a chest X-ray tell us?,” *Radiologia*, vol. 59, no. 5, p. 446, 2017.
- [49] V. Rangan, “Taking a Load Off Diagnosing Constipation: Utility of the Plain Film.” Springer, 2019.

- [50] S. W. Wilkins, T. E. Gureyev, D. Gao, A. Pogany, and A. W. Stevenson, "Phase-contrast imaging using polychromatic hard X-rays," *Nature*, vol. 384, no. 6607, pp. 335–338, 1996.
- [51] C. David, B. Nöhammer, H. H. Solak, and E. Ziegler, "Differential x-ray phase contrast imaging using a shearing interferometer," *Appl. Phys. Lett.*, vol. 81, no. 17, pp. 3287–3289, 2002.
- [52] J. Deng, S. Xu, W. Hu, X. Xun, L. Zheng, and M. Su, "Tumor targeted, stealthy and degradable bismuth nanoparticles for enhanced X-ray radiation therapy of breast cancer," *Biomaterials*, vol. 154, pp. 24–33, 2018.
- [53] B. S. Yadav, P. Chanana, and S. Jhamb, "Biomarkers in triple negative breast cancer: a review," *World J. Clin. Oncol.*, vol. 6, no. 6, p. 252, 2015.
- [54] M. Hofer, "CT teaching manual. A systematic approach to CT reading. 4," 2010.
- [55] S. Sugiyama *et al.*, "CT lymphography for sentinel lymph node mapping of clinically N0 early oral cancer," *Cancer Imaging*, vol. 19, no. 1, pp. 1–6, 2019.
- [56] M. A. Heuvelmans *et al.*, "Disagreement of diameter and volume measurements for pulmonary nodule size estimation in CT lung cancer screening," *Thorax*, vol. 73, no. 8, pp. 779–781, 2018.
- [57] K. Rangan, A. Israrahmed, and S. Gambhir, "Utility of 18F-labeled fluoro-2-deoxyglucose positron emission tomography/computed tomography in

- diagnostic workup and response evaluation in neurotuberculosis,” *J. Nucl. Med.*, vol. 61, no. supplement 1, p. 1561, 2020.
- [58] M. Finessi, G. Bisi, and D. Deandreis, “Hyperglycemia and 18F-FDG PET/CT, issues and problem solving: a literature review,” *Acta Diabetol.*, vol. 57, no. 3, pp. 253–262, 2020.
- [59] G. K. Anagnostopoulos *et al.*, “High-resolution magnification endoscopy can reliably identify normal gastric mucosa, *Helicobacter pylori*-associated gastritis, and gastric atrophy,” *Endoscopy*, vol. 39, no. 03, pp. 202–207, 2007.
- [60] T. T. Higuchi, J. A. Fox, and D. A. Husmann, “Annual endoscopy and urine cytology for the surveillance of bladder tumors after enterocystoplasty for congenital bladder anomalies,” *J. Urol.*, vol. 186, no. 5, pp. 1791–1795, 2011.
- [61] W. De Wever, J. Bogaert, and J. A. Verschakelen, “Virtual bronchoscopy: accuracy and usefulness—an overview,” in *Seminars in Ultrasound, CT and MRI*, 2005, vol. 26, no. 5, pp. 364–373.
- [62] R. L. Siegel *et al.*, “Colorectal cancer statistics, 2020,” *CA. Cancer J. Clin.*, 2020.
- [63] K. Yao *et al.*, “Clinical application of magnification endoscopy and narrow-band imaging in the upper gastrointestinal tract: new imaging techniques for detecting and characterizing gastrointestinal neoplasia,” *Gastrointest. Endosc. Clin. N. Am.*, vol. 18, no. 3, pp. 415–433, 2008.

- [64] Y.-Y. Zhao *et al.*, “Computer-assisted diagnosis of early esophageal squamous cell carcinoma using narrow-band imaging magnifying endoscopy,” *Endoscopy*, vol. 51, no. 04, pp. 333–341, 2019.
- [65] C. Lin *et al.*, “Comparison of ALK detection by FISH, IHC and NGS to predict benefit from crizotinib in advanced non-small-cell lung cancer,” *Lung Cancer*, vol. 131, pp. 62–68, 2019.
- [66] R. J. Huang *et al.*, “Prevalence, risk factors, and surveillance patterns for gastric intestinal metaplasia among patients undergoing upper endoscopy with biopsy,” *Gastrointest. Endosc.*, vol. 91, no. 1, pp. 70–77, 2020.
- [67] A. Irizawa, S. Suga, T. Nagashima, A. Higashiya, M. Hashida, and S. Sakabe, “Laser-induced fine structures on silicon exposed to THz-FEL,” *Appl. Phys. Lett.*, vol. 111, no. 25, p. 251602, 2017.
- [68] G. A. Komandin *et al.*, “BWO generators for terahertz dielectric measurements,” *IEEE Trans. Terahertz Sci. Technol.*, vol. 3, no. 4, pp. 440–444, 2013.
- [69] C. W. I. Chan, Q. Hu, and J. L. Reno, “Ground state terahertz quantum cascade lasers,” *Appl. Phys. Lett.*, vol. 101, no. 15, p. 151108, 2012.
- [70] J. A. Fülöp *et al.*, “Generation of sub-mJ terahertz pulses by optical rectification,” *Opt. Lett.*, vol. 37, no. 4, pp. 557–559, 2012.
- [71] N. Khiabani, Y. Huang, Y.-C. Shen, and S. Boyes, “Theoretical modeling of a photoconductive antenna in a terahertz pulsed system,” *IEEE Trans. Antennas Propag.*, vol. 61, no. 4, pp. 1538–1546, 2013.

- [72] M. A. Belkin and F. Capasso, “New frontiers in quantum cascade lasers: high performance room temperature terahertz sources,” *Phys. Scr.*, vol. 90, no. 11, p. 118002, 2015.
- [73] N. M. Burford and M. O. El-Shenawee, “Review of terahertz photoconductive antenna technology,” *Opt. Eng.*, vol. 56, no. 1, p. 10901, 2017.
- [74] E. Yiwen, Q. Jin, A. Tcytkin, and X. C. Zhang, “Terahertz wave generation from liquid water films via laser-induced breakdown,” *Appl. Phys. Lett.*, vol. 113, p. 181103, 2018.
- [75] D. S. Ponomarev *et al.*, “Lateral terahertz hot-electron bolometer based on an array of Sn nanothreads in GaAs,” *J. Phys. D. Appl. Phys.*, vol. 51, no. 13, p. 135101, 2018.
- [76] X. Chen, E. P. J. Parrott, B. S.-Y. Ung, and E. Pickwell-MacPherson, “A robust baseline and reference modification and acquisition algorithm for accurate THz imaging,” *IEEE Trans. Terahertz Sci. Technol.*, vol. 7, no. 5, pp. 493–501, 2017.
- [77] N. Fuse *et al.*, “Prognostic impact of HER2, EGFR, and c-MET status on overall survival of advanced gastric cancer patients,” *Gastric cancer*, vol. 19, no. 1, pp. 183–191, 2016.
- [78] C. K. Lee *et al.*, “Checkpoint inhibitors in metastatic EGFR-mutated non-small cell lung cancer—a meta-analysis,” *J. Thorac. Oncol.*, vol. 12, no. 2, pp. 403–407, 2017.

- [79] P. Bossi, C. Resteghini, N. Paielli, L. Licitra, S. Pilotti, and F. Perrone, “Prognostic and predictive value of EGFR in head and neck squamous cell carcinoma,” *Oncotarget*, vol. 7, no. 45, p. 74362, 2016.
- [80] S. Maheswaran *et al.*, “Detection of mutations in EGFR in circulating lung-cancer cells,” *N. Engl. J. Med.*, vol. 359, no. 4, pp. 366–377, 2008.
- [81] G. R. Oxnard *et al.*, “Noninvasive detection of response and resistance in EGFR-mutant lung cancer using quantitative next-generation genotyping of cell-free plasma DNA,” *Clin. cancer Res.*, vol. 20, no. 6, pp. 1698–1705, 2014.
- [82] P. G. Calavia, G. Bruce, L. Pérez-García, and D. A. Russell, “Photosensitiser-gold nanoparticle conjugates for photodynamic therapy of cancer,” *Photochem. Photobiol. Sci.*, vol. 17, no. 11, pp. 1534–1552, 2018.
- [83] R. Maity *et al.*, “Gold nanoparticle-assisted enhancement in the anti-cancer properties of theaflavin against human ovarian cancer cells,” *Mater. Sci. Eng. C*, vol. 104, p. 109909, 2019.
- [84] L. C. Kennedy *et al.*, “A new era for cancer treatment: gold - nanoparticle - mediated thermal therapies,” *Small*, vol. 7, no. 2, pp. 169–183, 2011.
- [85] W. Xu, L. Xie, and Y. Ying, “Mechanisms and applications of terahertz metamaterial sensing: a review,” *Nanoscale*, vol. 9, no. 37, pp. 13864–13878, 2017.
- [86] Q. Sun, Y. He, K. Liu, S. Fan, E. P. J. Parrott, and E. Pickwell-MacPherson, “Recent advances in terahertz technology for biomedical applications,” *Quant. Imaging Med. Surg.*, vol. 7, no. 3, p. 345, 2017.

-
- [87] X. Yang *et al.*, “Biomedical applications of terahertz spectroscopy and imaging,” *Trends Biotechnol.*, vol. 34, no. 10, pp. 810–824, 2016.
- [88] J. Jeong *et al.*, “High Contrast Detection of Water - Filled Terahertz Nanotrenches,” *Adv. Opt. Mater.*, vol. 6, no. 21, p. 1800582, 2018.
- [89] D.-K. Lee *et al.*, “Highly sensitive and selective sugar detection by terahertz nano-antennas,” *Sci. Rep.*, vol. 5, no. 1, pp. 1–7, 2015.
- [90] L. Xie, W. Gao, J. Shu, Y. Ying, and J. Kono, “Extraordinary sensitivity enhancement by metasurfaces in terahertz detection of antibiotics,” *Sci. Rep.*, vol. 5, no. 1, pp. 1–4, 2015.
- [91] L. Cong, S. Tan, R. Yahiaoui, F. Yan, W. Zhang, and R. Singh, “Experimental demonstration of ultrasensitive sensing with terahertz metamaterial absorbers: A comparison with the metasurfaces,” *Appl. Phys. Lett.*, vol. 106, no. 3, p. 31107, 2015.
- [92] R. Singh, W. Cao, I. Al-Naib, L. Cong, W. Withayachumnankul, and W. Zhang, “Ultrasensitive terahertz sensing with high-Q Fano resonances in metasurfaces,” *Appl. Phys. Lett.*, vol. 105, no. 17, p. 171101, 2014.
- [93] H. Tao *et al.*, “Metamaterials on paper as a sensing platform,” *Adv. Mater.*, vol. 23, no. 28, pp. 3197–3201, 2011.
- [94] H. Tao *et al.*, “Performance enhancement of terahertz metamaterials on ultrathin substrates for sensing applications,” *Appl. Phys. Lett.*, vol. 97, no. 26, p. 261909, 2010.

- [95] S. J. Park, B. H. Son, S. J. Choi, H. S. Kim, and Y. H. Ahn, "Sensitive detection of yeast using terahertz slot antennas," *Opt. Express*, vol. 22, no. 25, pp. 30467–30472, 2014.
- [96] J. Qin, L. Xie, and Y. Ying, "A high-sensitivity terahertz spectroscopy technology for tetracycline hydrochloride detection using metamaterials," *Food Chem.*, vol. 211, pp. 300–305, 2016.
- [97] W. Xu *et al.*, "Terahertz sensing of chlorpyrifos-methyl using metamaterials," *Food Chem.*, vol. 218, pp. 330–334, 2017.
- [98] A. Salim and S. Lim, "Review of recent metamaterial microfluidic sensors," *Sensors*, vol. 18, no. 1, p. 232, 2018.
- [99] K. Shih, P. Pitchappa, L. Jin, C.-H. Chen, R. Singh, and C. Lee, "Nanofluidic terahertz metasensor for sensing in aqueous environment," *Appl. Phys. Lett.*, vol. 113, no. 7, p. 71105, 2018.
- [100] X. Wu, X. Pan, B. Quan, X. Xu, C. Gu, and L. Wang, "Self-referenced sensing based on terahertz metamaterial for aqueous solutions," *Appl. Phys. Lett.*, vol. 102, no. 15, p. 151109, 2013.
- [101] B. Ng *et al.*, "Lattice resonances in antenna arrays for liquid sensing in the terahertz regime," *Opt. Express*, vol. 19, no. 15, pp. 14653–14661, 2011.
- [102] Z. Geng, X. Zhang, Z. Fan, X. Lv, and H. Chen, "A route to terahertz metamaterial biosensor integrated with microfluidics for liver cancer biomarker testing in early stage," *Sci. Rep.*, vol. 7, no. 1, pp. 1–11, 2017.

- [103] K. Shih, P. Pitchappa, M. Manjappa, C. P. Ho, R. Singh, and C. Lee, “Microfluidic metamaterial sensor: Selective trapping and remote sensing of microparticles,” *J. Appl. Phys.*, vol. 121, no. 2, p. 23102, 2017.
- [104] M. Chen, L. Singh, N. Xu, R. Singh, W. Zhang, and L. Xie, “Terahertz sensing of highly absorptive water-methanol mixtures with multiple resonances in metamaterials,” *Opt. Express*, vol. 25, no. 13, pp. 14089–14097, 2017.
- [105] X. Hu *et al.*, “Metamaterial absorber integrated microfluidic terahertz sensors,” *Laser Photon. Rev.*, vol. 10, no. 6, pp. 962–969, 2016.
- [106] M. Tonouchi, “Terahertz microfluidic chip sensitivity-enhanced with a few arrays of meta atoms,” in *Optical Sensors*, 2018, pp. SeTh4E-1.
- [107] K. Serita, J. Darmo, I. Kawayama, H. Murakami, and M. Tonouchi, “Direct measurements of terahertz meta-atoms with near-field emission of terahertz waves,” *J. Infrared, Millimeter, Terahertz Waves*, vol. 38, no. 9, pp. 1107–1119, 2017.
- [108] R. Zhang *et al.*, “Terahertz microfluidic metamaterial biosensor for tiny volume liquid samples,” in *2018 43rd International Conference on Infrared, Millimeter, and Terahertz Waves (IRMMW-THz)*, 2018, pp. 1–2.
- [109] M. V Cojocari, K. I. Schegoleva, and A. A. Basharin, “Blueshift and phase tunability in planar THz metamaterials: the role of losses and toroidal dipole contribution,” *Opt. Lett.*, vol. 42, no. 9, pp. 1700–1703, 2017.

- [110] L. Qi and C. Li, "Multi-band terahertz filter with independence to polarization and insensitivity to incidence angles," *J. Infrared, Millimeter, Terahertz Waves*, vol. 36, no. 11, pp. 1137–1144, 2015.
- [111] I. Al-Naib, "Biomedical sensing with conductively coupled terahertz metamaterial resonators," *IEEE J. Sel. Top. Quantum Electron.*, vol. 23, no. 4, pp. 1–5, 2016.
- [112] H. Cheon, J. H. Paik, M. Choi, H.-J. Yang, and J.-H. Son, "Detection and manipulation of methylation in blood cancer DNA using terahertz radiation," *Sci. Rep.*, vol. 9, no. 1, pp. 1–10, 2019.
- [113] R. H. Giles, F. Doradla, J. Martin, and C. S. Joseph, "Applications of terahertz frequency technologies in biology," in *2017 42nd International Conference on Infrared, Millimeter, and Terahertz Waves (IRMMW-THz)*, 2017, pp. 1–2.
- [114] G. Gallot, "Terahertz sensing in biology and medicine," *Photoniques*, no. 101, pp. 53–58, 2020.
- [115] M. Gupta, Y. K. Srivastava, M. Manjappa, and R. Singh, "Sensing with toroidal metamaterial," *Appl. Phys. Lett.*, vol. 110, no. 12, p. 121108, 2017.
- [116] M. R. Grootendorst *et al.*, "Use of a handheld terahertz pulsed imaging device to differentiate benign and malignant breast tissue," *Biomed. Opt. Express*, vol. 8, no. 6, pp. 2932–2945, 2017.
- [117] T. Chavez, T. Bowman, J. Wu, K. Bailey, and M. El-Shenawee, "Assessment of terahertz imaging for excised breast cancer tumors with image

- morphing,” *J. Infrared, Millimeter, Terahertz Waves*, vol. 39, no. 12, pp. 1283–1302, 2018.
- [118] M. El-Shenawee, N. Vohra, T. Bowman, and K. Bailey, “Cancer detection in excised breast tumors using terahertz imaging and spectroscopy,” *Biomed. Spectrosc. Imaging*, vol. 8, no. 1–2, pp. 1–9, 2019.
- [119] G. M. Png, J. W. Choi, B. W. H. Ng, S. P. Mickan, D. Abbott, and X. C. Zhang, “The impact of hydration changes in fresh bio-tissue on THz spectroscopic measurements,” *Phys. Med. Biol.*, vol. 53, no. 13, p. 3501, 2008.
- [120] Y. He, B. S.-Y. Ung, E. P. J. Parrott, A. T. Ahuja, and E. Pickwell-MacPherson, “Freeze-thaw hysteresis effects in terahertz imaging of biomedical tissues,” *Biomed. Opt. Express*, vol. 7, no. 11, pp. 4711–4717, 2016.
- [121] G. G. Hernandez-Cardoso *et al.*, “Terahertz imaging for early screening of diabetic foot syndrome: A proof of concept,” *Sci. Rep.*, vol. 7, p. 42124, 2017.
- [122] K. Dhanuthai *et al.*, “Oral cancer: A multicenter study,” *Med. Oral Patol. Oral Cir. Bucal*, vol. 23, no. 1, p. e23, 2018.
- [123] S. Yamada *et al.*, “Evaluation of the level of progression of extracapsular spread for cervical lymph node metastasis in oral squamous cell carcinoma,” *Int. J. Oral Maxillofac. Surg.*, vol. 45, no. 2, pp. 141–146, 2016.